receptor blocker, protected the heart against ischemia-reperfusion injury in dogs [1] and also improved both symptoms of CHF and ventricular remodeling in the clinical setting [16]. Although the maximum inotropic effects of substances acting through cAMP were decreased in diseased myocardium [6], famotidine, a histamine H_2 receptor blocker, exerts negative effects on cardiac performance [13], the roles of the histamine would have remained unclear in the state of heart failure.

In addition, it is still unclear whether histamine H_2 receptor blockers have a protective effect against CHF by reducing the myocardial accumulation of cAMP and whether there is an additive effect of histamine H_2 receptor blockade in the presence of β-adrenergic receptor blockade.

Therefore, we investigated the effect of a histamine H_2 receptor blocker on cardiac performance and myocardial cAMP accumulation in dogs with pacing-induced heart failure, and also investigated whether there was an additive effect of combined histamine H_2 receptor blocker and β-blocker therapy on cardiac performance.

Methods

Materials

The histamine H_2 receptor blocker famotidine was kindly provided by Astellas Pharma Inc. (Tokyo, Japan). Carvedilol, a β-adrenergic receptor blocker, was obtained from Sigma (St. Louis, MO, USA). Rabbit polyclonal anti-histamine antibody was obtained from Progen (Queensland, Australia).

Animal preparation

Beagle dogs (Oriental Yeast Co. Ltd., Tokyo, Japan) weighing 8–10 kg were sedated with intravenous sodium pentobarbital at a dose of 25 mg/kg. After intubation with a cuffed endotracheal tube, anesthesia was maintained with 0.5–1% isoflurane and an equal mixture of air and oxygen. Ventilation was provided with a tidal volume of 22 mL/kg at a rate of 15 times per minute. A bipolar pacing lead (Model BT-45P, Star Medical Inc., Tokyo, Japan) was advanced under fluoroscopic guidance through the right jugular vein to the right ventricular (RV) apex and was connected to an external programmable pacemaker (VOO mode; Model SIP-501, Star Medical Inc., Tokyo, Japan) that was implanted in a subcutaneous pocket in the neck. The success of this procedure was confirmed by electrocardiography. Antibiotics were given after surgery, and the dogs were allowed to recover fully. Then heart failure was induced by rapid right ventricular pacing at a rate of 230 beats/min for 4 weeks as the model mimicking heart failure in human, as reported previously [22, 23, 27].

All procedures were performed in conformity with the Guide for the Care and Use of Laboratory Animals (NIH publication No. 85–23, 1996 revision) and were approved by the ethical committee for laboratory animal use of the National Cardiovascular Center in Japan.

Echocardiography

Transthoracic echocardiography was performed by using an echocardiographic system equipped with a 2–4 MHz phased-array transducer (SONOS 5500, Hewlett Packard, Massachusetts, USA) in conscious dogs before pacemaker implantation and 30 min after the cessation of RV pacing at 4 weeks. Good two-dimensional short-axis views of the left ventricle were obtained at the level of the papillary muscles for guided M-mode measurement of the left ventricular (LV) end-diastolic dimension (LVDd), LV end-systolic dimension (LVDs), LV fractional shortening (LVFS), and LV ejection fraction (LVEF). All measurements were made by two observers, who were blinded to the source of the tracings.

Hemodynamic studies

LV pressure and mean aortic pressure were measured by pressure amplifiers connected to a pig tail catheter (5F, Terumo Co. Ltd., Tokyo, Japan) that was inserted into the left ventricle from the left femoral artery. Pulmonary capillary wedge pressure (PCWP) was measured with a 7 Fr Swan-Ganz catheter (American Edwards Laboratories, California, USA). LV dP/dt was analyzed using software (Data viewer, Yokogawa Electric Corporation, Tokyo, Japan). These studies were performed both before and after 4 weeks of RV pacing or 4 weeks after pacemaker implantation in the sham group.

Measurement of the myocardial cAMP level

The myocardial cyclic AMP (cAMP) level was measured as described previously [8]. Briefly, a sample of frozen cardiac muscle was homogenized mechanically in 500 mL of frozen hydrochloric acid (0.1 N) with a mechanical homogenizer. The homogenate was thawed and centrifuged at $5{,}000\times g$ at room temperature for 15 min and then a 100 mL aliquot of the supernatant was employed to measure cAMP with a sensitive radioimmunoassay (cyclic AMP kit; Yamasa Shoyu Co., Choshi, Japan).

Immunohistochemical analysis

Immunohistochemical analysis was performed as described previously [24]. Briefly, myocardial tissue samples were fixed in 10% formalin and embedded in paraffin. Then

5-μm-thick sections were cut and preincubated with 3% hydrogen peroxide. Rabbit polyclonal anti-histamine antibody (1:1,000 dilution) was added, and incubation was done at room temperature overnight. Next, the sections were incubated with biotinylated anti-rabbit immunoglobulin for 30 min and subsequently with horseradish peroxidase-labeled streptavidin solution for 30 min. The slides were rinsed in tris-buffered saline after each incubation step. Peroxidase activity was visualized by incubation with diaminobenzidine hydrochloride solution.

Experimental protocols

Protocol 1: effects of famotidine on cardiac performance and myocardial cAMP accumulation in dogs with pacing-induced heart failure

After pacemaker implantation, the dogs were randomly assigned to a sham group ($n = 6$) without pacing, a control group ($n = 7$) with pacing only, and a famotidine group ($n = 5$) with pacing plus the daily oral administration of famotidine (1 mg/kg per day). The dose of famotidine was chosen on the basis of previous reports [30, 36]. Echocardiography and measurement of hemodynamic parameters were performed before and 4 weeks after pacemaker implantation. After the measurement of hemodynamic parameters, myocardial tissue samples were obtained and quickly placed into liquid nitrogen for storage at −80°C until measurement of cAMP levels.

Protocol 2: effects of famotidine on cardiac performance in dogs with pacing-induced heart failure under β-adrenergic receptor blockade

Next, we examined the additive effect of histamine H_2 receptor blockade on the development of CHF. After pacemaker implantation, the dogs were randomly assigned to a carvedilol group ($n = 6$) that received daily oral administration of carvedilol (0.1 mg/kg per day) or a carvedilol + famotidine group ($n = 6$) that received daily oral administration of both carvedilol (0.1 mg/kg per day) and famotidine (1 mg/kg per day).

Statistical analysis

Results are expressed as the mean ± SEM. Comparison of time-course changes between the groups was performed by two-way repeated measures analysis of variance (ANOVA). For comparison of mast cell counts and cAMP levels between the groups, the Mann–Whitney U test was performed. A p value < 0.05 was considered to represent statistical significance.

Results

Mast cells and histamine expression

Mast cells were detected in the myocardium by toluidine blue staining. Consistent with previous reports [8, 26], we observed an increase of mast cells in the failing hearts compared with the number of cells in the sham group (Fig. 1a). Immunohistochemical analysis showed an increase of histamine expression indicating increased degranulation of mast cells in failing hearts compared with the level in the sham group (Fig. 1b).

Effect of famotidine on cardiac performance and myocardial cAMP in dogs with pacing-induced heart failure

Both mean aortic pressure and heart rate before pacing were similar in the control group (104 ± 5 mmHg and

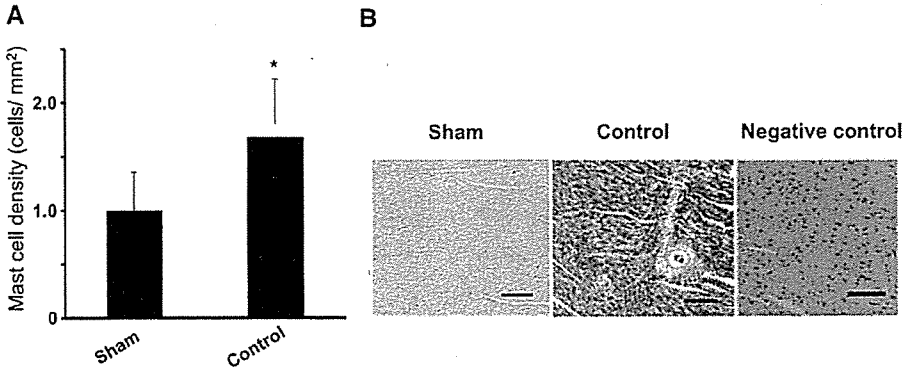

Fig. 1 Mast cell density and histamine expression in the failing heart. **a** Mast cell density in the heart. Values are the mean ± SEM. *$p < 0.05$ versus the sham group. **b** Immunostaining with an anti-histamine antibody. **a** Representative staining of a heart from the sham group. **b** Representative staining of a heart from the control group. **c** Negative control section incubated without the primary antibody. The *scale bars* indicate 50 μm

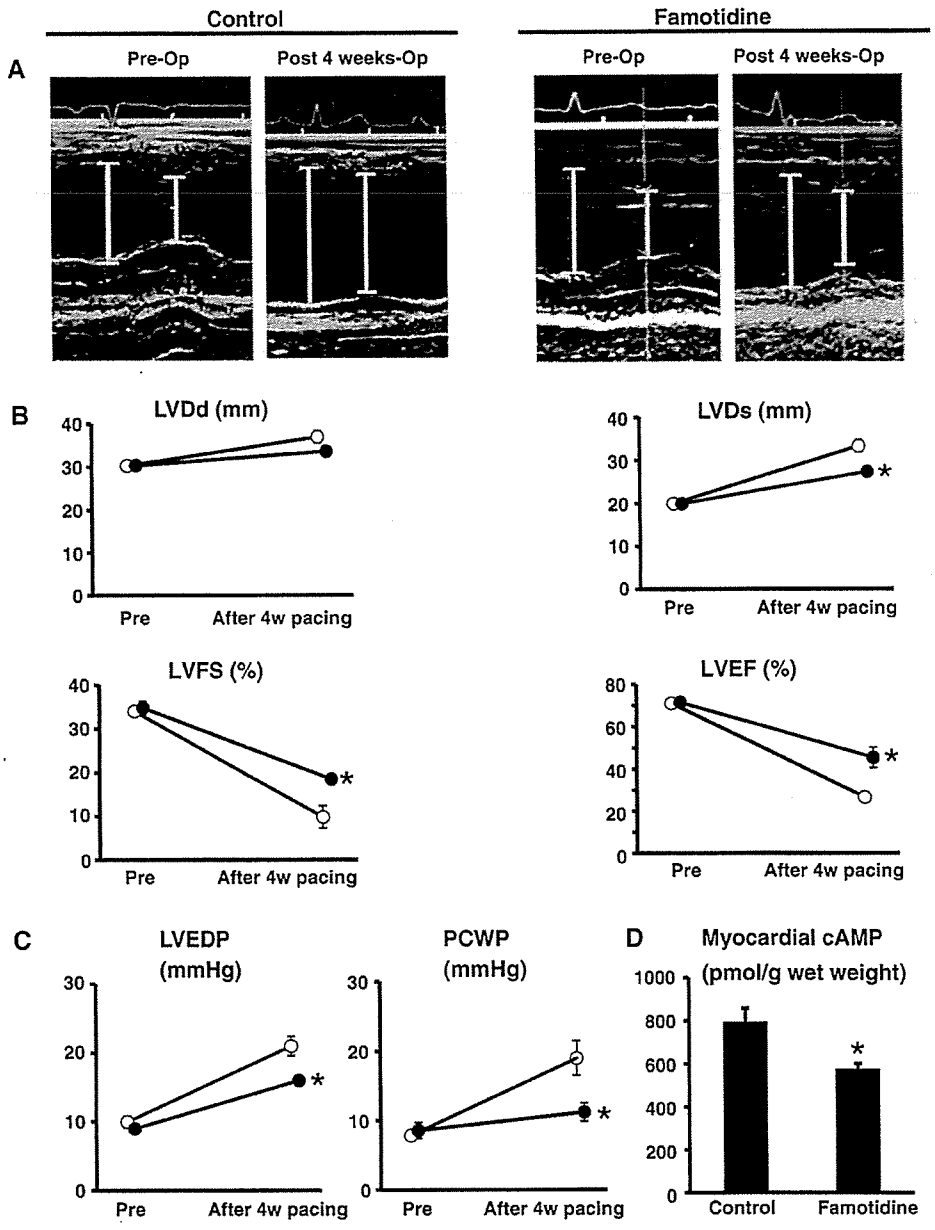

Fig. 2 Effects of famotidine on echocardiographic and hemodynamic parameters and myocardial cAMP levels. **a** Representative 2D echocardiograms. **b** Quantitative analysis of echocardiographic parameters in the control and famotidine groups. *Open* and *closed circles* indicate the control group and the famotidine group, respectively. **c** LVEDP and mean PCWP in the control and famotidine groups. **d** Myocardial cAMP levels in each group. All values are the mean ± SEM. $*p < 0.05$ versus the sham group

117 ± 7 bpm, respectively), and the famotidine group (101 ± 3 mmHg and 115 ± 8 bpm, respectively). These parameters did not significantly differ among the groups. LV d*P*/d*t* was 3,592 ± 512 mmHg/s in the control group and 3,981 ± 528 mmHg/s in the famotidine group. Four weeks after surgery, neither hemodynamic nor echocardiographic data showed any changes compared with the preoperative values in the sham group (data not shown). Four weeks after rapid RV pacing, an administration of famotidine significantly limited the increase of both LVDd and LVDs, as well as the decrease of both LVFS and LVEF (33.4 ± 0.8 mm, 27.4 ± 1.2 mm, 18.5 ± 2.6% and 45.4 ± 4.8%, respectively), compared with the findings in the control group (37.0 ± 1.4 mm, 33.4 ± 1.4 mm, 9.9 ± 1.0% and 26.7 ± 2.4%, respectively) (Fig. 2a, b). Four weeks after RV pacing, LV end-diastolic pressure (LVEDP) and PCWP of the famotidine group (16 ± 2 and 11 ± 1 mmHg, respectively), were both significantly lower compared with the values in the control group (21 ± 2 and 19 ± 2 mmHg and, respectively) (Fig. 2c). LV d*P*/d*t* after RV pacing was significantly preserved higher in the famotidine group (2,601 ± 216 mmHg/s) compared with that in control group (2,077 ± 124 mmHg/s) ($p < 0.05$).

The myocardial cAMP level was significantly higher in the control group (796 ± 111 pmol/g wet weight) compared with that in the sham group (597 ± 77 pmol/g wet

weight), while it was significantly lower in the famotidine group (577 ± 28 pmol/g wet weight) compared with the control group ($p < 0.05$) (Fig. 2d).

Additive effects of famotidine and a β-blocker on cardiac performance in dogs with pacing-induced heart failure

Before pacing, mean aortic pressure and heart rate were both similar in the carvedilol group (101 ± 7 mmHg and 111 ± 8 bpm, respectively), and the famotidine + carvedilol group (93 ± 2 mmHg, 106 ± 7 bpm, respectively), and these parameters did not significantly differ among the groups. LV d*P*/d*t* was 3,672 ± 417 mmHg/s in the carvedilol group and 3,941 ± 284 mmHg/s in the famotidine + carvedilol group. After rapid RV pacing for 4 weeks, both LVDd and LVDs were decreased and both LVFS and LVEF were increased (33 ± 0.4 mm, 25 ± 0.7 mm, 28 ± 2%, and 54 ± 3%, respectively), in the famotidine + carvedilol group compared with the respective values in the carvedilol group (34 ± 1 mm, 28 ± 1 mm, 23 ± 1%, and 38 ± 5%, respectively) (Fig. 3a).

Four weeks after RV pacing, LVEDP and PCWP of the carvedilol + famotidine group (12 ± 3 and 10 ± 4 mmHg, respectively), were both significantly reduced compared with the respective values in the carvedilol group (16 ± 2 and 15 ± 1 mmHg, respectively) (Fig. 3b). LV d*P*/d*t* after RV pacing was preserved higher in the famotidine + carvedilol group (3,382 ± 252 mmHg/s) compared with that in carvedilol group (2,740 ± 321 mmHg/s) ($p < 0.05$).

Furthermore, the myocardial cAMP level was significantly lower in the carvedilol + famotidine group (488 ± 45 pmol/g wet weight) compared with that in the carvedilol group (615 ± 28 pmol/g wet weight) (Fig. 3c).

Discussion

In the present study, we demonstrated that (1) myocardial histamine expression was increased by pacing-induced heart failure, (2) the histamine H_2 receptor blocker famotidine improved cardiac performance (gauged by echocardiographic and hemodynamic parameters) along with a reduction of myocardial cAMP accumulation, and (3) there was an additive effect of combined histamine H_2 receptor and β-adrenergic receptor blockade on cardiac performance in dogs with pacing-induced heart failure.

Impact of histamine blockade on cardiac failure

Histamine is one of the autacoids, and is stored and released by mast cells in the human heart, as well as in other organs or

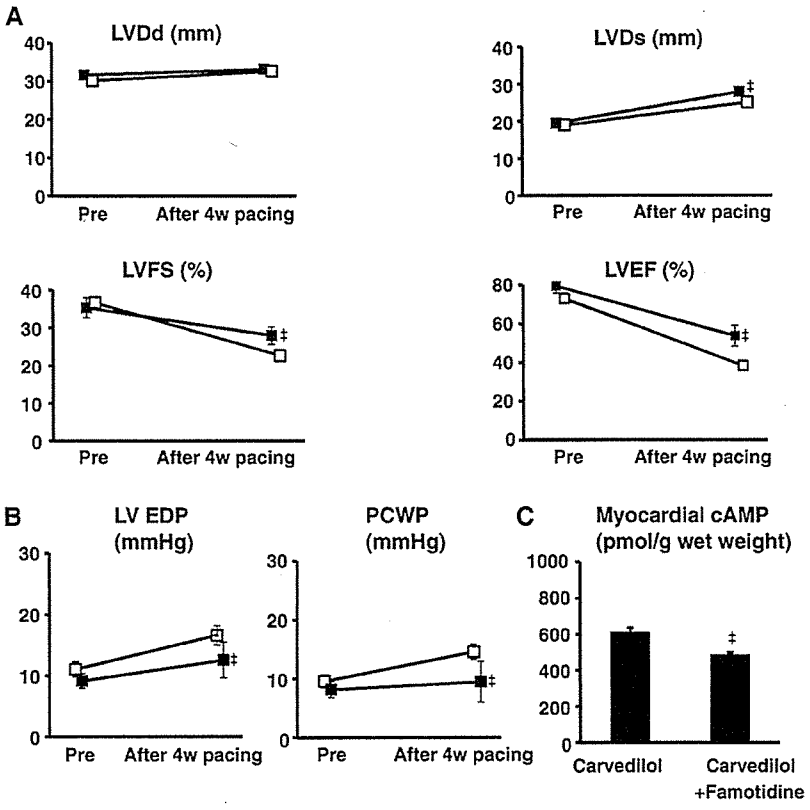

Fig. 3 Additive effect of famotidine and carvedilol on cardiac performance. **a** Quantitative analysis of echocardiographic parameters in the carvedilol and carvedilol + famotidine groups. *Open* and *closed squares* indicate the carvedilol group and the carvedilol + famotidine group, respectively. **b** LVEDP and mean PCWP in the carvedilol group and carvedilol + famotidine group. *Open* and *closed squares* indicate the carvedilol group and the carvedilol + famotidine group, respectively. **c** Myocardial cAMP levels in each group. All values are the mean ± SEM. $*p < 0.05$ versus the carvedilol group

tissues [8]. Recently, the number of mast cells and the myocardial histamine level were found to increase in the hearts of patients with idiopathic dilated cardiomyopathy or ischemic cardiomyopathy [26]. Histamine modulates various cellular functions via the activation of four different G-protein-coupled receptors (H_{1-4} receptors) [29]. As is well known, histamine H_2 receptors located on gastric cells promote the production of gastric acid [10] and histamine H_2 receptor blockers have been widely used for the treatment of peptic ulcer. Interestingly, histamine H_2 receptors are also expressed in canine and human ventricular myocardium [14, 18], although the expression levels were different among species [18]. Consisted with the previous studies, we confirmed the presence of histamine H_2 receptor in the canine heart using quantitative reverse-transcriptase PCR (data not shown).

In the present study, the precise locations of histamine receptors in myocytes or vessels in the canine hearts remained unclear. However, since famotidine did not decrease blood pressure in this study, the accumulating lines of evidence would suggest that histamine H_2 blockers did not have the potent effect on the vessels compared with cardiomyocytes. On the other hand, since histamine H_1 receptors are abundantly expressed in the vessels in most animal species [29], histamine H_1 receptor blocker has the effects on vessels. In addition, stimulation of H_2 receptors transduces the intracellular signals via Gs protein, as does the stimulation of β-adrenergic receptors. Moreover, histamine has a positive inotropic effect on human ventricular myocardium and has been suggested to have a role in cardiovascular diseases [3, 11]. Although it was reported that the maximum inotropic effects of histamine receptor stimulation were less than those mediated by beta-adrenergic receptors [5, 35], the roles of histamine receptor blockade have remained unclear compared with those of beta-adrenergic receptor.

Based on these backgrounds, we previously proposed that histamine H_2 receptor blockers could provide a novel therapeutic strategy for heart failure, and we have reported that histamine H_2 blocker treatment may have a cardioprotective effect in patients with chronic heart failure [16]. In the present study, we found that myocardial histamine expression was increased in dogs with pacing-induced heart failure compared with that in sham dogs on immunohistochemical analysis. Also, the histamine H_2 receptor blocker, famotide, prevented the development of heart failure induced by rapid RV pacing and lessened the myocardial accumulation of cAMP. These findings suggest that histamine H_2 receptor blockade exerts a cardioprotective effect along with the amelioration of myocardial cAMP accumulation. Recently it was reported that increased cardiac adenylyl cyclase expression is associated with mortality after myocardial infarction in rats [31]. It has been controversial for the role of myocardial cAMP in the heart failure [17]. Although increased cAMP acutely induced the improvement of ventricular function, several trials with either beta-adrenergic agonists or PDE inhibitors have revealed an increase in mortality [17, 20]. In the present study, in the dogs with the drugs that decreases myocardial cAMP levels, the development of heart failure was substantially attenuated, however further investigation will be needed to solve the roles of cAMP in the onset and progression of heart failure.

Additive effects of histamine H_2 blocker and β-blocker therapy on cardiac performance

β-Blockers have long been established as useful agents for chronic heart failure [2, 7, 25, 32]. These drugs act by preventing intracellular Ca overload, because β-adrenergic stimulation promotes Ca overload via Gs protein [34]. Histamine H_2 receptor blockade also prevents Ca overload [28], so we hypothesized that the combination of a histamine H_2 receptor blocker and a β-blocker would exert a stronger cardioprotective effect than either agent alone. Almost all of the patients in our earlier study, which showed that histamine H_2 receptor blockers were effective for the treatment of CHF, were also on β-blocker therapy [16], suggesting that there was an additive effect of histamine H_2 receptor and β-adrenergic receptor blockade in patients with CHF. In the present study, we demonstrated that the combination of a histamine H_2 receptor blocker and a β-blocker prevented the development of heart failure compared with β-blocker monotherapy. Thus, histamine H_2 receptor blockers have a potential clinical role in the treatment of CHF.

Rationale of the present study

The present study provided strong experimental evidence that histamine H_2 receptor blockade improves the pathophysiology of CHF. We have already reported about the beneficial effects of famotidine in patients with heart failure [16]. However, clinical research may be confounded by unexpected errors due to (1) the influence of other drugs being used by patients with CHF, (2) variation in the severity of CHF between patients, and (3) variation in the duration of CHF. Therefore, it was important to prove that histamine H_2 receptor blockade improves CHF in a controlled experimental setting (canine cardiomyopathy model) to support the clinical use of famotidine for CHF. Furthermore, to determine the merit of famotidine in heart failure patients, the present study would be a basis to design a prospective randomized double-blinded study.

Limitations

There are several limitations in this study. First, carvedilol blocks alpha$_1$-, beta$_1$-, beta$_2$- receptors, decreased the cardiac effects of norepinephrine, and has additional antioxidant and antiproliferative effects [4, 19]. In the present study, we did not address that carvedilol has the pleiotropic effects and is not just a beta-blocker.

Second, we did not measure cardiac output as a cardiac contractive index in the present study. However, we have previously reported that our tachycardia-induced heart failure model in dogs using the same procedure of the present study, revealed the low output state that mimics heart failure in human [27]. Our untreated dogs in the heart failure group were strongly suggested in the low output state because of decreased the level of ejection fraction as much as our previous study. In the present study, we analyzed the values of dP/dt as the index of contractility by measuring LV pressure using a pig tail catheter.

In summary, despite these limitations, we demonstrated that the histamine H_2 receptor blockade preserves cardiac systolic function in dogs with pacing-induced heart failure, even in the presence of β-adrenergic receptor blockade. This finding strengthens the rationale for the beneficial effects of histamine H_2 blockers in the treatment of heart failure.

Acknowledgments The authors thank Akiko Ogai for technical assistance; Masahiko Takahashi (Astellas Co. Ltd.) for providing information on famotidine; and the Evidence Finders' Club for their encouragement of this study. This work was supported by a Grant-in-aid from the Japanese Ministry of Health, Labor, and Welfare; a Grant-in-aid from the Japanese Ministry of Education, Culture, Sports, Science and Technology; a Grant from the Japan Heart Foundation; and a Grant from the Japan Cardiovascular Research Foundation.

Conflict of interest None.

References

1. Asanuma H, Minamino T, Ogai A, Kim J, Asakura M, Komamura K, Sanada S, Fujita M, Hirata A, Wakeno M, Tsukamoto O, Shinozaki Y, Myoishi M, Takashima S, Tomoike H, Kitakaze M (2006) Blockade of histamine H_2 receptors protects the heart against ischemia and reperfusion injury in dogs. J Mol Cell Cardiol 40:666–674
2. Bristow MR, Gilbert EM, Abraham WT, Adams KF, Fowler MB, Hershberger RE, Kubo SH, Narahara KA, Ingersoll H, Krueger S, Krueger S, Young S, Shusterman N (1996) Carvedilol produces dose-related improvements in left ventricular function and survival in subjects with chronic heart failure. Circulation 94:2807–2816
3. Bristow MR, Ginsburg R, Harrison DC (1982) Histamine and the human heart: the other receptor system. Am J Cardiol 49:249–251
4. Bristow MR (1997) Mechanism of action of beta-blocking agents in heart failure. Am J Cardiol 80:26L–40L
5. Brodde OE, Hillemann S, Kunde K, Vogelsang M, Zerkoski HR (1992) Receptor systems affecting force of contraction in the human heart and their alterations in chronic heart failure. J Heart Lung Transplant 11:S164–S174
6. Brown L, Lorenz B, Erdmann E (1986) Reduced positive inotropic effects in diseased human ventricular myocardium. Cardiovasc Res 20:516–520
7. CIBIS II Investigators and Committees (1999) The cardiac insufficiency bisoprolol study II (CIBIS II): a randomized trial. Lancet 353:9–13
8. Dvorak AM (1986) Mast-cell degranulation in human hearts. N Engl J Med 315:969–970
9. Eichhorn EJ (1998) Restoring function in failing hearts: the effects of beta blockers. Am J Med 104:163–169
10. Gantz I, Schaffer M, DelValle J, Logsdon C, Campbell V, Uhier M, Yamada T (1991) Molecular cloning of a gene encoding the histamine H_2 receptor. Proc Natl Acad Sci USA 88:5937
11. Hara M, Ono K, Hwang MW, Iwasaki A, Okada M, Nakatani K, Sasayama S, Matsumori A (2002) Evidence for a role of mast cells in the evolution to congestive heart failure. J Exp Med 195:375–381
12. Hattori Y (1999) Cardiac histamine receptors: their pharmacological consequences and signal transduction pathways. Methods Find Exp Clin Pharmacol 21:123–131
13. Hinrichsen H, Halabi A, Kirsch W (1990) Hemodynamic effects of different H_2-receptor antagonists. Clin Pharmacol Ther 48:302–308
14. Hill SJ, Ganellin CR, Timmerman H, Schwartz JC, Shankley NP, Young JM, Schunack W, Levi R, Haas HL (1997) International Union of Pharmacology. XIII. Classification of histamine receptors. Pharmacol Rev 49:253–278
15. Jessup M, Brozena S (2003) Heart failure. N Engl J Med 348:2007–2018
16. Kim J, Ogai A, Nakatani S, Hashimura K, Kanzaki H, Komamura K, Asakura M, Asanuma H, Kitamura S, Tomoike H, Kitakaze M (2006) Impact of blockade of histamine H_2 receptors on chronic heart failure revealed by retrospective and prospective randomized studies. J Am Coll Cardiol 48:1378–1384
17. Leineweber K, Bohm M, Heusch G (2006) Cyclic adenosine monophosphate in acute myocardial infarction with heart failure Slayer or savior? Circulation 114:365–367
18. Matsuda N, Jesmin S, Takahashi Y, Hatta E, Kobayashi M, Matsuyama K, Kawakami N, Sakuma I, Gando S, Fukui H, Hattori Y, Levi R (2004) Histamine H_1 and H_2 receptor gene and protein levels are differentially expressed in the hearts of rodents and humans. J Pharmacol Exp Ther 309:786–795
19. Metra M, Giubbini R, Nodari S, Boldi E, Modena MG, Cas LD (2000) Differential effects of beta-blockers in patients with heart failure. Circulation 102:546–551
20. Movsesian MA (1999) Beta-adrenergic receptor agonists and cyclic nucleotide phosphodiesterase inhibitors: shifting the focus from inotropy to cyclic adenosine monophosphatase. J Am Coll Cardiol 34:318–324
21. Nault MA, Milne B, Parlow JP (2002) Effects of the selective H_1 and H_2 histamine receptor antagonists loratadine and ranitidine on autonomic control of the heart. Anesthesiology 96:336–341
22. Neumann T, Heusch G (1997) Myocardial, skeletal muscle, and renal blood flow during exercise in conscious dogs with heart failure. Am J Physiol 273:H2452–H2457
23. Neumann T, Vollmer A, Schaffner TH, Hess OM, Heusch G (1999) Diastolic dysfunction and collagen structure in canine pacing-induced heart failure. J Mol Cell Cardiol 31:179–192
24. Okada K, Minamino T, Tsukamoto Y, Liao Y, Tsukamoto O, Takashima S, Hirata A, Fujita M, Nagamachi Y, Nakatani T,

Yutani C, Ozawa K, Ogawa S, Tomoike H, Hori M, Kitakaze M (2004) Prolonged endoplasmic reticulum stress in hypertrophic and failing heart after aortic constriction: possible contribution of endoplasmic reticulum stress to cardiac myocyte apoptosis. Circulation 110:705–712

25. Packer M, Coats AJ, Fowler MB, Fowler MB, Katus HA, Krum H, Mohacsi P, Rouleau JL, Tendera M, Castaigne A, Roecker EB, Schultz MK, DeMets DL, Carvedilol Prospective Randomized Cumulative Survival Study group (2001) Effect of carvedilol on survival in severe chronic heart failure. N Engl J Med 344:1651–1658
26. Patella V, Marino I, Arbustini E, Lamparter-Schummert B, Verga L, Adt M, Marone G (1998) Stem cell factor in mast cells and increased mast cell density in idiopathic and ischemic cardiomyopathy. Circulation 97:971–978
27. Sasaki H, Asanuma H, Fujita M, Takahama H, Wakeno M, Ito S, Ogai A, Asakura M, Kim J, Minamino T, Takashima S, Sanada S, Sugimachi M, Komamura K, Mochizuki N, Kitakaze M (2009) Metformin prevents progression of heart failure in dogs: role of AMP-activated protein kinase. Circulation 119:2568–2577
28. Schultz G, Rosenthal W, Hescheler J (1990) Role of G proteins in calcium channel modulation. Annu Rev Physiol 52:275–292
29. Simons FE (2004) Advances in H_1-antihistamines. N Engl J Med 351:2203–2217
30. Sugiyama A, Satoh Y, Takahara A, Nakamura Y, Shimizu-Sasamata M, Sato S, Miyata K, Hashimoto K (2003) Famotidine does not induce long QT syndrome: experimental evidence from in vitro and in vivo test systems. Eur J Pharmacol 466:137–146
31. Takahashi T, Tang T, Lai C, Roth DM, Rebolledo B, Saito M, Lew WYW, Clopton P, Hammond K (2006) Increased cardiac adenylyl cyclase expression is associated with increased survival after myocardial infarction. Circulation 114:388–396
32. The MERIT-HF Study Group (1999) Effect of metoprolol CR/XL in chronic heart failure: Metoprolol CR/XL Randomized Intervention Trial in Congestive Heart Failure (MERIT-HF). Lancet 353:2001–2007
33. Trautwein W, Hescheler J (1990) Regulation of cardiac L-type calcium current by phosphorylation and G proteins. Annu Rev Physiol 52:257–274
34. Xiao RP, Cheng H, Zhou YY, Kuschel M, Lakatta EG (1999) Recent advances in cardiac beta(2)-adrenergic signal transduction. Circ Res 85:1092–1100
35. Zeekowski HR, Broede A, Kunde K, Hillemann S, Schafer E, Vogelsang M, Michel MC, Brodde OE (1993) Comparison of the positive inotropic effects of serotonin, histamine, angiotensin II, endothelin and isoprenaline in the isolated human right atrium. Naunyn-Schemiedeberg's Arch Phamacol 347:347–352
36. Zhou R, Moench P, Heran C, Lu X, Mathias N, Faria TN, Wall DA, Hussain MA, Smith RL, Sun D (2005) pH-dependent dissolution in vitro and absorption in vivo of weakly basic drugs: development of canine model. Pharm Res 22:188–192

Supplemental Material can be found at:
http://www.jbc.org/content/suppl/2010/08/01/M110.155788.DC1.html

THE JOURNAL OF BIOLOGICAL CHEMISTRY VOL. 285, NO. 41, pp. 31337–31347, October 8, 2010

Isoform-specific Intermolecular Disulfide Bond Formation of Heterochromatin Protein 1 (HP1)*[S]

Received for publication, June 19, 2010, and in revised form, July 26, 2010 Published, JBC Papers in Press, August 1, 2010, DOI 10.1074/jbc.M110.155788

Shuichiro Higo[‡], Yoshihiro Asano[‡§¶], Hisakazu Kato[§], Satoru Yamazaki[¶], Atsushi Nakano[‡], Osamu Tsukamoto[¶], Osamu Seguchi[¶], Mitsutoshi Asai[‡], Masanori Asakura[¶], Hiroshi Asanuma[¶], Shoji Sanada[‡], Tetsuo Minamino[‡], Issei Komuro[‡], Masafumi Kitakaze[¶], and Seiji Takashima[‡§1]

From the Departments of [‡]Cardiovascular Medicine and [§]Molecular Cardiology, Osaka University Graduate School of Medicine, Suita, Osaka 565-0871 and the [¶]Department of Cardiovascular Medicine, National Cardiovascular Center, Suita, Osaka 565-8565, Japan

Three mammalian isoforms of heterochromatin protein 1 (HP1), α, β, and γ, play diverse roles in gene regulation. Despite their structural similarity, the diverse functions of these isoforms imply that they are additionally regulated by post-translational modifications. Here, we have identified intermolecular disulfide bond formation of HP1 cysteines in an isoform-specific manner. Cysteine 133 in HP1α and cysteine 177 in HP1γ were involved in intermolecular homodimerization. Although both HP1α and HP1γ contain reactive cysteine residues, only HP1γ readily and reversibly formed disulfide homodimers under oxidative conditions. Oxidatively dimerized HP1γ strongly and transiently interacted with TIF1β, a universal transcriptional co-repressor. Under oxidative conditions, HP1γ dimerized and held TIF1β in a chromatin component and inhibited its repression ability. Our results highlight a novel, isoform-specific role for HP1 as a sensor of the cellular redox state.

Heterochromatin protein 1 (HP1) was originally characterized as an abundant protein that binds pericentric heterochromatin (1). HP1 acts as a scaffold-like molecule, which is composed of two conserved domains as follows: the chromodomain (CD)[2] and the chromoshadow domain (CSD). The variable hinge region separates these two domains (2). The CD recognizes methylated lysine 9 of histone H3 (H3K9), which recruits HP1 to specific sites within the genome (3–5). The CSD promotes HP1 homodimer formation and provides a surface for interaction with a variety of other chromatin proteins (6, 7). Although genetic experiments previously revealed that HP1 works as a repressor of gene activation by propagation of a heterochromatin structure, emerging evidence has elucidated its diverse functions other than gene silencing (8). Some of these functions are regulated in an isoform-specific manner (9).

In vertebrates, three isoforms of HP1 exist as follows: α, β, and γ, all of which share highly conserved domains. Tethering any HP1 isoform upstream of a promoter equally triggers gene silencing concomitant with local chromatin condensation and an increase in H3K9 methylation (10–12), indicating their common silencing ability. However, nonredundant functions (13, 14), different binding affinities to other proteins (15–17) and different localizations in tissues (18, 19), of these three HP1 isoforms imply that α, β, and γ are functionally diverse. Furthermore, recent evidence clarified apparently opposite functions of HP1 isoforms, *e.g.* a role in transcriptional activation or in transcriptional elongation (20, 21). One mechanism that could account for such functional diversity of HP1 isoforms is post-translational modification, which could cause conformational changes in the molecule. In fact, reversible modifications of HP1 (*e.g.* phosphorylation) can modulate its function in response to various stimuli or cellular environments, suggesting an active role for HP1 beyond its known function as a marker of heterochromatin (17, 22). However, the precise modulatory mechanism across three HP1 isoforms that leads to functional differences remains to be elucidated.

Here, we identified isoform-specific disulfide bond formation as a novel post-translational modification of HP1. We analyzed the biochemical and functional characteristics of this oxidative modification. These data may offer a new insight into a novel role for HP1 during the cellular response to oxidative stress.

EXPERIMENTAL PROCEDURES

Materials—We used the following commercially available materials for Western blotting: anti-HP1α (H2164, Sigma; 19s2, Millipore); anti-HP1β (MAB3448, Chemicon); anti-HP1γ (42s2, Millipore); anti-FLAG M2-peroxidase antibody (Sigma); anti-histone H3 (ab1791, Abcam); anti-GAPDH (MAB374, Chemicon); and anti-TIF1β (4123, Cell Signaling). We also used anti-FLAG M2 affinity gel for immunoprecipitation. We used menadione (Sigma), H_2O_2 (Wako), and hydroxytamoxifen (4-OHT) (Sigma) for cell treatment.

Cell Fractionation—Cells were lysed with hypotonic lysis buffer (10 mM HEPES, pH 7.9, 1.5 mM $MgCl_2$, and 10 mM KCl) with 0.5% Nonidet P-40 and centrifuged at 20,000 × *g* for 5 min.

* This work was supported by grants-in-aid from the Ministry of Health, Labor, and Welfare of Japan, grants-in-aid from the Ministry of Education, Culture, Sports, Science, and Technology of Japan, grants from the Japan Heart Foundation, grants from the Japan Cardiovascular Research Foundation, a grant from the Japan Society for the Promotion of Science, Mochida Memorial Foundation for Medical and Pharmaceutical Research, Japan Medical Association, Japan Incurable Diseases Research Foundation, Osaka Medical Research Foundation for Incurable Diseases, Suzuken Memorial Foundation, and Japan China Medical Association.

[S] The on-line version of this article (available at http://www.jbc.org) contains supplemental Figs. S1–S4, "Experimental Procedures," and additional references.

[1] To whom correspondence should be addressed. Tel.: 81-6-6879-3472; Fax: 81-6-6879-3473; E-mail: takasima@medone.med.osaka-u.ac.jp.

[2] The abbreviations used are: CD, chromodomain; CSD, chromoshadow domain; HUVEC, human umbilical vein endothelial cell; 4-OHT, hydroxytamoxifen.

The supernatant was collected as the cytosolic fraction. Extraction buffer (20 mM HEPES, pH 7.9, 1.5 mM $MgCl_2$, 0.42 M NaCl, 0.2 mM EDTA, 25% glycerol) was added to the pellet, and ultrasonic agitation was performed (30-s sonication with 30-s interval, 4–6 times at 0 °C; Bioruptor, CosmoBio). The suspension was incubated for 15 min at 4 °C and centrifuged at 20,000 × *g* for 10 min. The supernatant was collected as the nuclear extract.

Column Chromatography—For anion exchange, whole cells were lysed with buffer A (20 mM Tris, pH 8.0, 5% acetonitrile) containing 5 mM EDTA and 1% Nonidet P-40 and incubated at 4 °C for 15 min. The lysate was centrifuged at 20,000 × *g* for 5 min, and the supernatant was filtered and loaded onto an anion-exchange column (Q-Sepharose High Performance, GE Healthcare) pre-equilibrated with buffer A. After unbound samples were washed, protein was eluted with a linear gradient (0–100%) of buffer B (buffer A with 1.0 M NaCl). For reverse-phase HPLC, purified protein samples and nuclear extracts were prepared with 0.3% trifluoroacetic acid (TFA) and 20% acetonitrile and applied to a phenyl reverse-phase column (4.6 × 250 mm; Nakalai Tesque). Bound proteins were eluted by a segmented linear gradient of increasing concentrations of buffer B (acetonitrile and 0.1% TFA) in buffer A (0.1% TFA) at a flow rate of 0.5 ml/min. Buffer B was increased at a rate of 1.0%/fraction (fast gradient) or 0.2%/fraction (slow gradient). Collected fractions were dried by a centrifugal evaporator and reconstituted with SDS sample buffer with or without 2.5% 2-mercaptoethanol (reducing or nonreducing conditions, respectively).

Triton Extraction—Triton extraction was carried out as described previously with modification (23). Cells were lysed with a hypotonic lysis buffer with 0.5% Nonidet P-40 and centrifuged at 20,000 × *g* for 5 min (as described above). The pellet was lysed in extraction buffer with 0.2% Triton X-100, incubated on ice for 30 min, and centrifuged at 20,000 × *g* for 5 min. The supernatant was kept as a Triton-soluble fraction. The remaining pellet was lysed in SDS sample buffer (250 mM Tris, 5% SDS, and 5% glycerol) with or without 2.5% 2-mercaptoethanol (reducing or nonreducing conditions, respectively), and ultrasonic agitation was performed as described above. After centrifugation at 20,000 × *g* for 5 min, the supernatant was kept as a Triton-insoluble fraction.

RNAi Knockdowns and Generation of HEK293T Stable Cells—Lentiviral particles derived from the pLKO.1-puro-containing shRNA sequence were purchased from the Mission shRNA library (Sigma). The oligonucleotide sequences of the shRNA were as follows: shRNA-6, CGACGTGTAGTGAATGGGAAA; and shRNA-7, GCGTTTCTTAACTCTCAGAAA. Lentiviral particles were used to transduce human umbilical vein endothelial cells (HUVECs) or HEK293T cells in the presence of 8 μg/ml Polybrene. To generate a HEK293T stable cell line, the infected cells were selected with 1 μg/ml puromycin. The stable cells in which HP1γ was almost completely depleted were next transfected with pEF-DEST51 HP1γ-FLAG WT or a C177S mutant (cloned from murine cDNA and resistant to shRNA), and the stable cells were selected with 5 μg/ml blasticidin.

GAL4-luciferase Reporter Assay—pC3-ERHBD-GAL4 or pC3-ERHBD-GAL4-KAP1 (TIF1β) with pGL4.31-PSV40-GAL4UAS were transfected using Lipofectamine 2000 into subconfluent HEK293T stable cells that were passaged 1 day before transfection. After 24 h, 0.04% ethanol or 4-OHT (500 nM) was added to the culture medium. Forty eight h after transfection, luciferase activity was measured by a luminometer (Lumat LB9507). Intranuclear mRNA levels of luciferase were measured as follows. Twenty four h after transfection, 4-OHT (500 nM) was added to the culture medium. Forty eight h after transfection, cells were lysed with a hypotonic lysis buffer with 0.5% Nonidet P-40 and centrifuged at 20,000 × *g* for 5 min (as described above). From the nuclear pellet, total RNA was isolated using RNA-Bee (Cosmo Bio). Total RNA was treated with DNase (Turbo DNA-free, Applied Biosystems) and was reverse-transcribed using a high capacity cDNA reverse transcription kit (Applied Biosystems). Luciferase mRNA levels were measured by real time quantitative PCR (SYBR Green ER, Invitrogen). Firefly luciferase cDNA was amplified using the following primers: 5′-TACCCACTCGAAGACGGGAC-3′ and 5′-ACTCGGCGTAGGTAATGTCCACCTC-3′. Human 18 S ribosomal RNA was measured using the following primers: 5′-GTAACCCGTTGAACCCCATT-3′ and 5′-CCATCCAATCGGTAGTAGCG-3′. The relative levels of luciferase mRNA were normalized to the mRNA levels of 18 S ribosomal RNA.

RESULTS

HP1α Forms Dimers via Disulfide Bonds through Cysteine 133—During purification of HP1α in our previous work (24), we found that endogenous HP1α separates into two peaks by fractionation using reverse-phase HPLC. To confirm this finding, we fractionated whole cell lysates from HEK293T cells using two-step column chromatography (Fig. 1*A*). Endogenous HP1α was eluted at a salt concentration ranging from 0.3 to 0.35 M on a Q-Sepharose anion-exchange column (Fig. 1*D*, *top panel*). We applied this single peak to a reverse-phase column. After elution with a fast gradient, HP1α was still detected as a single peak (Fig. 1*D*, *2nd panel*). However, when eluted with a slow gradient, HP1α separated into two peaks representing a hydrophilic and a hydrophobic form (Fig. 1*D*, *3rd panel*). Two other HP1α antibodies against different epitopes also detected both bands (data not shown), suggesting that these were biochemically different forms of HP1α. Even after direct fractionation of the nuclear extract, which includes the bulk of HP1α protein (Fig. 1*B*), endogenous HP1α showed a similar bimodal distribution (Fig. 1*D*, *4th panel*). In other primary cells (HUVECs, neonatal rat cardiomyocytes, and rat cardiac fibroblasts), similar bimodal peaks were observed (supplemental Fig. S1). In contrast, recombinant HP1α expressed in *Escherichia coli* (Fig. 1*C*) exhibited only one peak with elution characteristics similar to those of the hydrophilic peak under the same separating condition used for the endogenous protein (Fig. 1*D*, *bottom panel*). These data suggest that two different forms of HP1α endogenously exist in multiple cell types and that the late-eluted hydrophobic species may be a post-translationally modified form.

To further elucidate the molecular characteristics of these two forms of HP1α, we used recombinant FLAG-tagged HP1α (HP1α-FLAG). As with endogenous HP1α, HP1α-FLAG existed mainly as a nuclear protein (Fig. 1*E*) and exhibited the

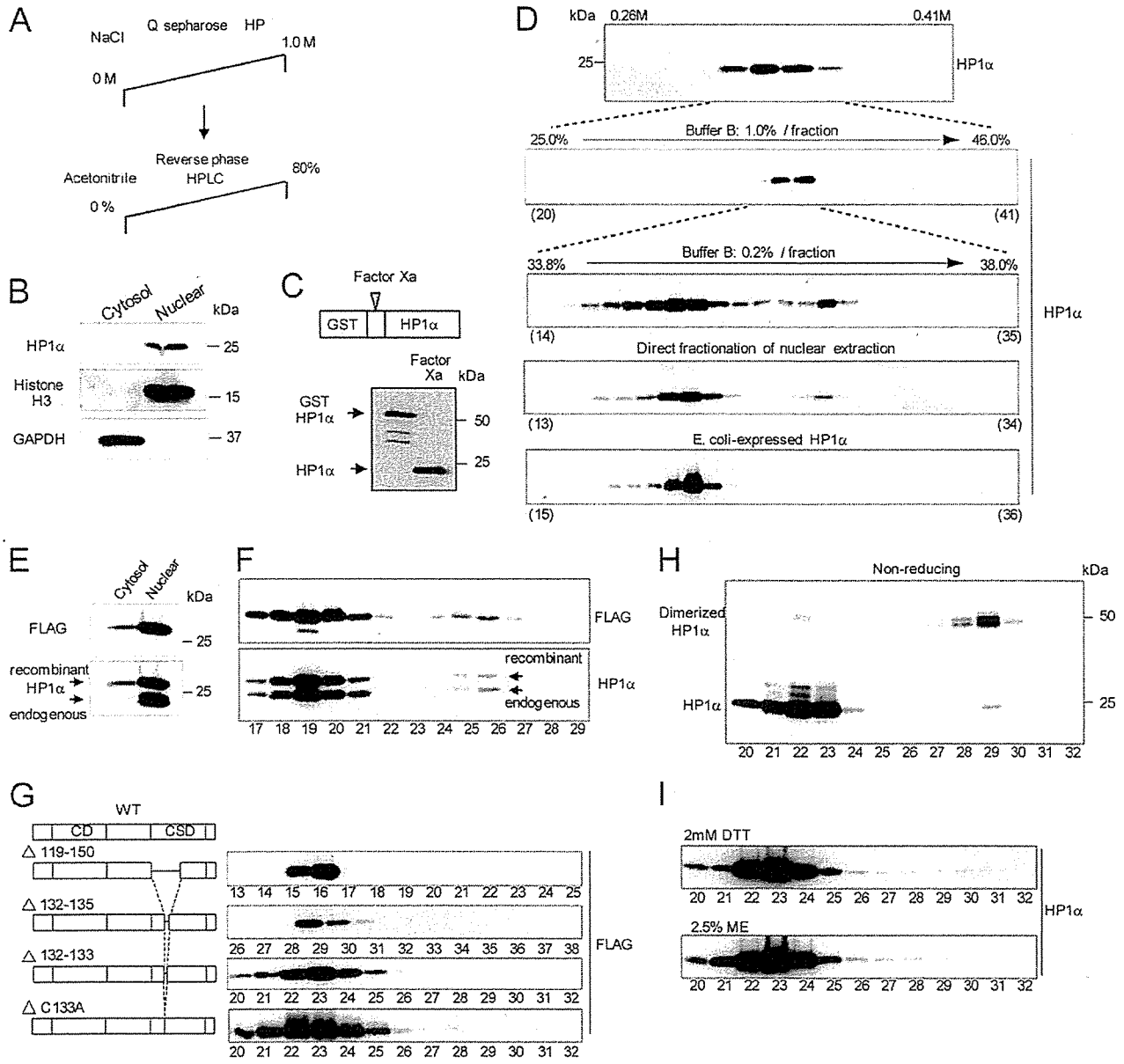

FIGURE 1. **Endogenous HP1α shows a bimodal distribution after protein purification by reverse-phase HPLC.** The late-eluted fraction of HP1α is oxidatively modified to form a disulfide bond. *A*, schematic representation of HP1α purification from cell lysates using sequential column chromatography. *B*, equal quantities of cytosolic and nuclear fractions from HEK293T cells were resolved by SDS-PAGE and probed with the indicated antibodies. *C*, GST-HP1α expressed in *E. coli* was purified and cleaved by Factor Xa (*upper panel*) and detected with anti-HP1α antibody (*lower panel*). *D*, HEK293T cell lysate was fractionated by a Q-Sepharose HP anion-exchange column. Eluted fractions were resolved by reducing SDS-PAGE and probed with anti-HP1α antibody (*top panel*). The *x* axis at the *upper edge* indicates salt concentration. HP1α fractions eluted from the anion-exchange column were next applied to a phenyl reverse-phase column. The fractions were eluted by a fast gradient (buffer B, 1.0% increase of acetonitrile concentration/fraction, *2nd panel from the top*) or by a slow gradient (buffer B, 0.2%/fraction, *3rd panel from the top*). Nuclear extraction from HEK293T cells (*4th panel from the top*) or HP1α purified from *E. coli* (*bottom panel*) was fractionated with the same slow gradient. The eluted fractions were resolved by reducing SDS-PAGE and probed with anti-HP1α antibody. *E*, equal quantities of cytosolic and nuclear fractions from HEK293T cells expressing HP1α-FLAG were resolved by SDS-PAGE and probed with the indicated antibodies. *F*, nuclear extract from HEK293T cells expressing HP1α-FLAG was directly applied to a reverse-phase column, and the eluted fractions were resolved by reducing SDS-PAGE and probed with the indicated antibodies. *G*, diagrams of the representative deletion mutant or point mutant of the HP1α protein during stepwise mutation analysis (*left column*). Nuclear extractions from HEK293T cells expressing each mutant protein were fractionated by reverse-phase HPLC, resolved by SDS-PAGE, and probed with anti-FLAG antibody (*right column*). *H*, endogenous HP1α was purified from the HEK293T cell lysate as shown in *A*. The fractions eluted from the reverse-phase column were resolved by SDS-PAGE under nonreducing conditions and probed with anti-HP1α antibody. *I*, nuclear extract from HEK293T cells was incubated with 2 mM DTT or 2.5% 2-mercaptoethanol (*ME*) for 30 min at 4 °C and then applied to a reverse-phase column. The eluted fractions were resolved by SDS-PAGE and probed with anti-HP1α antibody. *D* and *F–I*, the *x* axis at the *lower edge* indicates fraction numbers.

same bimodal distribution after reverse-phase HPLC (Fig. 1*F*). Thus, we concluded that HP1α-FLAG undergoes the same modification as endogenous HP1α, validating the use of the tagged protein for further analysis. Initially, we attempted to detect the specific modification directly by matrix-assisted laser desorption/ionization and time-of-flight mass spectrometry (MALDI-TOF/MS) (supplemental Fig. S2, *A–C*). Although we detected peptide masses from both fractions corresponding to ~75% of the entire HP1α sequence (supplemental Fig. S2*B*), we did not detect any distinct features in the mass spectra under two different digestion conditions (trypsin or Asp-N) (supplemental Fig. S2*C*). We next tried to detect a modified residue by making multiple, stepwise mutations throughout the entire HP1α molecule. We hypothesized that HP1α-FLAG lacking the modified residue would fractionate into a single peak by reverse-phase HPLC. First, we thoroughly screened the CD and hinge region, both of which are reported to be post-translationally modified (17, 22). However, we could not determine any specific amino acid residue from the mutational analysis (supplemental Fig. S2*D*). Second, we screened the CSD (supplemental Fig. S2*E*) and found that a deletion mutant lacking residues 119–150 (Δ119–150) was eluted as a single peak. We further narrowed down the deleted sequence 119–150 and finally found that a mutant in which cysteine 133 (Cys-133) was replaced by alanine (C133A) was eluted as a single peak (Fig. 1*G*). These data suggest that the single cysteine 133 residue is responsible for the separation of the hydrophobic fraction of HP1α.

Among post-translational modifications of cysteine, oxidation is a common feature. The thiol side chain can be oxidized to sulfenic acid (-SOH), sulfenyl amide (–SN), a disulfide bond (–SS–) or an irreversibly oxidized form (25). We examined the electrophoresis pattern of the two separated fractions of HP1α under nonreducing conditions and found that the hydrophobic form of HP1α shifted to a molecular weight twice its size, indicating that this HP1α formed a homodimer (Fig. 1*H*). In contrast, the mobility of the hydrophilic HP1α was unchanged. Because this dimer was nondissociable both under the strong acidic conditions of the reverse-phase HPLC and under the denaturing conditions during SDS-PAGE, it seemed to be linked by a covalent bond. Pretreatment with reducing agents, such as 2 mM DTT or 2.5% 2-mercaptoethanol, completely abolished the hydrophobic fraction (Fig. 1*I*). Taken together, these data suggest that endogenous HP1α dimerizes by intermolecular disulfide bond formation via Cys-133.

HP1α and HP1γ Both Possess an Isoform-specific Cysteine Residue for Disulfide Bond Formation—The sequence identity among the three HP1 isoforms is remarkably high (Fig. 2*A*), with up to 80% homology in the CSD. However, Cys-133 is specific to HP1α and is replaced by a serine in HP1β and HP1γ (highlighted in *red* in Fig. 2*A*). Therefore, we evaluated whether this oxidative modification was specific for HP1α. Endogenous HP1β was fractionated as a single peak by reverse-phase HPLC. However, endogenous HP1γ was isolated as two separate peaks (Fig. 2*B*). Both the hydrophilic and the hydrophobic fractions of HP1γ were eluted independently of those of HP1α suggesting that these two isoforms did not interact with each other during reverse-phase HPLC fractionation. Similar to HP1α, the hydrophobic form of HP1γ also dimerized (Fig. 2*C*). HP1β contains only two cysteines, both of which are conserved among the isoforms (Cys-59 and Cys-160 of HP1α; highlighted in *blue* in Fig. 2*A*). HP1γ has three cysteines, and one of the cysteines, Cys-177, is an isoform-specific residue located in the C terminus of the CSD. This residue is replaced by tyrosine in HP1α and HP1β (highlighted in *red* in Fig. 2*A*). Mutational analysis of these cysteine residues revealed that only isoform-specific Cys-133 of HP1α and Cys-177 of HP1γ were involved in dimerization (Fig. 2*D*). Mutating the corresponding residues of HP1β, Ser-129 (matched to Cys-133 of HP1α) or Tyr-173 (matched to Cys-177 of HP1γ), to cysteines created the late-eluted hydrophobic form (Fig. 2*E*). These hydrophobic forms of HP1β dimerized similarly with HP1α and HP1γ (Fig. 2*F*). The other two HP1β mutants, S141C and S162C, did not form disulfide bonds. Together, these data suggest that even though their overall structures are highly conserved, endogenous HP1α and HP1γ possess isoform-specific cysteine residues involved in the intermolecular disulfide bond formation. These two positions of the disulfide-linked cysteines are structurally sensitive to oxidation within the CSD.

HP1γ Is More Sensitive to Oxidation than HP1α in Vitro—We tested whether the differences in the positions of the modified cysteine residues between HP1α and HP1γ influenced their sensitivity to oxidation *in vitro*. Under mild oxidative conditions, only a low level of dimerized HP1α was detected even after a long exposure to air oxidation (Fig. 3*A*, *left panels*). In contrast, under the same conditions, HP1γ was easily oxidized to form disulfide bonds (Fig. 3*A*, *right panels*). Treatment with DTT reversed the disulfide formation of HP1γ. These data indicate that HP1γ is more sensitive to oxidation and more readily forms a disulfide dimer *in vitro*.

Using purified and oxidized HP1γ-FLAG, the intermolecular disulfide bond was confirmed by MALDI-TOF/MS analysis. The late-eluted dimerized fraction of HP1γ-FLAG was resolved by nonreducing SDS-PAGE, and the excised band was divided into two samples. One sample was reduced, carbamidomethylated with iodoacetamide, and digested by trypsin. The other sample was directly digested without pretreatment. The expected digested peptide, including Cys-177, consisted of the C terminus of HP1γ and lysine residue within the linker peptide (Fig. 3*B*). The mass spectrum peak of 3084.32, which was detected only in the nonreduced sample, corresponded to the estimated mass of the dimeric peptide connected by a disulfide bond via Cys-177 (3084.35) (Fig. 3*C*, *upper panel*). In contrast, the peak at 1600.68, which was detected only in the reduced sample, corresponded to the estimated mass of the monomeric peptide, including carbamidomethylated Cys-177 (1600.71) (Fig. 3*C*, *lower panel*). No other significant mass spectral peaks from the intermolecular disulfide bond were detected.

HP1γ, but Not HP1α, Readily Forms Disulfide Bonds under in Vivo Oxidative Conditions—We assessed whether this oxidative modification was promoted under *in vivo* oxidative conditions using a pro-oxidant agent, 2-methyl-1,4-naphthoquinone (menadione), which caused oxidative stress in cells (Fig. 4*A*) (26). Menadione treatment caused a dose- and time-dependent increase in the disulfide bond formation of HP1γ in COS7 cells (Fig. 4*B*, *left two panels*). The disulfide dimerization of HP1γ

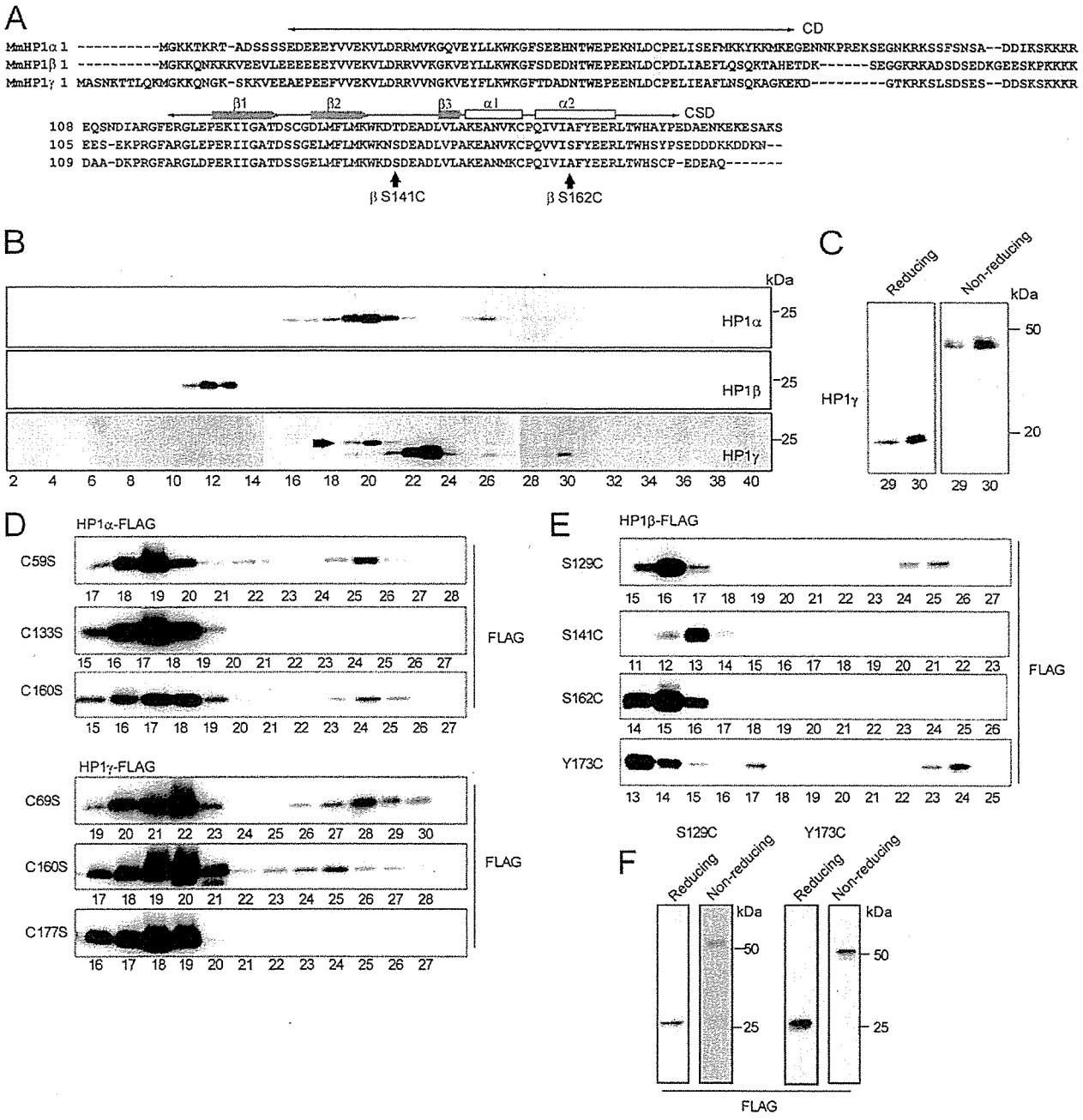

FIGURE 2. **Both HP1α and HP1γ possess isoform-specific cysteine residues that are oxidatively modified to form disulfide bonds.** *A*, amino acid sequence alignment among mouse HP1 isoforms. *Crosswise two-headed arrows* indicate the N-terminal CD and C-terminal CSD. The *bold blue arrow* and *bold white line* along the CSD indicate β-sheet and α-helix, respectively. *Blue highlights* represent the following: two cysteine residues conserved among the HP1 family (Cys-59 and Cys-160; HP1α). *Red highlights* represent the following: position of the cysteine residue specific to HP1α (Cys-133) or HP1γ (Cys-177). The *arrowhead* indicates the position of the mutated HP1β serine residue (shown in *E*). *B*, nuclear extract from HEK293T cells was directly applied to a reverse-phase column, and the eluted fractions were resolved by SDS-PAGE and probed with anti-HP1α, -β, or -γ antibodies. The immunoblotting procedure was performed by consecutive stripping and reprobing with each antibody of the same membrane. The *upper band* of fraction 20 in the *bottom panel* (*arrowhead*) indicates the residual signal from hydrophilic HP1α. *C*, hydrophobic fractions of HP1γ purified from HEK293T cells (as shown in Fig. 1*A*) were resolved by SDS-PAGE under reducing or nonreducing conditions and probed with anti-HP1γ antibody. *D*, nuclear extract from HEK293T cells expressing each HP1α-FLAG (*top three panels*) or HP1γ-FLAG (*bottom three panels*) with a cysteine-to-serine mutation was fractionated by reverse-phase HPLC, resolved by SDS-PAGE, and probed with anti-FLAG antibody. *E*, nuclear extract from HEK293T cells expressing HP1β-FLAG with each serine-to-cysteine or tyrosine-to-cysteine mutation was fractionated by reverse-phase HPLC, resolved by SDS-PAGE, and probed with anti-FLAG antibody. *F*, late-eluted hydrophobic fraction of the HP1β-FLAG mutant (S129C or Y173C) was resolved by reducing or nonreducing SDS-PAGE and probed with anti-FLAG antibody. *B–E*, the *x* axis at the lower edge indicates fraction numbers.

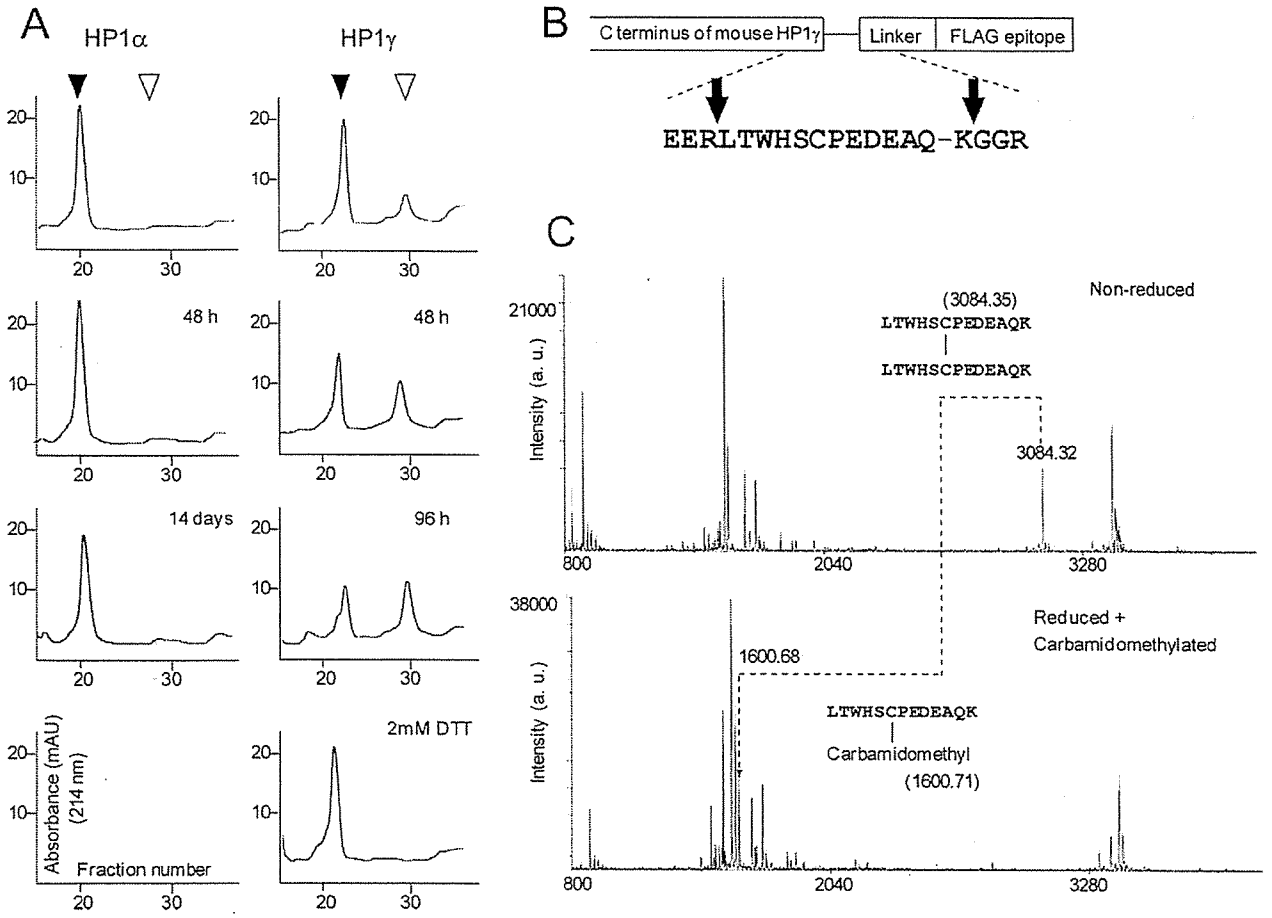

FIGURE 3. **HP1γ is more sensitive to oxidation than HP1α *in vitro*.** MALDI-TOF/MS analysis confirms the disulfide bond formation of HP1γ via Cys-177. *A*, HP1α-FLAG or HP1γ-FLAG expressed in COS7 cells was purified by an anion-exchange column and further fractionated by reverse-phase HPLC. The HPLC absorption pattern profiles at 214 nm are shown. *Black* or *white arrowheads* indicate the fraction of hydrophilic (monomer) or hydrophobic (dimer) forms of HP1, respectively. HP1α-FLAG was fractionated by reverse-phase HPLC immediately after anion exchange (*left top*) or after air oxidation at 4 °C for 48 h or 14 days. HP1γ-FLAG was fractionated immediately after anion exchange (*right top*) or after air oxidation at 4 °C for 48 or 96 h. The HP1γ-FLAG oxidized for 6 days was incubated with 2 mM DTT at 4 °C for 1 h and fractionated by reverse-phase HPLC (*right bottom*). *B*, C-terminal structure of HP1γ-FLAG. *Arrowheads* indicate the trypsin digestion positions. *C*, mass spectra from MALDI-TOF/MS analysis of nonreduced (*upper panel*) or reduced, carbamidomethylated (*lower panel*) HP1γ-FLAG. The expected sequence and estimated mass (*m/z*) of the digested peptide are shown.

was rapidly formed within minutes and was only formed via Cys-177 (Fig. 4*C*). The I165E mutation, which inhibits both noncovalent α-helix dimer formation and proper nuclear localization (6–7), decreased, but not completely, the amount of disulfide dimers of HP1γ (supplemental Fig. S3*A*). These data suggest that the oxidative dimerization of HP1γ requires the proper localization and formation of constitutive, noncovalent dimers.

In contrast to HP1γ, an increase in dimerized HP1α was not observed under the same *in vivo* oxidative conditions (Fig. 4*B*, *right panel*). The dimerized forms of HP1α and HP1γ under basal conditions were almost undetectable without using the large scale purification shown in Fig. 1 because of their relatively low abundance before oxidant treatment. Menadione treatment promoted HP1γ dimerization in various cells, but the extent of dimerization varied among cell types (supplemental Fig. S3*B*), suggesting that the reactivity of HP1γ to reactive oxygen species stimulation varied according to cell type. In each cell, an increase in dimerized HP1α was not observed (data not shown). These results demonstrate that there is a clear difference in oxidation sensitivity among HP1 family members. Although both HP1α and HP1γ have oxidation-sensitive cysteines in their sequences, HP1γ perceives oxidative conditions and is able to more readily form a disulfide dimer than HP1α.

In HEK293T cells, the dimerized HP1γ was subsequently reduced to the monomer form after removal of the oxidant (Fig. 4*D*, *upper panel*), but HP1γ remained dimerized when continuously exposed to the oxidants (Fig. 4*D*, *lower panel*), suggesting that this oxidative modification was reversible.

H_2O_2, known as an endogenous source of reactive oxygen species, also promoted dimerization of HP1γ (Fig. 4*E*). This effect of H_2O_2 was relatively weak in HEK293T cells when compared with the treatment of menadione. However, the same concentration of H_2O_2 substantially increased the amount of dimerized HP1γ in HUVECs (Fig. 4*E*, *lower panel*). Therefore, we further examined the molecular characteristics of the disulfide dimerization of HP1γ using HUVECs.

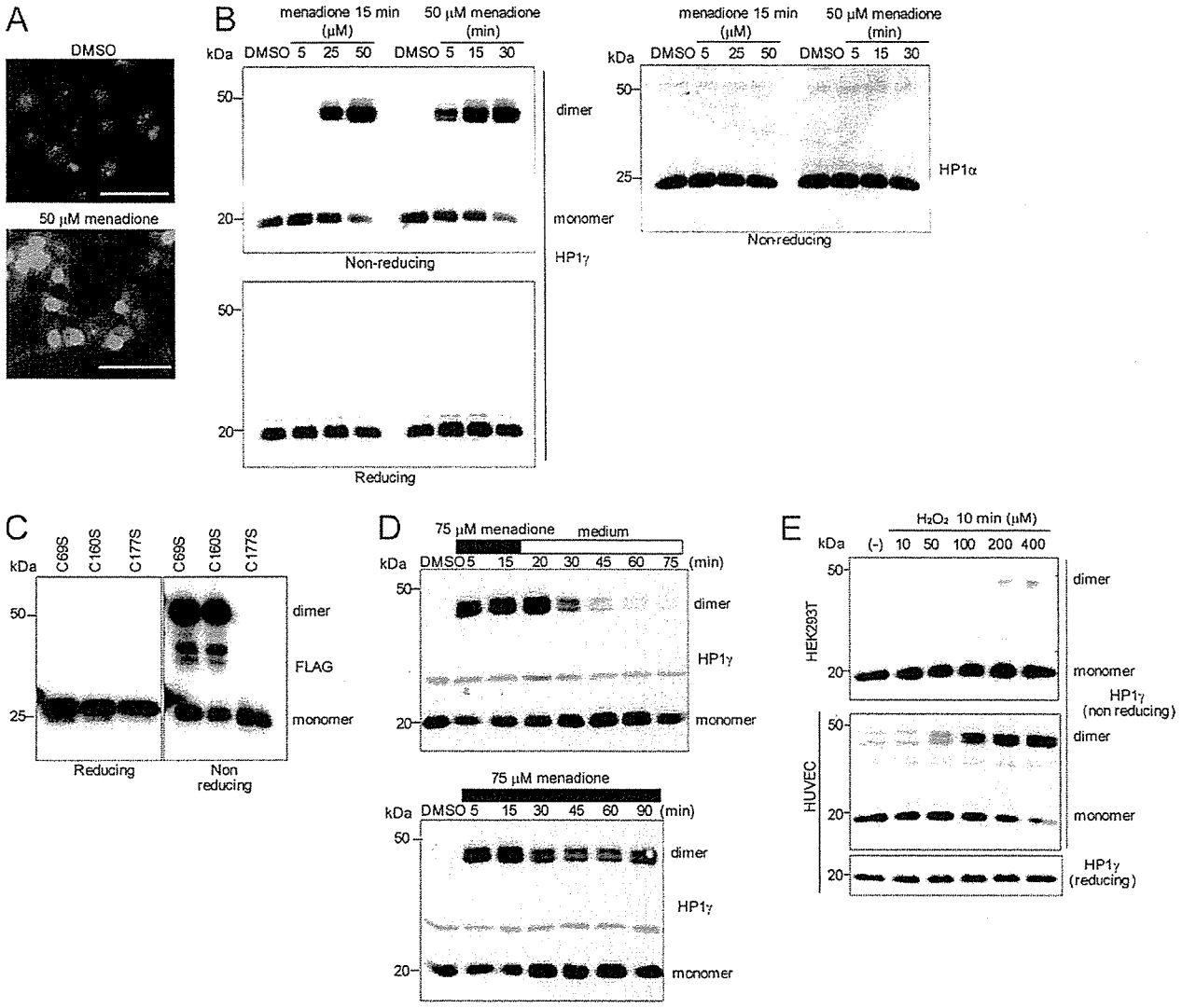

FIGURE 4. **HP1γ, but not HP1α, readily forms disulfide bonds under oxidative conditions.** *A*, after treatment with DMSO or 50 μM menadione for 15 min, COS7 cells were stained with 20 μM dihydroethidium for 30 min and monitored by fluorescence microscopy. *Bar*, 100 μm. *B*, COS7 cells treated with DMSO or menadione under the indicated conditions were lysed, resolved by nonreducing (*upper panel*) or reducing (*lower panel*) SDS-PAGE, and probed with anti-HP1γ antibody. The same membrane was reprobed with anti-HP1α antibody (*right panel*). *C*, COS7 cells expressing each cysteine-to-serine mutant HP1γ-FLAG were treated with 50 μM menadione for 15 min. Lysates were resolved by reducing (*left panel*) or nonreducing (*right panel*) SDS-PAGE and probed with anti-FLAG antibody. *D*, HEK293T cells were treated with 75 μM menadione for 15 min. Subsequently, the culture medium was exchanged for fresh medium (*upper panel*) or kept unchanged (*lower panel*). After incubation for the indicated time, cell lysates were resolved by nonreducing SDS-PAGE and probed with anti-HP1γ antibody. *E*, HEK293T cells and HUVECs were treated with H_2O_2 under the indicated conditions. Cell lysates were resolved by SDS-PAGE and probed with anti-HP1γ antibody. *B–E*, cells were lysed with a buffer (10 mM Tris-HCl, pH 7.2, 150 mM NaCl, 1 mM EDTA, and 1% Nonidet P-40) containing 100 mM maleimide, a thiol-alkylating agent, to prevent artifactual oxidation.

Under Oxidative Conditions, HP1γ Strongly and Transiently Interacts with TIF1β and Holds It in a Chromatin Component—The CSD of HP1, which includes Cys-177 at its C terminus, creates a binding surface for other proteins (27). Therefore, disulfide modification of HP1γ may affect the interactions between HP1 and HP1-binding proteins. Because many candidate effectors that bind to HP1 exist (8), we screened the interacting proteins of HP1γ under oxidative conditions using metabolically radiolabeled HUVECs expressing recombinant HP1γ-FLAG transduced with adenovirus. Among the co-immunoprecipitated proteins, one protein band was detected after treatment with H_2O_2 (Fig. 5*A*, *arrowhead*). The bound protein was purified and analyzed by MALDI-TOF/MS. The amino acid sequence of the digested peptides corresponded to TIF1β (also known as TRIM28 or KAP1), which is a universal co-repressor of gene transcription and is a well known interacting partner of HP1 (28–31). Co-immunoprecipitation analysis showed that endogenous HP1γ strongly interacted with TIF1β in a dose-dependent manner after H_2O_2 treatment (Fig. 5*B*). TIF1β did not interact with HP1γ with a C177S mutation under oxidative conditions, suggesting that the disulfide bond formation of HP1γ enhanced the interaction of these proteins (Fig. 5*C*). When the oxidant was removed, TIF1β dissociated again from HP1γ, suggesting that this enhanced endogenous interac-

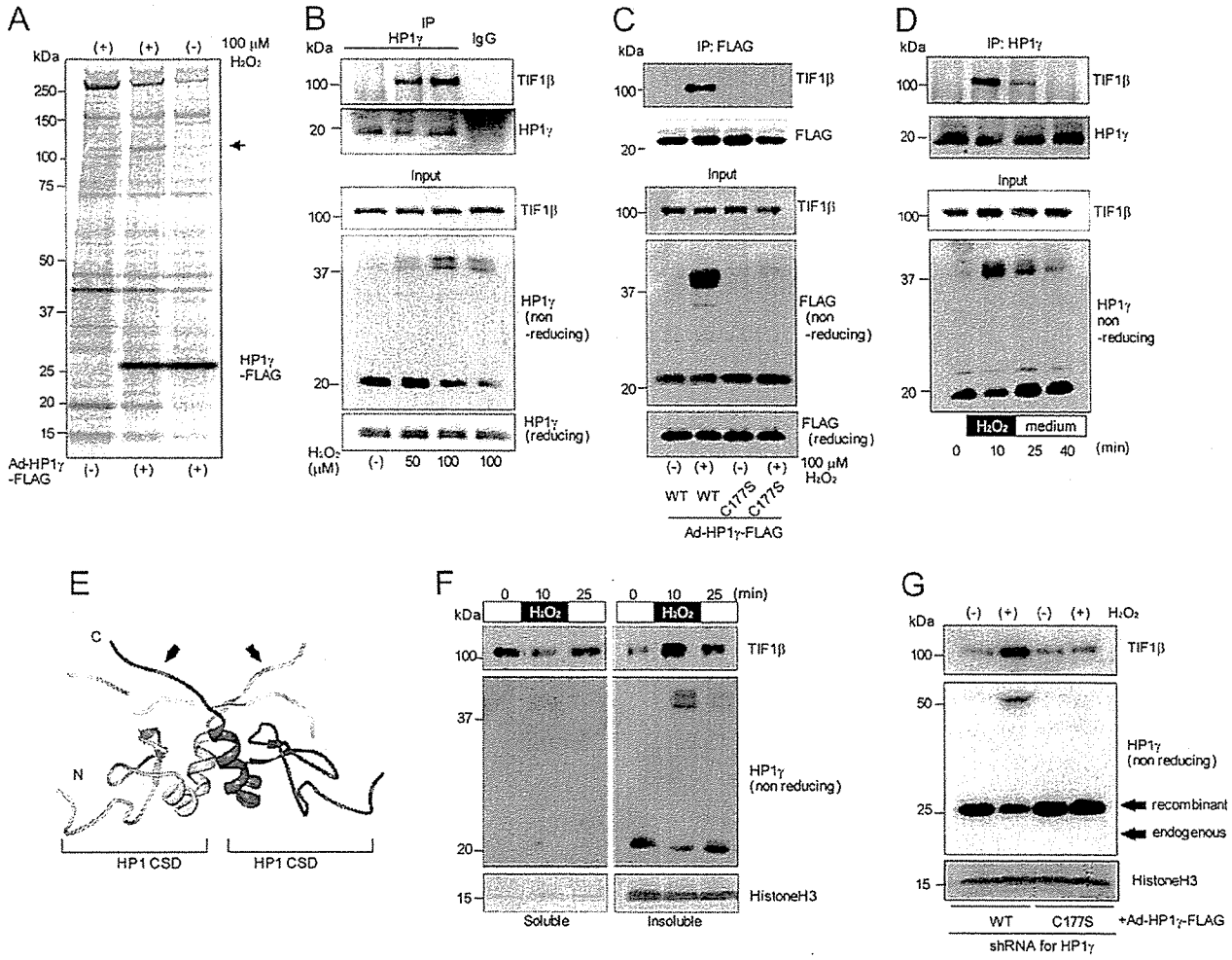

FIGURE 5. **HP1γ strongly interacts with TIF1β and promotes translocation of TIF1β to a chromatin component when dimerized under oxidative conditions.** *A*, HUVECs expressing HP1γ-FLAG (transduced by adenovirus) were metabolically labeled with [^{35}S]cysteine and -methionine for 6 h. Nontransduced cells were also labeled as a negative control. Forty eight h after transduction, the cells were treated with 100 μM H_2O_2 or control (water) for 10 min, lysed, and immunoprecipitated with anti-FLAG M2 affinity gel. Bound samples were resolved by reducing SDS-PAGE and visualized by autoradiography. The *arrow* indicates the protein band co-immunoprecipitated with HP1γ-FLAG only under the oxidative conditions. *B*, lysates from HUVECs treated with control (water) or H_2O_2 for 10 min were immunoprecipitated (*IP*) with anti-HP1γ antibody. Bound samples were resolved by SDS-PAGE and probed with the indicated antibodies. *C*, HUVECs expressing WT or C177S HP1γ-FLAG (transduced by adenovirus) were treated with 100 μM H_2O_2 for 10 min. Lysates were immunoprecipitated with anti-FLAG M2 affinity gel, and bound samples were resolved by SDS-PAGE and probed with the indicated antibodies. *D*, HUVECs were transiently treated with 100 μM H_2O_2. Lysates were immunoprecipitated with anti-HP1γ antibody, and bound samples were resolved by SDS-PAGE and probed with the indicated antibodies. *E*, structure of HP1 CSD noncovalent homodimer (*blue* and *cyan*) and PXVXL motif (*yellow*) complex (Protein Data Bank code 1s4z, modified using the WEB tool (43)). The position of Cys-177 in HP1γ is highlighted in *red* (*black arrows*). *F*, HUVECs were transiently treated with 100 μM H_2O_2. Soluble and insoluble nuclear fractions were obtained using Triton extraction. Each sample was resolved by SDS-PAGE and probed with the indicated antibodies. *G*, HUVECs were transduced with lentivirus expressing shRNA against HP1γ and adenovirus expressing shRNA-resistant HP1γ-FLAG WT or C177S mutant. Triton-insoluble fractions from these cells after H_2O_2 treatment were resolved by SDS-PAGE and probed with the indicated antibodies.

tion was transient (Fig. 5*D*). Structurally, disulfide dimerization via Cys-177 is formed at the C terminus of the CSD, just adjacent to the binding interface for the PXVXL motif, which is a well characterized binding sequence in HP1-interacting proteins, including TIF1β (Fig. 5*E*) (7).

We next examined the localization changes of these proteins before and after oxidant treatment. No remarkable change in localization was detected by immunostaining (data not shown). However, biochemical analysis using Triton extraction verified the TIF1β translocation. HP1γ existed mainly in the Triton-insoluble chromatin component, whereas TIF1β was distributed both in the soluble and the insoluble components (Fig. 5*F*). Under oxidative conditions, HP1γ dimerized and was maintained in the insoluble components. Concomitant with HP1γ dimerization, the insoluble component of TIF1β transiently increased. The knockdown of endogenous HP1γ combined with the replacement by a C177S mutant of HP1γ inhibited the translocation of TIF1β, suggesting that HP1γ held TIF1β on chromatin only when oxidized via Cys-177 (Fig. 5*G*). These data suggest that the intracellular redox state is transduced to the conformational and localization change of the repressor complex via oxidative modification of HP1γ.

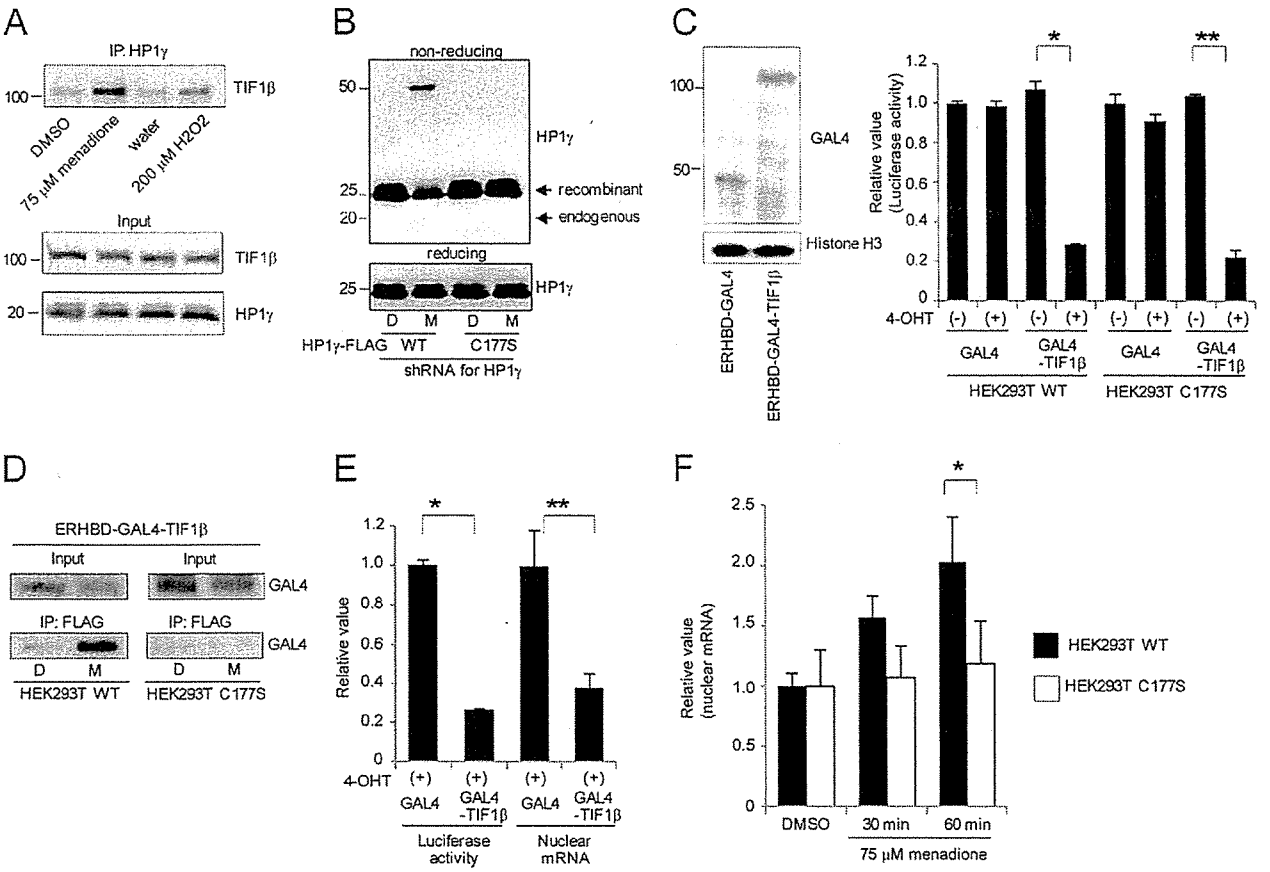

FIGURE 6. **Dimerized HP1γ under oxidative conditions inhibits the repression ability of TIF1β.** *A*, lysates from HEK293T cells treated with DMSO, 75 μM menadione, water, or 200 μM H_2O_2 for 15 min were immunoprecipitated (*IP*) with anti-HP1γ antibody. Bound samples were resolved by SDS-PAGE and probed with the indicated antibodies. *B*, HEK293T cells stably expressing shRNA for HP1γ and shRNA-resistant recombinant FLAG-tagged HP1γ were treated with DMSO or 75 μM menadione for 15 min. Cell lysates were resolved by nonreducing or reducing SDS-PAGE and probed with anti-HP1γ antibody. *D* indicates DMSO, and *M* indicates 75 μM menadione. *C*, lysates from HEK293T stable cells transfected with an ERHBD-GAL4 or ERHBD-GAL4-TIF1β fusion protein were resolved by SDS-PAGE and probed with the indicated antibodies (*left panel*). HEK293T stable cells were transfected with the plasmids encoding ERHBD-GAL4 or ERHBD-GAL4-TIF1β with the reporter plasmids. Twenty four h after transfection, 4-OHT was added to culture medium (500 nM). Forty eight h after transfection, luciferase activity was measured (*right panel*). The relative value was corrected by the value of the cells transfected with ERHBD-GAL4 without 4-OHT induction. Student's *t* test; *, **, $p < 0.01$. *D*, HEK293T stable cells expressing ERHBD-GAL4-TIF1β were treated with DMSO or 75 μM menadione for 15 min. Lysates were immunoprecipitated with anti-FLAG affinity gel. Bound samples were immunoblotted with anti-GAL4 antibody. *D* indicates DMSO, and *M* indicates 75 μM menadione. *E*, under the same conditions as *C*, luciferase transcription levels were determined both by protein enzymatic activity and intranuclear mRNA levels measured by quantitative PCR. Student's *t* test; *, **, $p < 0.01$. *F*, HEK293T stable cells expressing ERHBD-GAL4-TIF1β with 500 nM 4-OHT induction were treated with DMSO for 60 min or 75 μM menadione for the indicated time. Intranuclear luciferase mRNA levels at each time point were measured by quantitative PCR. The relative value was corrected by the value of the cells treated with DMSO. Two-way repeated measure analysis of variance; *, $p < 0.05$. The means ± S.D. as indicated by the *error bars* were determined from three independent experiments.

Dimerized HP1γ under Oxidative Conditions Inhibits the Repression Ability of TIF1β—To clarify whether the repression ability of TIF1β was promoted or inhibited when trapped by HP1γ under oxidative conditions, we used a GAL4-based transcriptional reporter assay. In HEK293T cells, menadione treatment promoted the disulfide dimerization of HP1γ and the interaction between HP1γ and TIF1β more prominently than H_2O_2 treatment (supplemental Fig. S3*B* and Figs. 4*E* and 6*A*). Therefore, we used menadione treatment for further analysis in HEK293T cells. We generated HEK293T cells stably expressing shRNA for HP1γ and shRNA-resistant recombinant FLAG-tagged HP1γ WT or C177S mutant. In these cells, endogenous HP1γ was almost completely depleted and was replaced by the dimerizable or undimerizable recombinant proteins (Fig. 6*B*). To evaluate the transcriptional repression ability of TIF1β, we transfected the plasmids encoding ERHBD-GAL4 as a control or ERHBD-GAL4-TIF1β fusion protein with the reporter plasmids in these cells (12, 32). The transcriptional regulatory activity of the ERHBD fusion protein is post-translationally controlled by the addition of 4-OHT to the culture medium (12). In our experimental conditions where ERHBD-GAL4 and ERHBD-GAL4-TIF1β were equally expressed (Fig. 6*C*, *left panel*), only ERHBD-GAL4-TIF1β repressed transcription of luciferase with 4-OHT (500 nM) in the HEK293T stable cells (Fig. 6*C*, *right panel*). The extent of repression was similar between the cells expressing either the HP1γ-FLAG WT or the C177S mutant under nonoxidative conditions. When the cells were treated with menadione, HP1γ-FLAG WT strongly interacted with ERHBD-GAL4-TIF1β as was similarly observed with endogenous proteins (Fig. 6*D*). To examine the transcrip-

tional change of the luciferase gene under oxidative conditions, we measured the intranuclear mRNA levels of luciferase by quantitative PCR instead of luciferase protein enzymatic activity (Fig. 6*E*). We chose this end point because the oxidation of HP1γ was too rapid to properly evaluate its effect on luciferase transcription by measuring luciferase protein enzymatic activity. Under these conditions, menadione treatment relieved the levels of luciferase transcription repressed by ERHBD-GAL4-TIF1β in the cells expressing HP1γ-FLAG WT but did not relieve the levels in the cells expressing the C177S mutant (Fig. 6*F*). These data suggest that dimerized HP1γ under oxidative conditions inhibits the repression ability of TIF1β.

It remained unclear whether the intranuclear redox-sensing mechanism through the oxidative modification of HP1γ plays a role in the cellular response to extrinsic oxidative stress. Therefore, we assessed the effect of this modification on cell survival under oxidative conditions using HEK293T cells stably expressing shRNA against HP1γ (supplemental Fig. S4*A*). Depletion of HP1γ using shRNA uniformly decreased cell viability under oxidative conditions induced by menadione treatment (supplemental Fig. S4*B*). For a rescue experiment, these stable clones were transduced with an adenoviral vector encoding WT HP1γ-FLAG or C177S HP1γ-FLAG. Both HP1γ vectors were cloned from murine cDNA and were resistant to shRNA against human HP1γ. Transduction of both adenoviral constructs at a multiplicity of infection of 20 resulted in nearly equal expression of recombinant HP1γ with endogenous HP1γ and yielded a similar disulfide dimerization pattern (supplemental Fig. S4*C*). Under these conditions, WT HP1γ-FLAG rescued cell viability after menadione treatment in each stable clone, but the C177S HP1γ-FLAG mutant did not rescue cell viability (supplemental Fig. S4*D*). These results suggest that HP1γ disulfide dimerization plays a pivotal role in cell survival under oxidative conditions.

DISCUSSION

In this study, we identified isoform-specific disulfide bond formation, which is a novel post-translational modification of HP1, using a unique column chromatography method. Biochemical analysis revealed two isoform-specific reactive cysteine residues, cysteine 133 in HP1α and cysteine 177 in HP1γ. In particular, HP1γ readily and reversibly formed disulfide dimers under oxidative conditions. Dimerized HP1γ strongly interacted with TIF1β and held it in a chromatin component. The GAL4 tethering repression assay revealed that the tight interaction of the repressor proteins had a reversing effect for transcriptional repression.

Several post-translational modifications of HP1 have been reported. Specifically, the linker region between the CSD and CD is highly amenable to post-translational modifications, especially phosphorylation that affects silencing activity or nuclear location of HP1 (17, 33–35). Also in the CD, Thr-51 of HP1β has been shown to be phosphorylated in response to DNA damage (22). More recently, a comprehensive proteomic analysis revealed that all HP1 isoforms are highly modified by phosphorylation, acetylation, methylation, and formylation both in the CD and in the CSD (36). Prior to this study, however, no oxidative modification of HP1 had been identified. Because oxidative modifications at cysteine residues would be easily disrupted under reducing conditions, such modifications may be detected only by the unique HPLC-based method used in this study and not by ordinary mass spectrometry analysis.

Both isoform-specific cysteines involved in forming disulfide bonds reside in a structurally flexible region of the CSD. Cys-133 of HP1α lies in the long loop between the β1 and β2 sheets, and Cys-177 of HP1γ lies in the C-terminal region. Introducing cysteine residues into these flexible sites of HP1β conferred the ability to form disulfide bonds, suggesting that these sites have specific structures in the oxidative center. Although both cysteines were reactive, a distinct difference of sensitivity to oxidation existed. Each location of reactive cysteines and the surrounding structure might determine the sensitivity of HP1α and -γ to oxidation. Under both *in vitro* and *in vivo* oxidative conditions, HP1γ readily formed disulfide bonds. In contrast, only minimal disulfide formation of HP1α by oxidation was observed under our experimental conditions. The reactivity of HP1α under oxidation might be observed under different conditions. Nonetheless, the isoform specificity and functional importance of Cys-133 in HP1α has been reported previously (15).

HP1 has been reported to form dimers via the CSD, but these dimers are not mediated by disulfide bonds or other covalent bonds (6, 37, 38). Thus, HP1 dimerizes in at least two ways. The interface of the noncovalently linked dimer involves a symmetrical interaction on helix α2 of the CSD (27) and creates a nonpolar groove structure, which is a binding site for the PXVXL motif in HP1-interacting proteins, such as TIF1β (Fig. 5*E*) (7). Because reactive cysteine 177 in HP1γ is located in the C terminus adjacent to the groove structure, disulfide bond formation at this site likely affects the binding affinity of HP1γ. Indeed, HP1γ strongly and transiently interacted with TIF1β and promoted its translocation to a chromatin component stringently depending on the oxidative status of cysteine 177. This rapid reacting mechanism to transduce cellular redox state to a conformational change like a clear "on-off switch" suggests that HP1γ is a functional redox sensor.

During the cellular response to oxidative stress, an increase in oxidants can trigger alterations in transcription levels through direct activation or by promoting a change in the subcellular localization of transcription factors by oxidizing reactive cysteine residues (25). Among these oxidative responses, the disulfide dimerization of HP1γ demonstrated in this study appears to be one of the most rapid transcriptional regulatory mechanisms. TIF1β is a universal co-repressor for the Krüppel-associated box domain containing the zinc finger protein (KRAB-ZNF) family of transcription factors, and it is the major protein binding the CSD of HP1 (28–31). TIF1β also works as a scaffold for the repressor complex, and its interaction with HP1 is essential for its repression activity (12, 39–41). Recent findings have revealed that the binding of HP1 to TIF1β is essential for their coordinated function on the promoter of the endogenous genes (42). Therefore, the reversing effect for the repressive ability of TIF1β caused by HP1γ disulfide dimerization might be required for a short period of adaptation against oxidative stress. Downstream genes regulated by these scaffold complexes remain to be clarified in the future analysis.

In conclusion, our study suggests that HP1 potentially acts as a rapid redox sensor, and it may connect the intracellular redox state with transcriptional regulation under various physiological conditions.

Acknowledgments—We thank David C. Schultz and Takahiro Nagase for the plasmid constructs. We thank Saori Ikezawa and Yoko Hamada for technical assistance and Yasunori Shintani for thoughtful discussions.

REFERENCES

1. James, T. C., and Elgin, S. C. (1986) *Mol. Cell. Biol.* **6**, 3862–3872
2. Wallrath, L. L. (1998) *Curr. Opin. Genet. Dev.* **8**, 147–153
3. Bannister, A. J., Zegerman, P., Partridge, J. F., Miska, E. A., Thomas, J. O., Allshire, R. C., and Kouzarides, T. (2001) *Nature* **410**, 120–124
4. Nakayama, J., Rice, J. C., Strahl, B. D., Allis, C. D., and Grewal, S. I. (2001) *Science* **292**, 110–113
5. Lachner, M., O'Carroll, D., Rea, S., Mechtler, K., and Jenuwein, T. (2001) *Nature* **410**, 116–120
6. Brasher, S. V., Smith, B. O., Fogh, R. H., Nietlispach, D., Thiru, A., Nielsen, P. R., Broadhurst, R. W., Ball, L. J., Murzina, N. V., and Laue, E. D. (2000) *EMBO J.* **19**, 1587–1597
7. Thiru, A., Nietlispach, D., Mott, H. R., Okuwaki, M., Lyon, D., Nielsen, P. R., Hirshberg, M., Verreault, A., Murzina, N. V., and Laue, E. D. (2004) *EMBO J.* **23**, 489–499
8. Grewal, S. I., and Jia, S. (2007) *Nat. Rev. Genet.* **8**, 35–46
9. Lomberk, G., Wallrath, L., and Urrutia, R. (2006) *Genome Biol.* **7**, 228
10. Schultz, D. C., Ayyanathan, K., Negorev, D., Maul, G. G., and Rauscher, F. J., 3rd. (2002) *Genes Dev.* **16**, 919–932
11. Maison, C., and Almouzni, G. (2004) *Nat. Rev. Mol. Cell Biol.* **5**, 296–304
12. Sripathy, S. P., Stevens, J., and Schultz, D. C. (2006) *Mol. Cell. Biol.* **26**, 8623–8638
13. Cammas, F., Janoshazi, A., Lerouge, T., and Losson, R. (2007) *Differentiation* **75**, 627–637
14. Filesi, I., Cardinale, A., van der Sar, S., Cowell, I. G., Singh, P. B., and Biocca, S. (2002) *J. Cell Sci.* **115**, 1803–1813
15. Nielsen, A. L., Sanchez, C., Ichinose, H., Cerviño, M., Lerouge, T., Chambon, P., and Losson, R. (2002) *EMBO J.* **21**, 5797–5806
16. Vassallo, M. F., and Tanese, N. (2002) *Proc. Natl. Acad. Sci. U.S.A.* **99**, 5919–5924
17. Lomberk, G., Bensi, D., Fernandez-Zapico, M. E., and Urrutia, R. (2006) *Nat. Cell Biol.* **8**, 407–415
18. Gilbert, N., Boyle, S., Sutherland, H., de Las Heras, J., Allan, J., Jenuwein, T., and Bickmore, W. A. (2003) *EMBO J.* **22**, 5540–5550
19. Ritou, E., Bai, M., and Georgatos, S. D. (2007) *J. Cell Sci.* **120**, 3425–3435
20. Mateescu, B., Bourachot, B., Rachez, C., Ogryzko, V., and Muchardt, C. (2008) *EMBO Rep.* **9**, 267–272
21. Vakoc, C. R., Mandat, S. A., Olenchock, B. A., and Blobel, G. A. (2005) *Mol. Cell* **19**, 381–391
22. Ayoub, N., Jeyasekharan, A. D., Bernal, J. A., and Venkitaraman, A. R. (2008) *Nature* **453**, 682–686
23. Petta, T. B., Nakajima, S., Zlatanou, A., Despras, E., Couve-Privat, S., Ishchenko, A., Sarasin, A., Yasui, A., and Kannouche, P. (2008) *EMBO J.* **27**, 2883–2895
24. Asano, Y., Takashima, S., Asakura, M., Shintani, Y., Liao, Y., Minamino, T., Asanuma, H., Sanada, S., Kim, J., Ogai, A., Fukushima, T., Oikawa, Y., Okazaki, Y., Kaneda, Y., Sato, M., Miyazaki, J., Kitamura, S., Tomoike, H., Kitakaze, M., and Hori, M. (2004) *Nat. Genet.* **36**, 123–130
25. D'Autréaux, B., and Toledano, M. B. (2007) *Nat. Rev. Mol. Cell Biol.* **8**, 813–824
26. Oka, S., Ohno, M., Tsuchimoto, D., Sakumi, K., Furuichi, M., and Nakabeppu, Y. (2008) *EMBO J.* **27**, 421–432
27. Cowieson, N. P., Partridge, J. F., Allshire, R. C., and McLaughlin, P. J. (2000) *Curr. Biol.* **10**, 517–525
28. Friedman, J. R., Fredericks, W. J., Jensen, D. E., Speicher, D. W., Huang, X. P., Neilson, E. G., and Rauscher, F. J., 3rd. (1996) *Genes Dev.* **10**, 2067–2078
29. Kim, S. S., Chen, Y. M., O'Leary, E., Witzgall, R., Vidal, M., and Bonventre, J. V. (1996) *Proc. Natl. Acad. Sci. U.S.A.* **93**, 15299–15304
30. Le Douarin, B., Nielsen, A. L., Garnier, J. M., Ichinose, H., Jeanmougin, F., Losson, R., and Chambon, P. (1996) *EMBO J.* **15**, 6701–6715
31. Moosmann, P., Georgiev, O., Le Douarin, B., Bourquin, J. P., and Schaffner, W. (1996) *Nucleic Acids Res.* **24**, 4859–4867
32. Itokawa, Y., Yanagawa, T., Yamakawa, H., Watanabe, N., Koga, H., and Nagase, T. (2009) *Biochem. Biophys. Res. Commun.* **388**, 689–694
33. Koike, N., Maita, H., Taira, T., Ariga, H., and Iguchi-Ariga, S. M. (2000) *FEBS Lett.* **467**, 17–21
34. Zhao, T., Heyduk, T., and Eissenberg, J. C. (2001) *J. Biol. Chem.* **276**, 9512–9518
35. Badugu, R., Yoo, Y., Singh, P. B., and Kellum, R. (2005) *Chromosoma* **113**, 370–384
36. Leroy, G., Weston, J. T., Zee, B. M., Young, N. L., Plazas-Mayorca, M. D., and Garcia, B. A. (2009) *Mol. Cell. Proteomics* **8**, 2432–2442
37. Wang, G., Ma, A., Chow, C. M., Horsley, D., Brown, N. R., Cowell, I. G., and Singh, P. B. (2000) *Mol. Cell. Biol.* **20**, 6970–6983
38. Nielsen, A. L., Oulad-Abdelghani, M., Ortiz, J. A., Remboutsika, E., Chambon, P., and Losson, R. (2001) *Mol. Cell* **7**, 729–739
39. Nielsen, A. L., Ortiz, J. A., You, J., Oulad-Abdelghani, M., Khechumian, R., Gansmuller, A., Chambon, P., and Losson, R. (1999) *EMBO J.* **18**, 6385–6395
40. Ayyanathan, K., Lechner, M. S., Bell, P., Maul, G. G., Schultz, D. C., Yamada, Y., Tanaka, K., Torigoe, K., and Rauscher, F. J., 3rd. (2003) *Genes Dev.* **17**, 1855–1869
41. Smallwood, A., Black, J. C., Tanese, N., Pradhan, S., and Carey, M. (2008) *Nat. Struct. Mol. Biol.* **15**, 318–320
42. Riclet, R., Chendeb, M., Vonesch, J. L., Koczan, D., Thiesen, H. J., Losson, R., and Cammas, F. (2009) *Mol. Biol. Cell* **20**, 296–305
43. Moreland, J. L., Gramada, A., Buzko, O. V., Zhang, Q., and Bourne, P. E. (2005) *BMC Bioinformatics* **6**, 21

THE JOURNAL OF BIOLOGICAL CHEMISTRY VOL. 285, NO. 34, pp. 26652–26661, August 20, 2010

Novel Phorbol Ester-binding Motif Mediates Hormonal Activation of Na^+/H^+ Exchanger*[S]

Received for publication, April 2, 2010, and in revised form, June 2, 2010 Published, JBC Papers in Press, June 15, 2010, DOI 10.1074/jbc.M110.130120

Shigeo Wakabayashi[1], Tomoe Y. Nakamura, Soushi Kobayashi, and Takashi Hisamitsu

From the Department of Molecular Physiology, National Cerebral and Cardiovascular Center Research Institute, Fujishirodai 5-7-1, Suita, Osaka 565-8565, Japan

Protein kinase C (PKC) is considered crucial for hormonal Na^+/H^+ exchanger (NHE1) activation because phorbol esters (PEs) strongly activate NHE1. However, here we report that rather than PKC, direct binding of PEs/diacylglycerol to the NHE1 lipid-interacting domain (LID) and the subsequent tighter association of LID with the plasma membrane mainly underlies NHE1 activation. We show that (i) PEs directly interact with the LID of NHE1 *in vitro*, (ii) like PKC, green fluorescent protein (GFP)-labeled LID translocates to the plasma membrane in response to PEs and receptor agonists, (iii) LID mutations markedly inhibit these interactions and PE/receptor agonist-induced NHE1 activation, and (iv) PKC inhibitors ineffectively block NHE1 activation, except staurosporin, which itself inhibits NHE1 via LID. Thus, we propose a PKC-independent mechanism of NHE1 regulation via a PE-binding motif previously unrecognized.

Tumor-promoting phorbol esters (PEs)[2] have been used to validate the involvement of protein kinase C (PKC) in the functions of many proteins and in cellular processes (1, 2). The ubiquitous Na^+/H^+ exchanger (NHE1 isoform) is a well-documented PE-activated membrane protein (3–5) that has long been believed to be activated via PKC (6). NHE1 catalyzes electroneutral Na^+/H^+ exchange and is an important regulator of intracellular pH (pH_i), Na^+ concentration, and cell volume (6–10). NHE1 is activated in response to various stimuli, including hormones, growth factors, and mechanical stress, and thereby optimizing the intracellular ionic environment for many cellular functions including cell proliferation, cell migration, and volume regulation (6–10). Furthermore, this activation is also thought to be involved in the pathogenesis of diseases, such as cancer and heart failure (11–13). Regulation of NHE1 is thought to occur through the interaction of multiple signaling molecules with the carboxyl (C)-terminal cytoplasmic domain of NHE1, their post-translational modifications, and subsequent conformational changes in the amino (N)-terminal transmembrane domain responsible for catalyzing the Na^+/H^+ exchange reaction (6, 10) (see Fig. 1*A* for membrane topology). Furthermore, this regulation is attributable to a change in the affinity for intracellular H^+ (6, 14, 15). Of the signaling molecules, calcineurin B homologous protein 1 (CHP1, a ubiquitous isoform of CHPs) was suggested to play an essential role in maintaining the structure/function of NHE1 as an obligatory subunit (16, 17). However, neither NHE1 nor CHP1 is phosphorylated by PKC *in vitro*.[3] Thus, at present, conclusive evidence for PKC involvement and the detailed molecular mechanism underlying NHE1 activation remain elusive.

We predicted that NHE1 is activated through PKC-independent mechanisms such as direct interaction with PE/diacylglycerol (DAG). The NHE1 region adjacent to the CHP-binding site (18, 19) was reported to bind phosphatidylinositol 4,5-bisphosphate (PIP_2), a membrane phospholipid, and to be critical for maintaining basal exchange activity (20, 21). Because this ~60-residue region (Fig. 1*A*), which includes the PIP_2-binding site, is also essential for hormonal NHE1 activation (6, 22, 23), we hypothesized that change in the interaction of this region (lipid-interacting domain, LID) with cell membranes may be critical for regulation of NHE1. Here, we investigated the biochemical properties of LID, and found that it contains a novel PE/DAG-binding domain, which plays a critical role in NHE1 regulation.

EXPERIMENTAL PROCEDURES

Molecular Biology—The template plasmid carrying cDNA coding for the NHE1 human isoform with some unique restriction sites cloned into the pECE mammalian expression vector has been described previously (24). All the constructs were produced by a polymerase chain reaction (PCR)-based strategy as described previously (24). In brief, PCR products generated using forward and reverse primers were inserted into the appropriate restriction sites of expression vectors. For construction of GFP- or mCherry-tagged wild-type and mutant LID, the cytoplasmic region (amino acids 542–598) of NHE1 was amplified by PCR using pECE constructs as templates and inserted into mammalian expression vectors, pEGFP-C1 or pmCherry-C1 (BD Biosciences Clontech, Palo Alto, CA),

* This work was supported by a Grant-in-Aid for Scientific Research on Priority Areas 18077015 and Grants-in-Aid for Scientific Research (B) 19390080, a grant for the Promotion of Fundamental Studies in Health Sciences from the National Institute of Biomedical Innovation (NIBIO), research grants for Cardiovascular Diseases (20C-3 and 21A-13), and a grant (nano-006) for Research on Advanced Medical Technology from the Ministry of Health, Labour, and Welfare of Japan.

[S] The on-line version of this article (available at http://www.jbc.org) contains supplemental Figs. S1–S8 and movies S1–S10.

[1] To whom correspondence should be addressed. Tel.: 81-6-6833-5012 (ext. 2519); Fax: 06-6835-5314; E-mail: wak@ri.ncvc.go.jp.

[2] The abbreviations used are: PE, phorbol ester; FRET, fluorescence resonance energy transfer; SAPD, sapintoxin D; PC, phosphatidylcholine; PEt, phosphatidylethanolamine; PG, phosphatidylglycerol; PA, phosphatidic acid; PI, phosphatidylinositol; PIP_2, phosphatidylinositol 4,5-bisphosphate; Ch, cholesterol; SM, sphingomyelin; LID, lipid-interacting domain.

[3] S. Wakabayashi, unpublished observations.

respectively. For construction of mCherry-PKCδ-C1a, PKCδ-C1a domain (amino acids 159–208) of cloned human PKCδ was amplified and inserted into pmCherry-C1 vector, and for construction of MARCKS-GFP, the entire coding region of cloned human MARCKS was inserted into pEGFP-N1 vector. The cDNA coding for mouse α1-adrenergic receptor was purchased from Invitrogen and cloned into the expression vector pT-REx-DEST30 (Invitrogen). GFP-labeled PLCδ-PH domain (25) was kindly provided by Dr. Tobias Meyer (Stanford University). The DNA sequences of the PCR fragments were confirmed using an Applied Biosystems Model 3130 autosequencer.

Confocal Microscopy—Exchanger-deficient PS120 cells (26) or PS120 cells stably expressing the wild-type NHE1 (our basic confocal observations described in this report did not differ across these two cell types) were co-transfected with GFP- or mCherry-labeled LID and other constructs for 6–8 h by Lipofectamine 2000 (Invitrogen, CA). Cells were trypsinized and plated onto glass-bottom 35-mm dishes. Fluorescent signals were observed by confocal microscopy with an Olympus Fluoview FV1000 confocal microscope 16–24 h after trypsinization. Various reagents such as PMA, OAG, and receptor agonists were added directly to dishes at 22–25 °C. Imaging data were usually taken each 15 or 30 s over 10–20 min. Changes in fluorescence intensities around plasma membranes (Figs. 1*C* and 6*D*) were analyzed using Image-Pro Plus software (Media Cybernetics Inc.). Fluorescence intensities in areas including plasma membranes and the whole cells were measured after these areas were selected by eye through an experimental series. Statistical analysis of colocalization was performed using software included with the confocal system (Fig. 1*D*). For co-transfection with mCherry-LID and GFP-PLCδ-PH (supplemental Figs. S5 and S6), line scanning of fluorescence intensity was performed at each cell, and fluorescence intensities in plasma membrane (I_{mem}) and cytosol (I_{cyt}) were measured using Image-Pro Plus software (Media Cybernetics, Inc.). The relative membrane-localization index $(I_{mem} - I_{cyt})/(I_{mem} + I_{cyt})$ was calculated as described (25).

Transfection of NHE1 Variants—In this experiment, we first stably transfected PS120 cells with mouse α1-adrenergic receptor under selection with G418. The cDNAs encoding the wild-type and mutant NHE1 variants were transfected by Lipofectamine 2000 (Invitrogen) into either PS120 or PS120 cells expressing α1-adrenergic receptor. Stable cell populations with Na^+/H^+ exchange activity were selected by acid-killing selection procedure as previously described (22).

Measurement of pH_i Change—Extracellular stimuli-induced change in pH_i was measured using the dual-excitation ratiometric pH-indicator BCECF/AM, as previously described (27). Briefly, cells expressing NHE1 variants were serum-depleted more than 2 h and loaded for 3 min with 0.3 μM BCECF/AM (Invitrogen) at room temperature in HEPES-buffered saline (HBS) containing: 140 mM NaCl, 5 mM KCl, 2 mM $CaCl_2$, 1 mM $MgCl_2$, 5 mM glucose, and 20 mM Hepes/Tris (pH 7.0). Cells were then placed in a flow chamber connected to a perfusion system and superfused (0.6 ml/min) with HBS at 35 °C. We measured fluorescence at 510–530 nm with alternating excitations at 440 and 490 nm through a 505-nm dichroic reflector. Images were collected every 10–20 s using a cooled CCD camera (ORCA-ER, Hamamatsu photonics K.K., Japan) mounted on an inverted microscope (IX 71, Olympus) with a ×20 objective (UApo/340, Olympus), and processed with AQUACOSMOS software (Hamamatsu Photonics). Change in pH_i was monitored by switching perfusions from normal medium to HBS containing various reagents. The resting pH_i was calibrated as previously reported, using a high $[K^+]$ solution containing: 140 mM KCl, 2 mM $CaCl_2$, 1 mM $MgCl_2$, and 0.005 mM nigericin, and adjusted to various pH values ranging from 7.0 to 7.5. The change in pH_i was also measured by the [^{14}C]benzoic acid-equilibration method (22, 28). In this experiment, serum-depleted cells were preincubated for 30 min in bicarbonate-free HEPES-buffered DMEM (pH 7.0), and then incubated in the same medium containing [^{14}C]benzoic acid (1 μCi/ml) and various agents for 15 min at 37 °C. In some experiments, cells were preincubated in HEPES-buffered DMEM containing wortmannin (10 μM) or PKC inhibitors (1 μM) and then switched to radioisotope medium containing PMA or phenylephrine and each inhibitor. After washing four times with ice-cold phosphate-buffered saline, the cellular uptake of ^{14}C-radioactivity was measured. The change in pH_i was calculated according to the following equation: $\Delta pH_i = \log_{10}(^{14}C_{stim}/^{14}C_{ref})$, where $^{14}C_{stim}$ and $^{14}C_{ref}$ are the intracellular ^{14}C-radioactivity in the presence or absence of extracellular stimuli, respectively.

Measurement of $^{22}Na^+$ Uptake—$^{22}Na^+$ uptake activity was measured by the K^+/nigericin pH_i clamp method as described previously (29). In brief, serum-depleted cells in 24-well plates were preincubated for 30 min at 37 °C in a Na^+-free choline chloride/KCl medium containing: 20 mM HEPES/Tris (pH 7.4), 1.2–140 mM KCl (adjusted to total 140 mM by choline chloride), 2 mM $CaCl_2$, 1 mM $MgCl_2$, 5 mM glucose, and 0.005 mM nigericin. $^{22}Na^+$ uptake was initiated by adding the same choline chloride/KCl solution containing ^{22}NaCl (37 kBq/ml; final concentration, 1 mM), 1 mM ouabain, and 0.1 mM bumetanide. In some wells, the uptake solution contained 0.1 mM EIPA. One min later, cells were rapidly washed four times with ice-cold phosphate-buffered saline to terminate $^{22}Na^+$ uptake. pH_i was calculated from $[K^+]_i/[K^+]_o = [H^+]_i/[H^+]_o$ by assuming an intracellular $[K^+]$ of 120 mM. EIPA-inhibitable $^{22}Na^+$ uptake was fitted by nonlinear least squares analysis to a Hill equation using GraphPad Prism software (GraphPad Software Inc.), as shown in Equation 1,

$$\text{EIPA-sensitive } ^{22}Na^+ \text{ uptake} = V_{max}/[1 + 10^{(pK - pH_i)n}] \quad \text{(Eq. 1)}$$

where V_{max} is the maximal uptake activity at very low pH_i, K is the dissociation constant for H^+, and n is the Hill coefficient. Data were plotted against pH_i after normalization to the V_{max} value. In some experiments, calphostin C (1 μM) or staurosporin (1 μM) was included throughout the preincubation and $^{22}Na^+$ uptake periods. The data were normalized based on the protein concentration, which was measured using a bicinchoninic assay system (Pierce), using bovine serum albumin as a standard.

Measurement of PE Binding to Peptides—Binding of the fluorescent PE, SAPD, to peptides was quantified essentially as

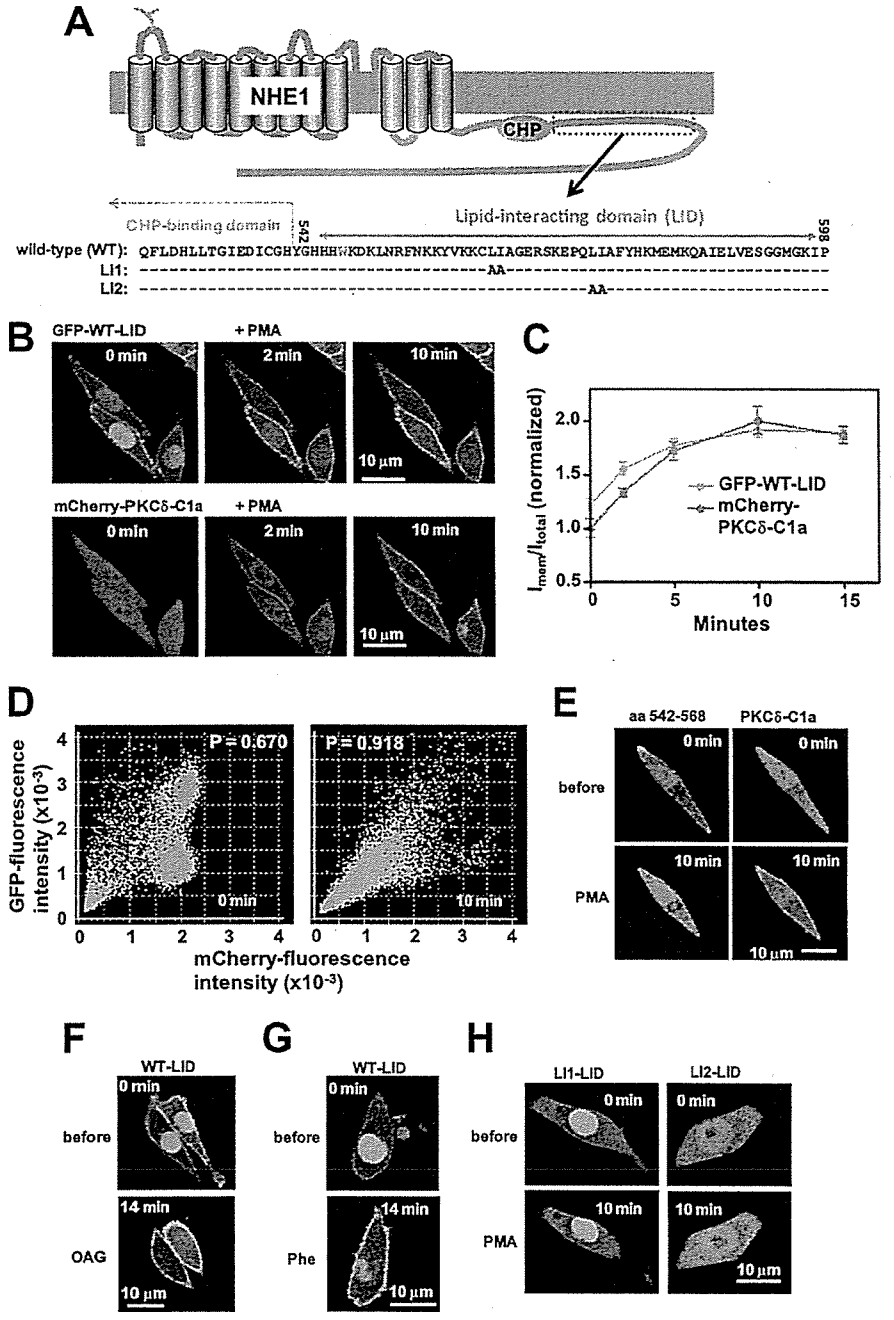

FIGURE 1. **Plasma membrane translocation of LID.** *A*, topology model of NHE1 and amino acid sequence of LID. Positions of two mutant constructs (LI1 and LI2) are represented. Leu-562 and Ile-563 in LI1 and Leu-573 and Ile-574 in LI2 were replaced with two alanine residues. *B*, PMA (1 μM) facilitates translocation of GFP-labeled LID (GFP-WT-LID) to the plasma membrane, in a similar time course as mCherry-labeled PKCδ-C1a domain. Note that fluorescence signals detected in the nucleus decreased and accumulated in the plasma membrane. *C*, time courses for the accumulation of two fluorescent probes in the plasma membrane within the same cells. Means ± S.E. (n = 7). *D*, colocalization efficiency was analyzed for a cell in *B* before and 10 min after PMA addition. High Pierson's coefficient (0.918) was observed with PMA. *E*, PMA does not promote the plasma membrane translocation of the 27 N-terminal residues of LID. OAG (100 μM) (*F*) and phenylephrine (Phe) (1 μM) (*G*) facilitate plasma membrane translocation of LID. In *G*, α1AR was stably expressed. *H*, PMA does not promote plasma membrane translocation of two LID mutants.

described previously (30) by measuring the fluorescence resonance energy transfer (FRET) from tryptophans to the 2-(*N*-methylamino)benzoyl fluorophore attached at the 12-position of the phorbol moiety. The fluorescence intensities, obtained upon excitation of the tryptophan fluorophore at 280 nm, were determined using a spectrofluorimeter (Hitachi, FL4500) at 340 and 440 nm, corresponding to the emission maxima of tryptophan and SAPD, respectively. Peptides used in the experiments contain one tryptophan residue (Trp-546 of NHE1 for GP57 and GC20, Trp-663 of NHE1 for IL54). The solution (0.5 ml) consisted of 100 mM Tris/HCl, pH 7.4, 1 mM dithiothreitol, and 10 μM each peptide. In one experiment, liposomes (0.17 mg) consisting of 89% PC, 5% PS, 5% PA, and 1% PIP_2 (weight %) was added to the cuvette. In some experiments, PMA, 4α-PMA, and OAG were added at the indicated concentrations. SAPD was titrated from stock solutions of the required concentration prepared from a Me_2SO solution. To isolate the fluorescence signal resulting from FRET, the observed fluorescence intensities at each SAPD concentration were corrected for volume changes incurred during the titration procedure and normalized for the contribution from the direct excitation of the SAPD fluorophore according to Equation 2,

$$\text{FRET} = (F_{i,+P} - F_{i,-P}) - (F_{0,+P} - F_{0,-P}) \quad \text{(Eq. 2)}$$

where $F_{i,+P}$ and $F_{i,-P}$ are the fluorescence intensities measured after each SAPD addition in the presence and absence of peptides, respectively, and $F_{0,+P}$ and $F_{0,-P}$ are the fluorescence intensities measured in the absence of SAPD in the presence and absence of peptides, respectively. The data were fitted by nonlinear least squares analysis to a Hill equation, as shown in Equation 3,

$$\text{FRET} = (F_{max} - F_{min})/[(K_{d/cSAPD})^n + 1] \quad \text{(Eq. 3)}$$

where F_{max} and F_{min} are the maximum and minimum corrected FRET signals, K_d is the binding constant for SAPD, *cSAPD* is the concentration of SAPD, and n is the Hill coefficient. In the presence of

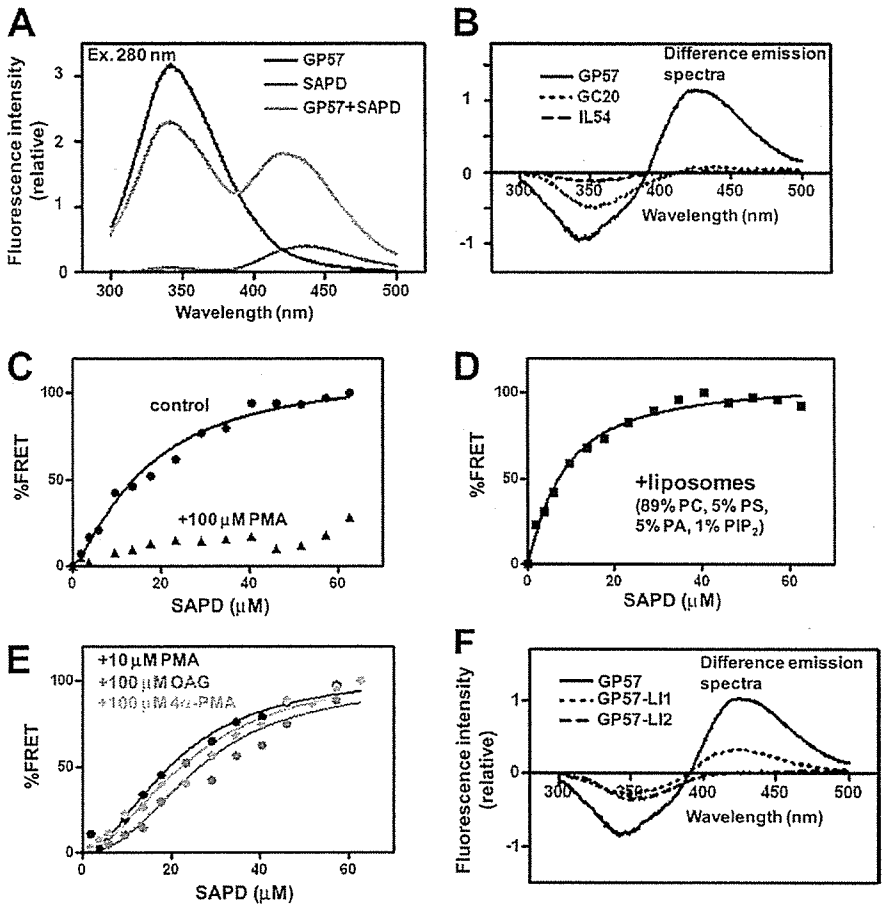

FIGURE 2. **PEs directly interact with LID *in vitro*.** *A*, emission spectra at 280-nm excitation. FRET signals were observed between a tryptophan residue of peptide GP57 spanning LID (10 μM) and the fluorescent PE analogue SAPD (20 μM). *B*, difference emission spectra. In peptides GC20 and IL54, FRET signals (increment in fluorescence intensity at 440 nm) were not observed. *C*, FRET signals were considerably reduced in the presence of high concentrations of PMA (100 μM). *D*, liposomes increased SAPD affinity (see Table 1). *E*, PMA (10 μM), OAG (100 μM), and 4α-PMA (100 μM) decrease the apparent affinity of GP57 for SAPD, suggesting that they competitively interact with GP57. *F*, two mutations, particularly LI2, markedly reduced FRET signals.

TABLE 1

Summary of FRET data obtained with GP57

Concentration dependence of SAPD on FRET signals was measured in the presence or absence of additional chemicals. The apparent dissociation constant $K_{d,app}$ for SAPD was obtained by curve-fitting to a Hill equation as described under "Experimental Procedures." Using the $K_{d,app}$ value for SAPD in the absence of other chemicals, intrinsic $K_{d,C}$ for the added competitors was calculated by assuming competition. Data are expressed as the best-fit values ± S.E.

Added chemicals	$K_{d,app}$ for SAPD	Calculated $K_{d,C}$ for added competitors	Hill coefficient
	μM	μM	
None	16.5 ± 3.1		1.36 ± 0.25
PMA (10 μM)	24.0 ± 3.8	22.3	1.90 ± 0.42
OAG (100 μM)	26.0 ± 6.4	174.7	2.30 ± 0.81
4α-PMA (100 μM)	24.3 ± 5.1	213.4	1.83 ± 0.49
Liposomes	8.07 ± 1.1		1.16 ± 0.16

competitive chemicals, the data were fitted by the competitive binding equation, as shown by Equations 4 and 5,

$$FRET = (F_{max} - F_{min})/[(K_{d,app/cSAPD})^n + 1] \quad \text{(Eq. 4)}$$

$$K_{d,app} = K_{d,SAPD}(1 + C/K_{d,C}) \quad \text{(Eq. 5)}$$

where $K_{d,app}$ is the apparent binding constant for SAPD in presence of competitors, C is the concentration of competitors (C) included in the cuvette, and $K_{d,C}$ is the binding constant for C. After obtaining $K_{d,app}$ by curve fitting, $K_{d,C}$ was calculated using the $K_{d,SAPD}$ value for SAPD.

Liposome Binding Assay of Peptides—For liposome preparation, a lipid mixture was made in chloroform and dried under nitrogen gas. Dried lipid mixture was agitated vigorously by vortexing in a buffer containing 100 mM Tris/HCl, pH 7.5, 1 mM dithiothreitol and sonicated for 1 min on ice in a bath-type sonicator. The resultant liposomes (0.2 mg) were mixed with peptides (140 μM) in the above Tris buffer (total volume 25 μl), incubated 10 min at room temperature, and centrifuged for 1 h at 100,000 × *g*. An aliquot of supernatant was subjected to PAGE with a 4–12% gradient gel (Invitrogen), together with a peptide mixture without centrifugation as a reference (total). Peptide bands were visualized by Coomassie Brilliant Blue staining and analyzed using Image-Pro Plus software (Media Cybernetics Inc.). The relative amount of peptides bound to liposomes was calculated by subtracting the amount of peptides remaining in the supernatant from the initial input as follows in Equation 6,

$$\text{Lipid binding (\%)} = (P_t - P_s) \times 100/P_t \quad \text{(Eq. 6)}$$

where P_t is the amount of total peptide without lipids, while P_s is the amount of peptide in the supernatant after centrifugation.

Reagents—In this study, the following N-terminally biotinylated peptides corresponding to the cytoplasmic regions of NHE1 were synthesized with >85% purity by GL Biochem Ltd.: GP57, GHHHWKDKLNRFNKKYVKKCLIAGERSKEPQLIAFYHKMEMKQAIELVESGGMGKIP; GP57-LI1, GHHHWKDKLNRFNKKYVKKCAAAGERSKEPQLIAFYHKMEMKQAIELVESGGMGKIP; GP57-LI2, GHHHWKDKLNRFNKKYVKKCLIAGERSKEPQAAAFYHKMEMKQAIELVESGGMGKIP; GC20, GHHHWKDKLNRFNKKYVKKC; and IL54, IRKILRNNLQKTRQRLRSYNRHTLVADPYEEAWNQMLLRRQKARQLEQKINNYL.

SAPD was purchased from Calbiochem, PMA and 4α-PMA from Sigma, OAG and other membrane lipids from Avanti Polar Lipids (Alabaster, AL), and ^{22}NaCl and [^{14}C]benzoic acid from PerkinElmer Life Science Inc. All other chemicals were of the highest purity available.

RESULTS

PEs Facilitate the Translocation of LID to the Plasma Membrane—We first determined whether PEs modulate the interaction of LID with the plasma membrane. Green fluorescent protein (GFP)-labeled LID expressed in fibroblasts (exchanger-deficient PS120 cells) targeted the plasma membrane and was located within cells (Fig. 1*B*). Interestingly, phorbol-12-myristate-13-acetate (PMA) greatly facilitated the translocation of LID to the plasma membrane (Fig. 1*B* and supplemental movie S1), which is also a characteristic of the PKC regulatory domain C1, where direct PE binding facilitates anionic membrane interactions (31). We also observed that GFP-LID and mCherry-PKCδ-C1a translocated to the plasma membrane in response to PMA over a similar time course within the same cells (Fig. 1, *B* and *C*) and finally colocalized in the plasma membrane (Fig. 1*D*). Such translocation did not occur in the case of the GFP-labeled 27 N-terminal residues (amino acids 542–568) of LID (Fig. 1*E* and supplemental movie S2), indicating that the C-terminal region is required for this phenomenon. Furthermore, LID accumulated in the plasma membrane in response to a membrane-permeable DAG analogue, 1-oleoyl-2-acetyl-*sn*-glycerol (OAG) (Fig. 1*F* and supplemental movie S3), thrombin (supplemental Fig. S1), and α1-adrenergic receptor (α1AR) agonist phenylephrine only when its receptor was expressed (Fig. 1*G* and supplemental movie S4). These results strongly suggest that PEs and the endogenous second-messenger DAG directly bind LID, thereby increasing the latter's affinity to plasma membranes.

PEs Directly Bind LID in Vitro—To study the LID-PE interaction *in vitro*, we determined whether fluorescence resonance energy transfer (FRET) occurs between the two. We synthesized a 57-residue peptide (GP57, Gly-542—Pro-598) spanning LID and examined whether FRET occurs between the tryptophan residue (Trp-546) of GP57 and the fluorescent PMA analogue, sapintoxin D (SAPD), as described previously (32). Inclusion of GP57 markedly increased the fluorescence intensity of SAPD with a slight blue-shift at the maximal emission wavelength of SAPD (440 nm), indicating clear FRET from tryptophan to the 2-(*N*-methylamino)benzoyl fluorophore of SAPD (Fig. 2*A*). FRET was not observed in the 20 N-terminal residues (GC20, Gly-542—Cys-561) of LID or in a control peptide (IL54, Ile-631—Leu-684 of NHE1) (Fig. 2*B*), and was greatly reduced by competition with 100 μM non-fluorescent PMA (Fig. 2*C*), suggesting that LID, particularly its 37 C-terminal residues, directly interacts with PEs. The affinity of GP57 for SAPD increased in the presence of liposomes (K_d, from 16.5 to 8.1 μM) (Fig. 2*D* and Table 1), suggesting that PEs may bind LID with higher affinity in membranes. Competition experiments revealed that OAG and even the inactive PE analogue 4α-PMA interact with LID, though with lower affinity (Fig. 2*E* and Table 1).

Besides these lipophilic compounds, we also examined the interaction of LID with membrane lipids by testing for direct binding. GP57 was incubated with liposomes consisting of various membrane lipids and then centrifuged; the unbound supernatant was analyzed using gel electrophoresis followed by Coomassie Brilliant Blue staining. We found that LID interacts with multiple membrane lipids, particularly, acidic phospholipids such as PIP_2, phosphatidylserine (PS), and phosphatidic acid (PA) (Fig. 3, *A* and *B*). GP57 exhibited the following order of binding strength: PIP_2 > PS, phosphatidylinositol (PI), PA > phosphatidylglycerol (PG) > phosphatidylcholine (PC) (supplemental Fig. S2).

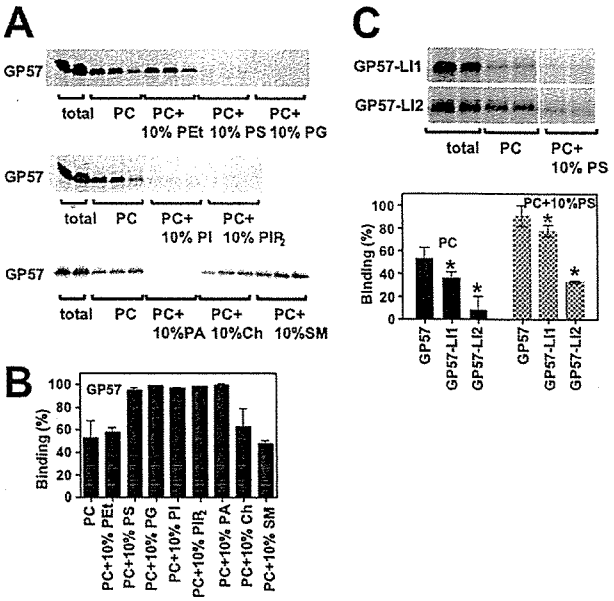

FIGURE 3. **Multiple phospholipids can interact with LID.** *A*, CBB-stained patterns of peptide GP57 spanning LID. Liposomes containing various lipids (weight %, adjusted to 100% with PC) were mixed with GP57 and centrifuged. Peptides before centrifugation (total) and an aliquot of each supernatant were subjected to PAGE. It was difficult to obtain the reliable data for interaction of DAG with peptides using this method because DAG inhibited the stable liposome formation. *B*, relative amount of GP57 bound to liposomes was calculated as described under "Experimental Procedures." GP57 preferentially binds to acidic phospholipids such as PS, PG, PI, PIP_2, and PA. Approximately 50% of peptides also bind to liposomes consisting of only PC under these conditions, suggesting that GP57 is capable of binding various membrane lipids. *C*, binding of peptides containing replaced residues to PC or PC + PS liposomes. CBB-stained patterns of peptides GP57-LI1 and GP57-LI2 from total input and the supernatant. Summarized data are represented in the *lower panel*. One amino acid substitution (GP57-LI2) markedly inhibited lipid binding, whereas another substitution (GP57-LI1) had a small inhibitory effect. Means ± S.D. (n = 3–4). *, $p < 0.05$ *versus* GP57.

Mutations in LID Abolish PE- and Hormone-induced Activation of NHE1—To study the role of LID in the regulation of NHE1 activity, we generated alanine-scanning mutations. Six mutations of conserved residues (Fig. 1*A* and supplemental Fig. S3) abrogated PE-promoted translocation of LID to the plasma membrane (Fig. 1*H* and supplemental Fig. S3 and movie S5), suggesting that the whole region of LID is important for membrane interaction. Mutations (particularly LI2, in which Leu-573 and Ile-574 were replaced with two alanine residues) also markedly inhibited the interaction of LID with PEs and phospholipids (Figs. 2*F* and 3*C*). Rapid and persistent cytoplasmic alkalinization, a consequence of increased cytosolic H^+ affinity, has been used as a reliable indicator of NHE1 activation (3, 28). PMA, OAG, and SAPD induced such alkalinization in cells expressing wild-type full-length NHE1 (Fig. 4, *A–C*). PE-induced alkalinization occurred at relatively low concentrations (>0.03 μM SAPD) (Fig. 4*C*). Phenylephrine also induced alkalinization only in cells co-expressing α1ARs

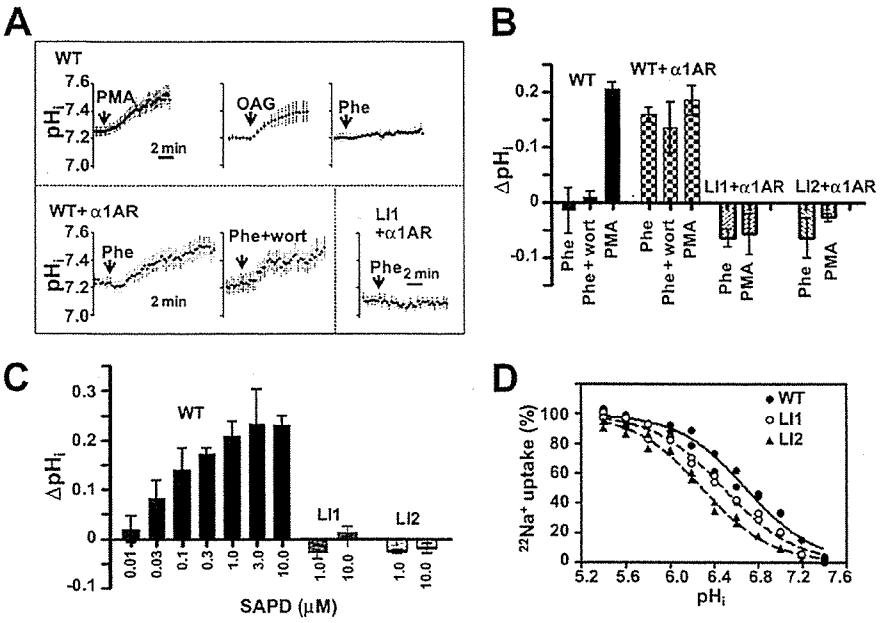

FIGURE 4. **Effect of LID mutation on NHE1 activity and regulation.** *A*, change in pH_i was measured using the pH_i indicator BCECF-AM. PS120 cells were stably transfected with WT NHE1 (*upper*), WT + α1AR (*lower left*), or LI1 + α1AR (*lower right*). Cells were stimulated with PMA (1 μM), OAG (100 μM), or phenylephrine (*Phe*) (1 μM). In one experiment, cells were preincubated for 15 min with wortmannin (wort) (10 μM) and then stimulated with phenylephrine in the presence of wortmannin. Means ± S.E. (n > 20 cells). *B*, change in pH_i 15 min after stimulation was measured using the [^{14}C]benzoic acid equilibration method. Means ± S.D. (n = 3). *C*, SAPD-induced cytoplasmic alkalinization measured in cells expressing WT or mutant NHE1 by using the ^{14}C-benzoic acid equilibration method. This alkalinization was abolished by mutations in LID. Means ± S.D. (n = 3). *D*, LID mutations induced an acidic shift of pH_i dependence (decreased cytosolic H^+ affinity).

TABLE 2

Summary for $^{22}Na^+$ uptake activity (Fig. 4*D*) measured in cells expressing the NHE1 variants

The EIPA-inhibitable $^{22}Na^+$ uptake was fitted by nonlinear least squares analysis to a Hill equation. V_{max} is the $^{22}Na^+$ uptake activity at a very low pH_i and normalized by the amount of total protein expression. Mutation LI2 reduced both V_{max} and pK values, while LI1 reduced the pK value. Data are the best-fitted values ± S.E.

Mutant	V_{max}	Expression-normalized V_{max}	pK for pH_i	Hill coefficient
	nmol/mg/min	%		
WT	30.0 ± 1.0	100 ± 3.4	6.69 ± 0.03	1.41 ± 0.12
LI1	12.0 ± 0.5	88.2 ± 3.8	6.49 ± 0.03	1.38 ± 0.10
LI2	10.9 ± 0.4	36.9 ± 1.4	6.30 ± 0.06	1.33 ± 0.17

(Fig. 4, *A* and *B*). Interestingly, such alkalinization was dramatically inhibited by LI1, LI2 (Fig. 4, *A–C*), and other mutations (supplemental Fig. S3) incorporated into the entire NHE1 molecule, suggesting that the PE/DAG-promoted interaction of LID with the plasma membrane may be essential for NHE1 activation.

Moreover, these mutations decreased cytosolic H^+ affinity for NHE1 as shown by the acidic shift of pH_i dependence (Fig. 4*D* and Table 2) as well as the maximal activity at acidic pH_i (supplemental Fig. S4), thus reducing the basal exchange activity particularly in neutral pH_i range. These observations suggest that LID-membrane interaction is also required for optimal NHE1 function in the resting state. PIP_2 would be the most important lipid for this function (20, 21). However, under rapid PIP_2 breakdown after receptor stimulation, most LID probes remain in the plasma membrane (supplemental Fig. S5 and movie S6), and exchange activity is uninhibited (no decrease in pH_i) even when PIP_2 re-synthesis is blocked by wortmannin (Fig. 4, *A* and *B*, supplemental Fig. S6 and movie S7), suggesting that basal activity is preserved even under conditions of reduced PIP_2, possibly because of interactions between LID and predominant acidic lipids within membranes. Thus, the broad lipid specificity of LID may facilitate rapid NHE1 activation after receptor stimulation.

PKC Inhibitors, except Staurosporin, Are Ineffective in Blocking NHE1 Activation—We next examined the possible involvement of PKC in NHE1 regulation by using PKC inhibitors. PMA induced the translocation of myristoyl alanine-rich protein kinase C substrate (MARCKS) from the plasma membrane to the cytoplasm (Fig. 5*A*) in response to PKC-mediated phosphorylation (33), and five known PKC inhibitors almost completely inhibited this PMA-induced MARCKS translocation, indicating that the test compounds could inhibit PKC. However, under similar conditions, bisindolylmaleimide I, calphostin C, Go-6976, and Ro-32–0432 had only a marginal inhibitory effect on alkalinization, but staurosporin completely inhibited alkalinization (Fig. 5*B*). These results suggest that PKC is not majorly involved in PE- or hormone-induced NHE1 activation. We next determined why only staurosporin completely inhibited NHE1 activation. Similar to LID mutations and unlike calphostin C, staurosporin by itself decreased cytosolic H^+ affinity (Fig. 5*C* and Table 3), suggesting that staurosporin directly acts on the NHE1 molecule. Furthermore, staurosporin completely blocked PMA-induced translocation of LID to the plasma membrane, possibly through competition with PMA at LID (Fig. 6, *A* and *D* and supplemental movie S8). Similar inhibition by staurosporin was observed in the case of OAG- and phenylephrine-induced translocation of LID (data not shown). In contrast, calphostin C, which does not inhibit NHE1, had no effect on LID, although it completely inhibited PMA-mediated PKCδ-C1a translocation (Fig. 6, *B* and *D* and supplemental movie S9). The opposing translocation effects of staurosporin and calphostin C on PKCδ-C1a are attributable to their different competition sites; staurosporin binds to the ATP-binding site of PKC, whereas calphostin C binds to the PKCδ-C1a domain. Staurosporin itself at least partly reduced membrane localization of LID (supplemental Fig. S7), suggesting that it can inhibit lipid binding of LID. These results indicate that both staurosporin-induced reduction in H^+ affinity and abolishment of NHE1 activation occur via interactions between staurosporin and LID, not via inhibition of PKC. Like staurosporin but with a weaker effect, the PE analogue 4α-PMA inhibited both

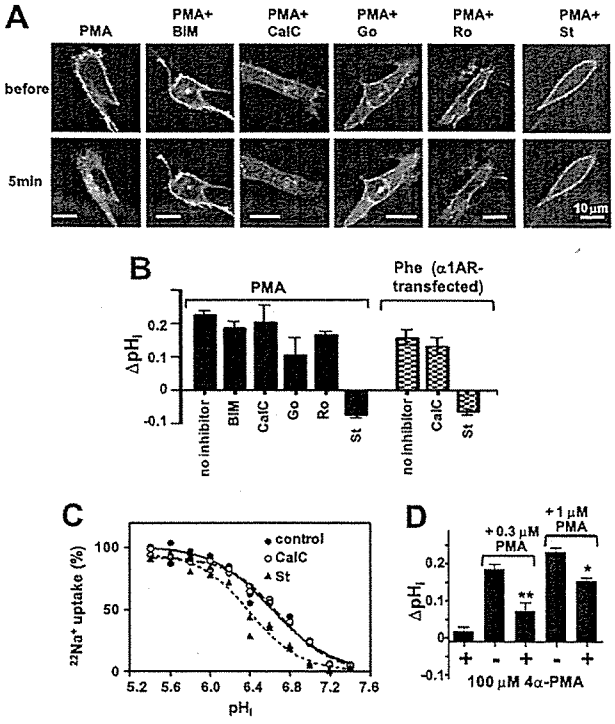

FIGURE 5. **Effect of PKC inhibitors and 4α-PMA on PE-induced NHE1 activation.** *A*, effect of PKC inhibitors on the translocation of myristoylated alanine-rich C kinase substrate (MARCKS) from the plasma membrane to the cytoplasm. Cells transiently expressing the MARCKS-GFP protein were preincubated with PKC inhibitors (1 μM each) for 15 min, and then PMA (1 μM) together with these inhibitors were added at time 0. These PKC inhibitors almost completely abrogated the translocation of MARCKS from the plasma membrane to the cytoplasm, confirming that they inhibited PKC. BIM, bisindolylmaleimide I; CalC, calphostin C; Go, Go-6976; Ro, Ro-32-0432; and St, staurosporin, Scale, 10 μm. *B*, under conditions similar to those in the experiment of MARCKS translocation, the effect of PKC inhibitors on PMA- or phenylephrine (Phe)-induced NHE1 activation was examined. Except for staurosporin (St), all other PKC inhibitors tested had only a marginal inhibitory effect on NHE1 activation. *C*, staurosporin, but not calphostin C, decreased cytosolic H^+ affinity in WT-NHE1-expressing cells. *D*, 4α-PMA competitively inhibited PMA-induced cytoplasmic alkalinization. *, $p < 0.05$; **, $p < 0.01$.

TABLE 3

Summary for $^{22}Na^+$ uptake activity (Fig. 5C) measured in cells expressing wild-type NHE1 in the presence of calphostin C or staurosporin

The EIPA-inhibitable $^{22}Na^+$ uptake was fitted by nonlinear least squares analysis to a Hill equation. V_{max} is the $^{22}Na^+$ uptake activity at a very low pH_i and normalized by V_{max} in the absence of inhibitors. Although calphostin C and staurosporin did not affect V_{max}, St significantly reduced the pK value. Data are the best-fitted values ± S.E.

Treatment	V_{max}	Normalized V_{max}	pK for pH_i	Hill coefficient
	nmol/mg/min	%		
None	30.1 ± 0.4	100 ± 1.3	6.62 ± 0.03	1.46 ± 0.13
Calphostin C	29.8 ± 1.1	99.3 ± 3.7	6.70 ± 0.02	1.70 ± 0.10
Staurosporin	29.8 ± 2.9	99.3 ± 9.7	6.40 ± 0.04	1.70 ± 0.21

PMA-induced NHE1 activation and LID recruitment to the plasma membrane, apparently in competition with PMA (Figs. 5*D* and 6, *C* and *D* and supplemental Fig. S7 and movie S10). Partial inhibition of PMA-induced translocation was also observed for Go-6976 structurally related compound of staurosporin (supplemental Fig. S7), which appears to slightly inhibit NHE1 activation (Fig. 5*B*).

DISCUSSION

We analyzed the biochemical properties of LID, a critical regulatory region of NHE1, to gain insights into the molecular mechanism underlying the hormonal activation of NHE1. We found that (i) PEs directly interact with the LID of NHE1 *in vitro*, (ii) GFP-LID translocates to the plasma membrane in response to PEs, OAG, and α1AR agonists, suggesting that the direct interaction of PEs/DAG with LID increases LID affinity to the plasma membrane. Furthermore, mutations affecting LID (particularly LI2) markedly inhibit the above interactions and abolish PE- or α1AR agonist-induced NHE1 activation, supporting the view that NHE1 is activated through the direct interaction of LID with PEs/DAG, followed by stronger interaction with the plasma membrane (see Fig. 6*E* for the schematic model). Compared with LI2, LI1 mutation had a weak inhibitory effect on lipid binding (Fig. 3*C*), but resulted in complete abrogation of NHE1 activation (Fig. 4, *B* and *C*). NHE1 activation may occur via multiple sequential steps including PEs/DAG binding, conformational change of LID and subsequent increased association of LID with membranes. LI1 mutation partially inhibited PE binding and completely inhibited membrane translocation of LID. Thus complete abrogation of NHE1 activation would be due to an overall consequence resulting from inhibitions of multiple events by LI1 mutation.

Experimental evidence indicated that the C terminus (~40 residues) of LID is required for its interaction with PEs. Further, we observed that the N-terminal peptide of LID (GC20) preferentially interacted with acidic lipids (data not shown), supporting a previous report that positive charge clusters in the LID N terminus may be important for electrostatic interactions (20). However, the interaction of LID with the plasma membrane was abrogated by mutations in the C terminus (LI2 etc.) as well as those in the N terminus (mutations of basic residues, etc., see supplemental Fig. S3), indicating that the entire region encoding the LID is important for the association of this domain with cell membranes. Further experiments will be required for elucidating whether LID is separated into several functional subdomains and how PEs/DAG increase the interaction with membrane lipids via possible structural coupling between these subdomains.

We identified several residues, for example, Leu-573 and Ile-574 that were important for the binding of PEs to LID. Unlike LID, the C1 domains of PKC and other "nonkinase" proteins such as chimerins and Munc13 coordinate two Zn^{2+} ions with conserved cysteine and histidine residues (34, 35). Although the amino acid sequences of the LID and PKC-C1 domain exhibit partial homology, LID does not possess residues coordinating Zn^{2+} ions (supplementary Fig. S8). Thus, LID is a previously unrecognized motif of PE binding. Because of the marked differences between the LID sequence and the sequences of known PE targets, the existence of this domain may have been overlooked in many membrane proteins, despite its functional importance. PE binding to LID occurs at micromolar concentrations of PEs, at least, *in vitro*. Thus, the affinity of PEs to LID may not be sufficiently high for their interaction with NHE1 in cells. However, we observed that despite the apparent low affinity, submicromolar concentrations of PEs were capable

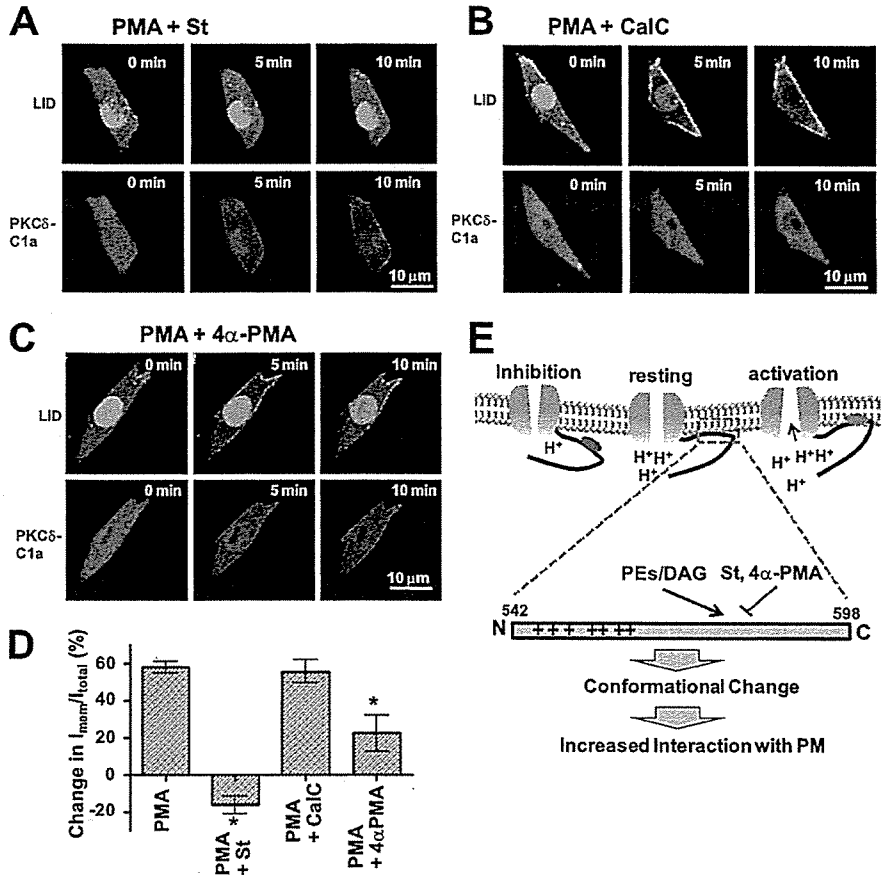

FIGURE 6. **Differential effects of lipophilic compounds on plasma membrane translocation of LID.** *A*, staurosporin (*St*) inhibits PMA-induced LID (*upper*), but not PMA-induced PKCδ-C1a (*lower*), plasma membrane translocation. *B*, in contrast, calphostin C (CalC) does not inhibit PMA-induced LID (*upper*) translocation, but does inhibit PKCδ-C1a (*lower*) plasma membrane translocation. *C*, similar to staurosporin, 4α-PMA partly inhibits LID, but not PKCδ-C1a, plasma membrane translocation. *D*, relative change (%) in the fluorescence intensity of GFP-LID localized in the plasma membrane before and after (10 min) the addition of PMA and/or other reagents. Means ± S.E. ($n = 5$–7). *, $p < 0.05$ *versus* PMA alone. *E*, schematic models for NHE1 regulation (*upper*) with LID (*lower*). In the resting state, physiological NHE1 activity is preserved by interaction of LID with membrane phospholipids. Upon PE or receptor stimulation, PE/DAG binds to LID (probably its C-terminal portion), induces a conformational change to increase its affinity for membrane lipids, and thereby increases H^+ affinity, leading to NHE1 activation. Mutations or interaction with some lipophilic compounds such as staurosporin reduce the affinity of LID to lipids, and thus inhibit NHE1 by decreasing H^+ affinity.

of activating NHE1: alkalinization was detectable at 0.03 μM SAPD (Fig. 4*C*). Furthermore, (i) incubation of GP57 with membrane lipids increased the affinity of PEs to LID (Table 1), and (ii) SAPD fluorescence in the medium was observed to rapidly and strongly accumulate within the cells (data not shown). The latter observation suggests that the concentration of PEs in the cells is much higher than that in the medium, and that the low concentration of added PEs is sufficient for PE interaction with the LID of NHE1 within the cells, despite the low affinity of PEs.

Stimulation of G protein-coupled receptors induces hydrolysis of PIP_2 by phospholipase C, which in turn produces two second messengers: DAG, which is a potent PKC activator, and inositol 1,4,5-triphosphate, which releases the calcium stored in the endoplasmic reticulum (36). We previously reported that the released calcium activates NHE1 through the direct binding of calcium/calmodulin to the autoinhibitory cytoplasmic domain of NHE1 in the early phase (~1 min) after receptor stimulation (37, 38). In addition to such regulation, our present findings indicate that DAG directly contributes to the prolonged activation of NHE1. It should be noted that NHE1 activity is not inhibited even under the conditions of reduced PIP_2 levels after receptor stimulation. This finding can be best explained by the broad lipid specificity of LID and the predominant presence of acidic phospholipids like phosphatidylserine in the inner leaflet of the plasma membrane (39). By interacting with different lipids, LID would be able to preserve basal exchange activity and render NHE1 further activatable despite PIP_2 breakdown. However, this hypothesis appears to contradict previous findings that NHE1 activity is robustly inhibited under conditions of PIP_2 depletion either by cellular ATP depletion (20) or overexpression of lipid phosphatase from *salmonera* (40). We cannot rule out the possibility that receptor stimulation produces different effects on PIP_2 hydrolysis from those produced by ATP depletion or treatment with exogenous phosphatase: for instance, some localized PIP_2 bound to NHE1 may not be completely hydrolyzed upon receptor stimulation and thus the NHE1 activity may be preserved, whereas localized PIP_2 may be dephosphorylated by other treatments, leading to robust inhibition of NHE1 activity.

Although many studies have used PKC inhibitors to validate the involvement of PKC in NHE1 regulation (41–44), the effectiveness of these inhibitors are variable. Therefore, in this study, we assessed NHE1 regulation by using only those inhibitors that completely inhibited MARCKS translocation under similar conditions. Our data suggest that PKC is not largely involved in either PE- or hormone-induced NHE1 activation; however, we cannot rule out the involvement of PKC isoforms that do not phosphorylate MARCKS. In this study, we identified staurosporin as a new type of NHE1 inhibitor. Interestingly, staurosporin inhibited NHE1 activity only by reducing its affinity to H^+ without altering the maximal exchange activity at acidic pH_i (Table 3), in sharp contrast to amiloride derivatives, which completely inhibit NHE1 activity. Importantly, the NHE1 inhibition by staurosporin was mediated through LID, which is distant from the putative amiloride-binding sites, the transmembrane-spanning segments (45, 46). This observation is

consistent with our previous findings that the juxtamembrane cytoplasmic domain including LID is crucial for pH_i sensing (22, 47).

LID appears to bind various lipids or lipophilic compounds with broad specificity and to serve as an essential module to differentially regulate NHE1 activity, depending on the interacting molecules. For example, 4α-PMA was a weak inhibitor of PMA-induced NHE1 activation (Fig. 5*D*). Surprisingly, okadaic acid, a phosphatase inhibitor and known potent NHE1 activator (48), promoted LID translocation to the plasma membrane,[3] probably via direct interaction between the two. This broad specificity of LID is advantageous for NHE1, which is regulated by a variety of signals, and explains the diverse regulatory mechanisms of different NHE isoforms. For example, NHE1 and NHE2 are activated by PEs (49), whereas NHE3 and NHE5 are inhibited by PEs (49, 50). Despite the relatively high homology of LIDs among NHE isoforms, subtle differences exist in the primary structure of these isoforms (supplemental Fig. S8). These differences may lead to differences between the regulatory effects of PE binding on NHE1/2 and NHE3/5. This testable hypothesis will be analyzed in the future.

Many studies have reported that NHE1 is regulated by phosphorylation-dependent pathways (6, 51–54). However, the role of phosphorylation of the NHE1 molecule itself is rather controversial; in our hands, no significant inhibition of PMA- or hormone-induced NHE1 activation was detected upon Ala-substitution mutations of several Ser residues including the ones reported to be phosphorylated (data not shown, but see Ref. 23). In conclusion, we propose a novel phosphorylation-independent mechanism for transporter regulation via "non-C1"-type PE receptors, which may be distributed in many membrane proteins. Our findings may help develop new LID-based therapies for cancer and heart failure since drugs targeting LIDs are expected to selectively block increments in NHE1 activity in response to various stimuli.

Acknowledgment—We thank Prof. Munekazu Shigekawa (Senri Kinran University) for the critical reading of this manuscript.

REFERENCES

1. Nishizuka, Y. (1992) *Science* **258,** 607–614
2. Griner, E. M., and Kazanietz, M. G. (2007) *Nat. Rev. Cancer* **7,** 281–294
3. Moolenaar, W. H., Tertoolen, L. G., and de Laat, S. W. (1984) *Nature* **312,** 371–374
4. Grinstein, S., Cohen, S., Goetz, J. D., and Rothstein, A. (1985) *J. Cell Biol.* **101,** 269–276
5. Besterman, J. M., and Cuatrecasas, P. (1984) *J. Cell Biol.* **99,** 340–343
6. Wakabayashi, S., Shigekawa, M., and Pouyssegur, J. (1997) *Physiol. Rev.* **77,** 51–74
7. Pedersen, S. F., and Cala, P. M. (2004) *J. Exp. Zoolog. A. Comp. Exp. Biol.* **301,** 569–578
8. Zachos, N. C., Tse, M., and Donowitz, M. (2005) *Annu. Rev. Physiol.* **67,** 411–443
9. Fliegel, L. (2005) *Int. J. Biochem. Cell Biol.* **37,** 33–37
10. Orlowski, J., and Grinstein, S. (2004) *Pflugers Arch.* **447,** 549–565
11. Karmazyn, M., Sawyer, M., and Fliegel, L. (2005) *Curr. Drug Targets Cardiovasc Haematol. Disord.* **5,** 323–335
12. Nakamura, T. Y., Iwata, Y., Arai, Y., Komamura, K., and Wakabayashi, S. (2008) *Circ. Res.* **103,** 891–899
13. Cardone, R. A., Casavola, V., and Reshkin, S. J. (2005) *Nat. Rev. Cancer* **5,** 786–795
14. Paris, S., and Pouysségur, J. (1984) *J. Biol. Chem.* **259,** 10989–10994
15. Lacroix, J., Poët, M., Maehrel, C., and Counillon, L. (2004) *EMBO Rep.* **5,** 91–96
16. Pang, T., Su, X., Wakabayashi, S., and Shigekawa, M. (2001) *J. Biol. Chem.* **276,** 17367–17372
17. Matsushita, M., Sano, Y., Yokoyama, S., Takai, T., Inoue, H., Mitsui, K., Todo, K., Ohmori, H., and Kanazawa, H. (2007) *Am. J. Physiol. Cell Physiol.* **293,** C246–C254
18. Ammar, Y. B., Takeda, S., Hisamitsu, T., Mori, H., and Wakabayashi, S. (2006) *EMBO J.* **25,** 2315–2325
19. Mishima, M., Wakabayashi, S., and Kojima, C. (2007) *J. Biol. Chem.* **282,** 2741–2751
20. Aharonovitz, O., Zaun, H. C., Balla, T., York, J. D., Orlowski, J., and Grinstein, S. (2000) *J. Cell Biol.* **150,** 213–224
21. Fuster, D., Moe, O. W., and Hilgemann, D. W. (2004) *Proc. Natl. Acad. Sci. U.S.A.* **101,** 10482–10487
22. Wakabayashi, S., Fafournoux, P., Sardet, C., and Pouysségur, J. (1992) *Proc. Natl. Acad. Sci. U.S.A.* **89,** 2424–2428
23. Wakabayashi, S., Bertrand, B., Shigekawa, M., Fafournoux, P., and Pouysségur, J. (1994) *J. Biol. Chem.* **269,** 5583–5588
24. Wakabayashi, S., Pang, T., Su, X., and Shigekawa, M. (2000) *J. Biol. Chem.* **275,** 7942–7949
25. Stauffer, T. P., Ahn, S., and Meyer, T. (1998) *Curr. Biol.* **8,** 343–346
26. Pouysségur, J., Sardet, C., Franchi, A., L'Allemain, G., and Paris, S. (1984) *Proc. Natl. Acad. Sci. U.S.A.* **81,** 4833–4837
27. Hisamitsu, T., Ben Ammar, Y., Nakamura, T. Y., and Wakabayashi, S. (2006) *Biochemistry* **45,** 13346–13355
28. L'Allemain, G., Paris, S., and Pouysségur, J. (1984) *J. Biol. Chem.* **259,** 5809–5815
29. Wakabayashi, S., Hisamitsu, T., Pang, T., and Shigekawa, M. (2003) *J. Biol. Chem.* **278,** 11828–11835
30. Slater, S. J., Ho, C., Kelly, M. B., Larkin, J. D., Taddeo, F. J., Yeager, M. D., and Stubbs, C. D. (1996) *J. Biol. Chem.* **271,** 4627–4631
31. Rosse, C., Linch, M., Kermorgant, S., Cameron, A. J., Boeckeler, K., and Parker, P. J. (2010) *Nat. Rev. Mol. Cell Biol.* **11,** 103–112
32. Slater, S. J., Taddeo, F. J., Mazurek, A., Stagliano, B. A., Milano, S. K., Kelly, M. B., Ho, C., and Stubbs, C. D. (1998) *J. Biol. Chem.* **273,** 23160–23168
33. Ohmori, S., Sakai, N., Shirai, Y., Yamamoto, H., Miyamoto, E., Shimizu, N., and Saito, N. (2000) *J. Biol. Chem.* **275,** 26449–26457
34. Zhang, G., Kazanietz, M. G., Blumberg, P. M., and Hurley, J. H. (1995) *Cell* **81,** 917–924
35. Kazanietz, M. G. (2002) *Mol. Pharmacol.* **61,** 759–767
36. Taylor, C. W. (2002) *Cell* **111,** 767–769
37. Bertrand, B., Wakabayashi, S., Ikeda, T., Pouysségur, J., and Shigekawa, M. (1994) *J. Biol. Chem.* **269,** 13703–13709
38. Wakabayashi, S., Bertrand, B., Ikeda, T., Pouysségur, J., and Shigekawa, M. (1994) *J. Biol. Chem.* **269,** 13710–13715
39. van Meer, G., Voelker, D. R., and Feigenson, G. W. (2008) *Nat. Rev. Mol. Cell Biol.* **9,** 112–124
40. Mason, D., Mallo, G. V., Terebiznik, M. R., Payrastre, B., Finlay, B. B., Brumell, J. H., Rameh, L., and Grinstein, S. (2007) *J. Gen. Physiol.* **129,** 267–283
41. Snabaitis, A. K., Yokoyama, H., and Avkiran, M. (2000) *Circ. Res.* **86,** 214–220
42. Maly, K., Strese, K., Kampfer, S., Ueberall, F., Baier, G., Ghaffari-Tabrizi, N., Grunicke, H. H., and Leitges, M. (2002) *FEBS Lett.* **521,** 205–210
43. Aharonovitz, O., and Granot, Y. (1996) *J. Biol. Chem.* **271,** 16494–16499
44. Liu, F., and Gesek, F. A. (2001) *Am. J. Physiol. Renal. Physiol.* **280,** F415–F425
45. Counillon, L., Franchi, A., and Pouysségur, J. (1993) *Proc. Natl. Acad. Sci. U.S.A.* **90,** 4508–4512
46. Orlowski, J., and Kandasamy, R. A. (1996) *J. Biol. Chem.* **271,** 19922–19927
47. Ikeda, T., Schmitt, B., Pouysségur, J., Wakabayashi, S., and Shigekawa, M. (1997) *J. Biochem.* **121,** 295–303
48. Sardet, C., Fafournoux, P., and Pouysségur, J. (1991) *J. Biol. Chem.* **266,**

19166–19171
49. Kandasamy, R. A., Yu, F. H., Harris, R., Boucher, A., Hanrahan, J. W., and Orlowski, J. (1995) *J. Biol. Chem.* **270,** 29209–29216
50. Attaphitaya, S., Nehrke, K., and Melvin, J. E. (2001) *Am. J. Physiol. Cell Physiol.* **281,** C1146–C1157
51. Takahashi, E., Abe, J., Gallis, B., Aebersold, R., Spring, D. J., Krebs, E. G., and Berk, B. C. (1999) *J. Biol. Chem.* **274,** 20206–20214
52. Meima, M. E., Webb, B. A., Witkowska, H. E., and Barber, D. L. (2009) *J. Biol. Chem.* **284,** 26666–26675
53. Coccaro, E., Karki, P., Cojocaru, C., and Fliegel, L. (2009) *Am. J. Physiol. Heart Circ. Physiol.* **297,** H846–H858
54. Snabaitis, A. K., Cuello, F., and Avkiran, M. (2008) *Circ. Res.* **103,** 881–890

research articles Journal of proteome research

A Peptidomics Strategy for Discovering Endogenous Bioactive Peptides

Kazuki Sasaki,*,† Noriyuki Takahashi,‡ Mitsuo Satoh,§ Motoo Yamasaki,‡ and Naoto Minamino*,†

Department of Molecular Pharmacology, National Cerebral and Cardiovascular Center Research Institute, Suita, Osaka 565-8565, Japan, Innovative Drug Research Laboratories, Kyowa Hakko Kirin Co., Ltd., Machida, Tokyo 194-8533, Japan, and Antibody Research Laboratories, Kyowa Hakko Kirin Co., Ltd., Machida, Tokyo 194-8533, Japan

Received April 15, 2010

Peptide hormones and neuropeptides constitute an important class of naturally occurring peptides that are generated from precursor proteins by limited proteolytic processing. An important but unaddressed issue in peptidomics is to pin down novel bioactive peptides in a bulk of peptide sequences provided by tandem mass spectrometry. Here, we describe an approach to simultaneously screen for bioactive peptides and their target tissues. The principle behind this approach is to identify intact secretory peptides that have the ability to raise intracellular calcium levels. In practice, we used nanoflow liquid chromatography–tandem mass spectrometry to analyze peptides released by exocytosis from cultured cells. Peptide sequence information was utilized to deduce intact peptide forms, among which those highly conserved between species are selected and tested on an ex vivo calcium assay using tissue pieces from transgenic mice that systemically express the calcium indicator apoaequorin. The calcium assay can be applied to various cell types, including those not amenable to in vitro culture. We used this approach to identify novel bioactive neuropeptides derived from the neurosecretory protein VGF, which evoke a calcium response in the pituitary and hypothalamus.

Keywords: peptidomics • proteolytic processing • apoaequorin • secretory peptides • bioactive peptides

Introduction

Peptide hormones and neuropeptides function as cell-to-cell signaling molecules that mediate many physiological effects. The generation of these bioactive peptides involves a series of cleavage events orderly executed by specific proteases, starting with the endoproteolytic cleavage of precursor proteins to produce peptides with defined lengths.[1,2] These biosynthetic cleavages are often accompanied by post-translational modifications on specific residues, such as N-terminal acetylation and C-terminal amidation.[3] Resultant peptides, termed major processing products or "intact" peptides, are subsequently degraded and inactivated by a variety of proteases.

Peptidomics has been advocated to comprehensively study these naturally cleaved peptides that are beyond the reach of conventional proteomics.[4,5] Tandem mass spectrometry techniques enable the sequence determination of peptides present in complex mixtures for an organism whose genome sequencing nears completion. Efforts have been made to discover neuropeptides by analyzing the total peptide complement of the hypothalamus and pituitary, which are considered treasure troves of bioactive peptides.[6–9] However, despite initial enthusiasm, it has become clear that intact secretory peptides account for a relatively small proportion in a tissue peptidome. Even with known neuropeptides and peptide hormones, most of the identified peptides are N-terminally or C-terminally trimmed from intact peptides, implying that bioactive peptides, present in trace amounts, are difficult to identify in their native molecular forms.[6–9] Hence, delineating intact peptides emerges as a key factor in mass spectrometry-based peptidomic approaches to discovering bioactive peptides.

This "peptide first" approach, however, only leaves behind many peptide sequences and does not offer information about bioactivity or target tissues. One solution to the problem is to focus on post-translational modifications characteristic of known bioactive peptides, for instance C-terminal amidation.[3] Using tandem mass spectrometry, we profiled peptides secreted by cultured endocrine cells and identified novel C-terminally amidated peptides, designated NERP-1 and NERP-2.[10] Since C-terminal amidation does not guarantee that the peptides are bioactive, we were forced to conduct many hit-or-miss experiments to demonstrate that they are bioactive.[10] A more efficient method for identifying bioactive peptides would therefore be desired.

Besides the importance of investigating intact secretory peptides, we have considered the following common features

* To whom correspondence should be addressed. Department of Molecular Pharmacology, National Cerebral and Cardiovascular Center Research Institute, Fujishirodai 5-7-1, Suita, Osaka 565-8565, Japan. Phone: +81 6 6833 5004ex. 2600; Fax: +81 6 6835 5349. E-mail: ksasaki@ri.ncvc.go.jp or minamino@ri.ncvc.go.jp.

† National Cerebral and Cardiovascular Center Research Institute.

‡ Innovative Drug Research Laboratories, Kyowa Hakko Kirin Co., Ltd.

§ Antibody Research Laboratories, Kyowa Hakko Kirin Co., Ltd.

10.1021/pr1003455

Published on Web 08/04/2010

of known bioactive peptides: (1) strong interspecies homology at the amino acid level and (2) frequent use of calcium as a second messenger. In the present study, we describe an approach to screen for bioactive peptides, independent of specific modifications. The core part of this approach is to identify intact peptides released by exocytosis from cultured cells with secretory granules, followed by testing the ability of a candidate to raise intracellular calcium levels. We hypothesized that our transgenic mice systemically expressing apoaequorin, a calcium-sensitive photoprotein,[11] could be used to simultaneously screen for bioactive peptides and their target tissues. In the present study, we examined peptides derived from the neurosecretory protein VGF, the processing of which has not been elucidated, aside from the C-terminal region.[12] We used this peptidomic approach to identify two neuropeptides, hidden in the precursor sequence, that elicited a calcium transient in the pituitary and hypothalamus.

Materials and Methods

Peptide Preparation. Monolayer cultures of TT cells[13] were rinsed three times with Hanks medium (Invitrogen). Culture supernatants of the cells incubated for 15 min after stimulation with 10 μM forskolin plus 10 μM carbachol were harvested and rapidly extracted at 4C using an RP-1 solid-phase extraction cartridge (GL Sciences). Peptide fractions were obtained by HPLC on a gel filtration column (G2000SWXL, 21.5 × 300 mm, TOSOH) at 1.5 mL/min to obtain two fractions named G7−8 and G9−12, which contains peptides around 3000−7000 Da and smaller peptides (around 1000−3000 Da), respectively. Both fractions were reductive alkylated and desalted with Empore C18 cartridges (3M). The resultant samples were individually reconstituted in solvent A (10 mM ammonium formate, pH 3.8: acetonitrile (ACN) = 9:1 (v/v)) and applied to a TSK gel SP-2SW cation-exchange column (1.0 × 50 mm, TOSOH) and eluted at 50 uL/min with a gradient of 0−100% solvent B (1 M ammonium formate, pH 3.8: ACN = 9:1 (v/v)) in 30 min. Fraction G7−8 was divided into five fractions (collected every 5 min, starting 5 min after injection) and fraction G9−12 was into nine fractions (collected every 3 min, starting immediately after injection) using this cation-exchange HPLC. A total of 14 cation-exchange fractions were individually desalted with Empore C18 cartridges and analyzed by LC−MS/MS.

LC−MS/MS. NanoLC−MS/MS experiments were performed with a Chorus nanoflow system (CTC Analytics) connected to an LTQ-Orbitrap mass spectrometer (ThermoFisher Scientific) equipped with a nanoelectrospray emitter (MonoSpray C18 Nano, 100 um × 50 mm, GL Sciences).[14] Sample dissolved in 2% ACN and 0.1% formic acid was loaded via a PAL autosampler (CTC Analytics) onto an L column (Chemicals Evaluation and Research Institute, Japan) and eluted with a linear gradient from 5% ACN, 0.1% formic acid to 60% ACN, 0.1% formic acid over 40 min at 500 nL/min. A protonated ion of polycyclodimethylsiloxane with m/z 445.120025 was used for internal calibration throughout. The mass spectrometer was operated in a data-dependent mode to automatically switch between MS and MS/MS acquisitions. After survey full scan (400−1500 m/z range), five most intense ions (intensity threshold 2×10^5) were isolated for MS/MS in the linear ion trap using collision induced dissociation, with dynamic exclusion onward throughout the following scans. The resultant product ions were recorded in the Orbitrap. For each fraction, any precursor m/z (except for singly charged ions) was subjected to MS/MS and excluded thereafter if detected within a mass width of 5 ppm. Multiple identifications of the same sequence were allowed given that each identification was derived from a different precursor charge state. In addition, redundant identification of the same peptide, which was in most cases caused by distribution over multiple chromatographic fractions, was also allowed in this secretopeptidome analysis (Supplemental Table, Supporting Information).

Data Analysis and Peptide Identification. Peak picking, deisotoping, and deconvolution of MSMS spectra were performed using Mascot Distiller (ver. 2.1.1.0) with the default parameters for OrbiTrap. Peak lists were searched against IPI Human (76539 entries on March 4, 2009) using Mascot (ver. 2.2.04), with no enzyme specification. Mascot was used with monoisotopic mass selected, a precursor mass tolerance of 2 ppm, and a fragment mass tolerance of 25 mmu. Pyroglutamination and C-terminal amidation were simultaneously allowed as variable modifications. The significance threshold was the Mascot default setting of 5%. Each MSMS spectrum was checked manually to confirm or contradict the Mascot assignment. The false discovery rate for the identity threshold was in all cases 0% as estimated by using the Mascot decoy database function. Only peptides identified with a score above the Mascot identity threshold were considered in the present study.

Peptide Synthesis. All peptides were synthesized using Fmoc (*N*-(9-fluorenyl)methoxycarbonyl) strategy, purified by reversed phase HPLC (SigmaGenosys), and verified for correct synthesis by mass spectrometry and amino acid analysis.

Antibody Preparation. Cysteinyl C-terminal peptides of rat NERP-3 (CESPGPERVW) and AQEE-30 (CEHVLLHRP) were synthesized and each coupled with maleimide activated keyhole limpet hemocyanin (Pierce). Rabbits were immunized with each conjugate and antisera were characterized as described.[15]

Mass Spectrometric Characterization of VGF-Derived Peptides. Rat whole brain excluding cerebellum was extracted and condensed with a SepPak C18 cartridge as previously described.[10] Sephadex G-50 gel filtrated fractions of the rat brain extract (2.38 and 1.40 g equivalent for NERP-3 and AQEE-30, respectively) were immunoprecipitated with the antibodies and analyzed on a surface-enhanced laser desorption ionization mass spectrometer (Ciphergen) as described.[16]

Calcium Assay Using Tissues from Apoaequorin Transgenic Mice. Assays were performed as previously described with a few modifications.[11] Tissues or organs from the apoaequorin transgenic mice were cut out as 1−2 mm^3 pieces and incubated with coelenterazine for 3 h. They were sequentially treated with RPMI medium containing 0.01% (w/v) BSA, test peptide (1 μM), a standard and Triton X-100 (final 2.5%). Triton X-100 was used to lyse cells and confirm the expression of functionally active aequorin. The standard refers to one of the following positive controls: angiotensin II (1 μM), bradykinin (1 μM) and ATP (100 μM). A positive control that constantly exhibited higher signals than any other control was used as standard for a given organ, where bradykinin served as standard for pituitary and uterus, ATP for hypothalamus, liver and heart, and angiotensin II for adrenal gland. The mean relative luminescent units (RLU) elicited by the standards from 20 assays (values in parentheses indicate RLU ranges) for the pituitary, hypothalamus, liver, adrenal gland, uterus, and heart were 40,000 (23 000−51 500), 880 (200−3950), 160 (100−300), 2020 (120−9200), 11 600 (1700−32 000), and 820 (120−3000), respectively. Signals induced by test peptides were defined as positive in case RLUs were above 100 for the pituitary or 50 for the others, or above

Figure 1. VGF processing deduced from identified peptides. Sequenced peptides are shown by gray boxes and detailed in Supplemental Table (Supporting Information). Closed arrowheads denote major cleavage sites across the top of the precursor, with basic residues (pale magenta boxes) and the signal sequence (a stippled box) indicated. Orange boxes, C-terminal amidation; red boxes, pyroglutamination.

5% of the RLUs induced by each standard in a given experiment. Peptides were dissolved in RPMI containing 0.01% (w/v) fatty acid-free BSA (Sigma) treated with activated charcoal. Data for test peptides were obtained from three or four independent experiments. A given peptide was considered positive on a tested tissue if positive signals were observed in at least two experiments. All the peptides were used at 1 μM throughout due to limited sensitivity inherent in this assay; endothelin-1, known as a potent vasoconstrictive peptide, did not produce a positive signal below 0.1 μM (data not shown).

Results and Discussion

The human thyroid cell line TT was stimulated with carbachol plus forskolin for 15 min to recover peptides secreted in the medium. The TT secretopeptidome was separated by gel filtration and subsequent cation exchange chromatography into 14 fractions for LC–MS/MS. Among the MS/MS-identified peptides, we studied peptides derived from VGF, a neurosecretory protein.[12,17] *Vgf*, expressed in various neurons and endocrine cells, encodes a 68-kDa protein of 617 amino acids in rodents and of 615 in human that bears several consensus motifs for processing enzymes PC1/3 and PC2 to yield peptides secreted via the regulated secretory pathway.[12] Studies of *Vgf*-deficient mice received much attention since they are lean, hypermetabolic, and resistant to various types of obesity.[18] These findings support the view that VGF is a precursor to multiple bioactive peptides. Major bioactive peptides derived from VGF are AQEE-30,[19] TLQP-62,[19] TLQP-21,[20] NERP-1 and NERP-2.[10] It is hence possible that additional bioactive peptides are embedded in this precursor sequence.

Consequently, we were able to identify 240 redundant peptides (155 distinct sequences) that arise from the human VGF sequence. These peptide sequences were aligned on the precursor sequence to construct a "peptide alignment map" (Figure 1 and Supplemental Figure 1, Supporting Information). Of note, this map is conceptually different from the peptide coverage map commonly used in proteomics studies. The peptide alignment map delineated 15 distinct clusters of the redundant peptides across the entire sequence. Consistent with the reported signal peptide,[12] the N-terminal region of 22 amino acids was not occupied by any peptide sequence (Figure 1). Each cluster consisted of peptides having N- or C-terminal trimming. The peptide ladders observed are not unique to VGF and common among different precursors of the regulatory secretion pathway, such as neuropeptide precursors and chromogranins identified in secretion media of endocrine cells, presumably caused by the action of exopeptidases.[14,21]

In 12 of 15 clusters, the longest peptide in each cluster was flanked by basic residue(s) at both ends (Figure 1 and Supplemental Figure 1, Supporting Information). Except for 232QARI MPD237, the boundaries that separate each cluster fit the consensus motifs for PC1/3 and PC2 ((R/K)Xn(R/K) where n = 0, 2, 4, or 6).[2] While not experimentally verified, the stretch of six basic residues 479KRKRKK484 may be a bona fide target of PC1/3, since PC1/3 actually cleaves the corresponding rat residues 483KRKRKK488.[22] Judging from the number of human peptides identified, APPG-40 (aa 23–62), QQET-30 (aa 177–206), MPDS-45 (aa 235–279), NERP-1 (aa 282–306, C-terminal amidation), NERP-2 (aa 310–347, C-terminal amidation), NAPP-19 (aa 485–503), and AQEE-30 (aa 586–615) were considered intact peptides released from TT cells. As noted earlier, NERP-1, NERP-2,[10] and AQEE-30[19] have been reported as bioactive. Although not illustrated by redundant identification (Supplemental Figure 1, Supporting Information), GGEE-45 (aa 373–417) also appeared to be an intact peptide.

The limited number of human VGF-derived peptides reported in cerebrospinal fluid peptitomics studies[23–25] does not suffice to elucidate an overall processing pattern of the precursor (Supplemental Figure 2, Supporting Information). In the present study, however, we were able to identify most, if not all, of potential processing sites of the precursor (Figures 1 and 2). While some of the clusters are represented by relatively few peptides (Figure 1), this might be caused by poor presentation of acidic peptides in positive ion mode, as exemplified by GGEE-45 with a calculated pI of 3.8. Otherwise, some regions may not have been appreciably converted to peptides in TT cells. For instance, the cleavage site 553RPRITLQ558 (corresponding human sequence 551RPRITLQ556) for the recently reported rat TLQP-21 as well as TLQP-62, an abundant C-terminal peptide in rat brain,[20] did not emerge in the TT secretopeptidome analysis. Since TT cells are of thyroid C-cell origin, the lack of identification might reflect the difference in cell type-specific precursor processing that involves multiple processing enzymes.[26] In two human pancreatic neuroendocrine cell lines we examined, we got evidence that 551RPRITLQ556 represented a major processing site (data not shown). To the

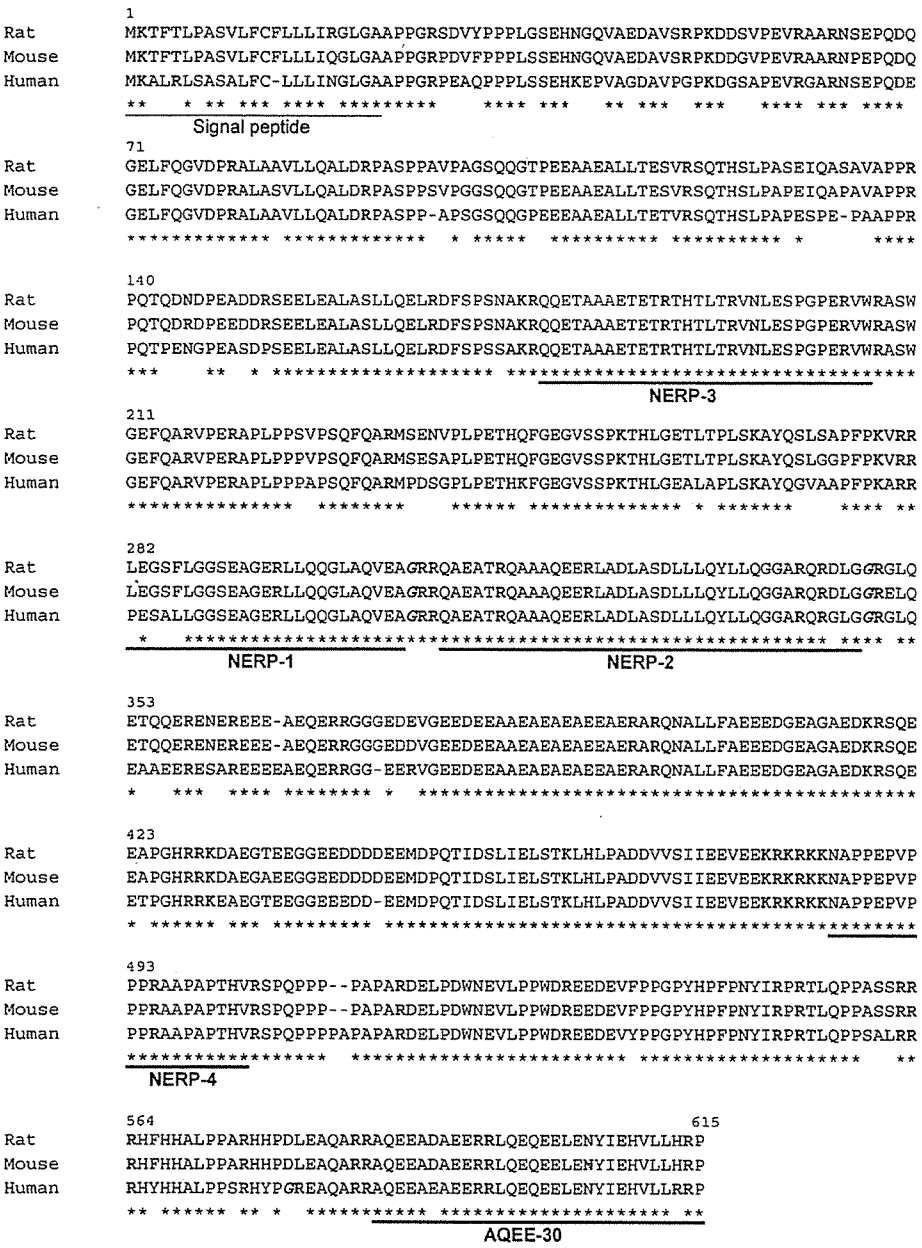

Figure 2. Alignment of rat (IPI00324864), mouse (IPI00378764), and human (IPI00069058) VGF sequences. Asterisks denote identical residues. Basic residues and amidation motifs are marked in bold and bold italic, respectively. The calcium assay was performed with bold underlined peptides. The residue numbering is for the human sequence.

best of our knowledge, this is the first study to demonstrate that accumulated peptide information contributes to elucidation of the overall processing of a precursor protein.

Bioactivity of a peptide cannot be inferred just from its sequence. It would be impossible to synthesize all of the peptides of various lengths revealed by LC–MS/MS. We therefore need to narrow down the number of candidate peptides for assessing bioactivity. In the present study, we took into consideration that peptides with definite biological activity are structurally conserved between species. Given the overall processing pattern (Figure 1), as well as interspecies homology between human and rodent VGF sequences (Figure 2), we selected QQET-30, hereafter designated NERP-3, and NAPP-19, designated NERP-4 (Figure 2). At the amino acid level, they are completely identical between human and rodents. APPG-40 and HYHH-19 (aa 565–583) were excluded since the location of internal basic residues is not conserved between rodent and human sequences (Figure 2). MPDS-45 was disregarded since rodent corresponding peptides were not so identical. HYHH-13 (aa 565–577, C-terminal amidation)[14] was also excluded because rodent VGF sequences do not harbor corresponding amidation sites. The stretch of acidic residues (seven aspartic and/or glutamic acids in human and eight in rodents) led us to disregard human EAEG-48 (aa 431–478. calculated p*I* 3.5). Also, the presence of multiple proline residues in SPQP-49 (aa

Table 1. Calcium Mobilization Induced by Test Peptides in Tissues from Apoaequorin Transgenic Mice[a]

	pituitary	hypothalamus	liver	adrenal gland	uterus	heart
NERP-3	+ (2/3)	+ (2/3)	− (0/3)	− (0/3)	− (0/3)	− (0/3)
NERP-4	+ (3/4)	+ (2/3)	− (0/3)	− (1/4)	− (0/3)	− (0/3)
AQEE-30	+ (2/4)	+ (2/3)	− (0/3)	− (1/4)	− (0/3)	− (0/3)
NERP-1	+ (3/3)	+ (2/3)	− (0/3)	ND	ND	ND
NERP-1-Gly	− (0/3)	− (0/3)	− (0/3)	ND	ND	ND
NERP-2	+ (3/3)	+ (2/3)	− (0/3)	ND	ND	ND
NERP-2-Gly	− (0/3)	− (0/3)	− (0/3)	ND	ND	ND

[a] Peptides were tested at a final concentration of 1 μM throughout. Data were summarized from at least three separate experiments. The peptide was considered active on the indicated tissue if positive signals were observed in at least two experiments. In parentheses, (X/Y) indicates the occurrence of positive signals (X) in total experiments (Y). ND, not determined.

505−553) was a reason for not including this peptide in subsequent assays.

Screening methods for bioactive peptides should be as comprehensive as possible. Given the presence of numerous cell types in an organism, a cell-based assay using a limited number of permanent cell lines or primary cultured cells is not practical. Since calcium is the most common second messenger, we used transgenic mice systemically expressing apoaequorin[11] to develop a tissue-based calcium assay. A candidate peptide is tested for its ability to raise intracellular calcium levels on selected tissues from the mice in a standardized analytical platform. Namely, the evoked calcium transient serves as a marker to report that the peptide is active on a tested tissue. The assay system was validated by bradykinin (pituitary) and ATP (hypothalamus, liver, and heart) and angiotensin II (adrenal gland) in advance. After an induced calcium transient returned to basal levels, expression of functional aequorin in the tested tissues was confirmed by lysing cells with Triton X-100. This treatment liberated intracellular apoaequorin to allow binding to extracellular calcium in incubation medium. At first, the utility of this assay system was assessed with the recently reported bioactive peptides NERP-1 and NERP-2[10] on pieces excised from the pituitary, hypothalamus, and liver. Consistent with their central actions reported in recent studies,[10] they elicited positive responses in the pituitary and hypothalamus (Figure 3 and Table 1). The inability of glycine-extended NERP-1 and NERP-2 to evoke the calcium response was also consistent with the previous report that NERPs' function is dependent on C-terminal amidation.[10] In this assay, the liver was considered a negative control since in most cases it does not respond to known bioactive peptides (data not shown).

NERP-3 and NERP-4, in addition to AQEE-30, were tested on the tissues including pituitary, hypothalamus, liver, adrenal gland, uterus, and heart. Aside from the liver, they are established targets for known neuropeptides and peptide hormones, including previously reported VGF-derived neuropeptides.[10,20] Positive signals were observed in the pituitary and hypothalamus in response to NERP-3 and NERP-4 (Figure 3 and Table 1). The observed calcium transient in the hypothalamus triggered by AQEE-30 may support a previous view that the peptide is a neuropeptide whose activity was first reported in isolated hypothalamic tissue cultures.[19] Overall, we identified two novel VGF-derived peptides that are functional toward the pituitary and hypothalamus.

As for human/mouse/rat NERP-3 and mouse/rat AQEE-30, we were able to prepare antibodies that specifically recognize

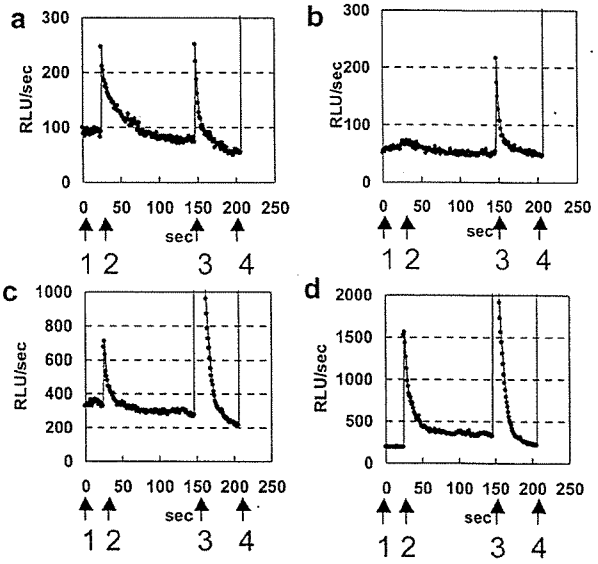

Figure 3. Typical traces of the relative luminescence units (RLU) evoked in hypothalamic tissues from apoaequorin transgenic mice. (a) NERP-1, (b) NERP-1-Gly, (c) NERP-3, and (d) AQEE-30. Peptides were tested at a final concentration of 1 μM. Medium (1), peptide (2), ATP (3), and Triton X-100 (4) were sequentially administered where indicated by arrows.

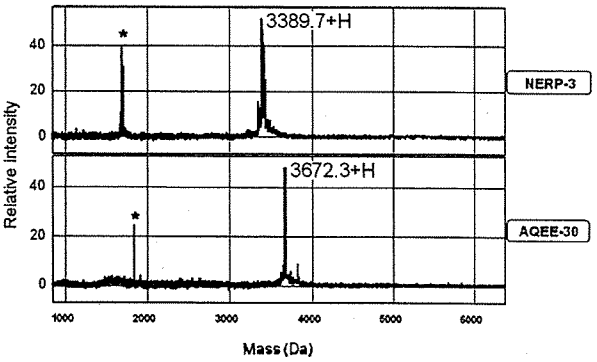

Figure 4. Mass characterization of peptides recognized by NERP-3 and AQEE-30 antibodies. Brain extract was immunoprecipitated with each antibody and analyzed on a surface-enhanced laser desorption ionization mass spectrometer. Asterisks indicate doubly charged ions.

the C-terminus of respective peptide as described in Materials and Methods. Peptides immunoprecipitated from whole rat brain extract were analyzed on a surface-enhanced laser desorption ionization mass spectrometer. Major peaks of the immunoprecipitate coincided with the calculated mass of 3389 Da (NERP-3) and 3672 Da (mouse/rat AQEE-30) (Figure 4), indicating that NERP-3 and AQEE-30 are actual major processing products also in rat brain. Although antibody was not prepared, NERP-4 may be a major peptide also in rodents as deduced by the multiple identifications in the human peptidomic data shown in Figure 1. Overall, this assay resulted in the identification of two VGF-derived peptides, designated NERP-3 and NERP-4, which are active on the pituitary and hypothalamus.

Conclusions

We described an approach to discover bioactive peptides and their target tissues. This approach can be extended to different

cell culture models. Identification of target organs or tissues will help to characterize responding cells and receptors.

Acknowledgment. We thank Emi Mishiro-Sato, Masako Matsubara (National Cerebral and Cardiovascular Center) and Miho Inoue, Machi Kusunoki, Teruyoshi Imada and Toyoko Kashiwagi (Kyowa Hakko Kirin) for expert technical assistance. This work was supported in part by the Program for Promotion of Fundamental Studies in Health Sciences of the National Institute of Biomedical Innovation, and by Grants-in-Aid for Scientific Research from the Japanese Society for the Promotion of Science, Japan. We also thank Junko Kimata, Makoto Takahata and Morihiko Yoshida (Thermo Fisher Scientific, Japan) for LTQ-Orbitrap operation.

Supporting Information Available: Supplemental Table, peptides identified by LC–MS/MS; Supplemental Figure 1, detailed presentation of Figure 1; Supplemental Figure 2, peptides reported in previous cerebrospinal peptidomics studies; Supplemental Figure 3, MS/MS spectra of peptides with modified residues listed in Supplemental Table. This material is available free of charge via the Internet at http://pubs.acs.org.

References

(1) Zhou, A.; Webb, G.; Zhu, X.; Steiner, D. F. Proteolytic processing in the secretory pathway. *J. Biol. Chem.* **1999**, *274*, 20745–8.
(2) Fricker, L. D. Neuropeptide-processing enzymes: applications for drug discovery. *AAPS J.* **2005**, *7*, E449–455.
(3) Eipper, B. A.; Stoffers, D. A.; Mains, R. E. The biosynthesis of neuropeptides: peptide alpha-amidation. *Annu. Rev. Neurosci.* **1992**, *15*, 57–85.
(4) Clynen, E.; Baggerman, G.; Veelaert, D.; Cerstiaens, A.; Van der Horst, D.; Harthoom, L.; Derua, R.; Waelkens, E.; De Loof, A.; Schoofs, L. Peptidomics of the pars intercerebralis-corpus cardiacum complex of the migratory locust, Locusta migratoria. *Eur. J. Biochem.* **2001**, *268*, 1929–39.
(5) Schrader, M.; Schultz-Knappe, P. Peptidomics technologies for human body fluids. *Trends Biotechnol.* **2001**, *10*, S55–60.
(6) Svensson, M.; Sköld, K.; Svenningsson, P.; Andren, P. E. Peptidomics-based discovery of novel neuropeptides. *J. Proteome Res.* **2003**, *2*, 213–9.
(7) Che, F. Y.; Lim, J.; Pan, H.; Biswas, R.; Fricker, L. D. Quantitative neuropeptidomics of microwave-irradiated mouse brain and pituitary. *Mol. Cell. Proteomics* **2005**, *4*, 1391–1405.
(8) Dowell, J. A.; Heyden, W. V.; Li, L. Rat neuropeptidomics by LC-MS/MS and MALDI-FTMS: enhanced dissection and extraction techniques coupled with 2D RP-RP HPLC. *J. Proteome Res.* **2006**, *5*, 3368–75.
(9) Bora, A.; Annangudi, S. P.; Millet, L. J.; Rubakhin, S. S.; Forbes, A. J.; Kelleher, N. L.; Gillette, M. U.; Sweedler, J. V. Neuropeptidomics of the rat supraoptic nucleus. *J. Proteome Res.* **2008**, *7*, 4992–5003.
(10) Yamaguchi, H.; Sasaki, K.; Satomi, Y.; Shimbara, T.; Kageyama, H.; Mondal, M. S.; Toshinai, K.; Date, Y.; Gonzalez, L. J.; Shioda, S.; Takao, T.; Nakazato, M.; Minamino, N. Peptidomic identification and biological characterization of neuroendocrine regulatory peptide-1 and -2. *J. Biol. Chem.* **2007**, *282*, 26354–60.
(11) Yamano, K.; Mori, K.; Nakano, R.; Kusunoki, M.; Inoue, M.; Satoh, M. Identification of the functional expression of adenosine A3 receptor in pancreas using transgenic mice expressing jellyfish apoaequorin. *Transgenic Res.* **2007**, *16*, 429–35.
(12) Levi, A.; Ferri, G. L.; Watson, E.; Possenti, R.; Salton, S. R. Processing, distribution, and function of VGF, a neuronal and endocrine peptide precursor. *Cell Mol. Neurobiol.* **2004**, *24*, 517–33.
(13) Gkonos, P. J.; Born, W.; Jones, B. N.; Petermann, J. B.; Keutmann, H. T.; Bimbaum, R. S.; Fischer, J. A.; Roos, B. A. Biosynthesis of calcitonin gene-related peptide and calcitonin by a human medullary thyroid carcinoma cell line. *J. Biol. Chem.* **1986**, *261*, 14386–91.
(14) Sasaki, K.; Satomi, Y.; Takao, T.; Minamino, N. Snapshot peptidomics of the regulated secretory pathway. *Mol. Cell. Proteomics* **2009**, *8*, 1638–47.
(15) Mishiro-Sato, E.; Sasaki, K.; Matsuo, Y.; Kageyama, H.; Yamaguchi, H.; Date, Y.; Matsubara, M.; Ishizu, T.; Yoshizawa-Kumagaye, K.; Satomi, Y.; Takao, T.; Shioda, S.; Nakazato, M.; Minamino, N. Distribution of neuroendocrine regulatory peptide-1 and−2, and proteolytic processing of their precursor VGF protein in the rat. *J. Neurochem.* **2010**, *114*, 1097–106.
(16) Sasaki, K.; Sato, K.; Akiyama, Y.; Yanagihara, K.; Oka, M.; Yamaguchi, K. Peptidomics-based approach reveals the secretion of the 29-residue COOH-terminal fragment of the putative tumor suppressor protein DMBT1 from pancreatic adenocarcinoma cell lines. *Cancer Res.* **2002**, *62*, 4894–8.
(17) Levi, A.; Eldridge, J. D.; Paterson, B. M. Molecular cloning of a gene sequence regulated by nerve growth factor. *Science* **1985**, *229*, 393–5.
(18) Hahm, S.; Mizuno, T. M.; Wu, T. J.; Wisor, J. P.; Priest, C. A.; Kozak, C. A.; Boozer, C. N.; Peng, B.; McEvoy, R. C.; Good, P.; Kelley, K. A.; Takahashi, J. S.; Pintar, J. E.; Roberts, J. L.; Mobbs, C. V.; Salton, S. R. Targeted deletion of the Vgf gene indicates that the encoded secretory peptide precursor plays a novel role in the regulation of energy balance. *Neuron* **1999**, *23*, 537–48.
(19) Alder, J.; Thakker-Varia, S.; Bangasser, D. A.; Kuroiwa, M.; Plummer, M. R.; Shors, T. J.; Black, I. B. Brain-derived neurotrophic factor-induced gene expression reveals novel actions of VGF in hippocampal synaptic plasticity. *J. Neurosci.* **2003**, *23*, 10800–8.
(20) Bartolomucci, A.; Possenti, R.; Levi, A.; Pavone, F.; Moles, A. The role of the vgf gene and VGF-derived peptides in nutrition and metabolism. *Genes Nutr.* **2007**, *2*, 169–80.
(21) Nikoulina, S. E.; Andon, N. L.; McCowen, K. M.; Hendricks, M. D.; Lowe, C.; Taylor, S. W. A primary colonic crypt model enriched in enteroendocrine cells facilitates a peptidomic survey of regulated hormone secretion. *Mol. Cell. Proteomics* **2010**, *9*, 728–41.
(22) Trani, E.; Giorgi, A.; Canu, N.; Amadoro, G.; Rinaldi, A. M.; Halban, P. A.; Ferri, G. L.; Possenti, R.; Schinina, M. E.; Levi, A. Isolation and characterization of VGF peptides in rat brain. Role of PC1/3 and PC2 in the maturation of VGF precursor. *J. Neurochem.* **2002**, *81*, 565–74.
(23) Selle, H.; Lamerz, J.; Buerger, K.; Dessauer, A.; Hager, K.; Hampel, H.; Karl, J.; Kellmann, M.; Lannfelt, L.; Louhija, J.; Riepe, M.; Rollinger, W.; Tumani, H.; Schrader, M.; Zucht, H.-D. Identification of novel biomarker candidates by differential peptidomics analysis of cerebrospinal fluid in Alzheimer's disease. *Comb. Chem. High Throughput Screen.* **2005**, *8*, 801–6.
(24) Huang, J. T.; Leweke, F. M.; Oxley, D.; Wang, L.; Harris, N.; Koethe, D.; Gerth, C. W.; Nolden, B. M.; Gross, S.; Schreiber, D.; Reed, B.; Bahn, S. Disease biomarkers in cerebrospinal fluid of patients with first-onset psychosis. *PLoS Med.* **2006**, *3*, e428.
(25) Zougman, A.; Pilch, B.; Podtelejnikov, A.; Kiehntopf, M.; Schnabel, C.; Kumar, C.; Mann, M. Integrated analysis of the cerebrospinal fluid peptidome and proteome. *J. Proteome Res.* **2008**, *7*, 386–99.
(26) Rehfeld, J. F.; Bundgaard, J. R.; Hannibal, J.; Zhu, X.; Norrbom, C.; Steiner, D. F.; Friis-Hansen, L. The cell-specific pattern of cholecystokinin peptides in endocrine cells versus neurons is governed by the expression of prohormone convertases 1/3, 2, and 5/6. *Endocrinology* **2008**, *149*, 1600–8.

PR1003455

Chronic kidney disease as an independent risk factor for new-onset atrial fibrillation in hypertensive patients

Takeshi Horio[a], Yoshio Iwashima[a], Kei Kamide[a], Takeshi Tokudome[b], Fumiki Yoshihara[a], Satoko Nakamura[a] and Yuhei Kawano[a]

Objective Chronic kidney disease (CKD) has recently been recognized to be a powerful predictor of cardiovascular morbidity and mortality. Atrial fibrillation (AF), which is a common arrhythmia in hypertensives, is associated with increased risks of cardiovascular events and death. However, the association between CKD and the onset of AF has not been fully elucidated. The present study assessed the hypothesis that CKD may influence the onset of AF in hypertensives.

Methods A total of 1118 hypertensive patients (mean age, 63 years) without previous paroxysmal AF, heart failure, myocardial infarction, or valvular disease were enrolled. CKD was defined as decreased glomerular filtration rate (<60 ml/min per 1.73 m^2) and/or the presence of proteinuria (≥1+).

Results During follow-up periods (mean, 4.5 years), 57 cases of new-onset AF were found (1.1% per year). Kaplan–Meier curves revealed that the cumulative AF event-free rate was decreased in the CKD group (log-rank test $P<0.001$). By univariate Cox regression analysis, age, smoking, left atrial dimension, left ventricular mass index, and the presence of CKD were significantly associated with the occurrence of AF. Among these possible predictors, CKD (hazard ratio 2.18, $P=0.009$) was an independent determinant for the onset of AF in multivariate analysis. Advanced stages of CKD (stages 4 and 5) were strongly related to the increased occurrence of AF.

Conclusion The present study demonstrated that the complication of CKD, especially progressed renal dysfunction, was a powerful predictor of new-onset AF in hypertensive patients, independently of left ventricular hypertrophy and left atrial dilatation. *J Hypertens* 28:1738–1744 © 2010 Wolters Kluwer Health | Lippincott Williams & Wilkins.

Journal of Hypertension 2010, 28:1738–1744

Keywords: atrial fibrillation, hypertension, kidney, proteinuria, renal function

Abbreviations: AF, atrial fibrillation; CKD, chronic kidney disease; eGFR, estimated glomerular filtration rate; IVST, interventricular septal thickness; LA, left atrial; LV, left ventricular; LVDd, left ventricular diameter at end-diastole; LVD, left ventricular diameter at end-systole; PWT, posterior wall thickness; RAS, renin–angiotensin system

[a]Division of Hypertension and Nephrology, Department of Medicine, National Cardiovascular Center, Suita, Japan and [b]Cardiovascular Center Research Institute, Suita, Japan

Correspondence to Dr Takeshi Horio, MD, Division of Hypertension and Nephrology, Department of Medicine, National Cardiovascular Center, 5-7-1, Fujishirodai, Suita, Osaka 565-8565, Japan
Tel: +81 6 6833 5012; fax: +81 6 6872 7486; e-mail: thorio@ri.ncvc.go.jp

Received 16 December 2009 Revised 25 March 2010
Accepted 31 March 2010

Introduction

Atrial fibrillation (AF) is the most common clinically significant arrhythmia in patients with hypertension, even in the absence of antecedent valvular heart disease or coronary artery disease. AF is a significant risk factor for ischemic stroke and heart failure events, and is also associated with increased risks of total and cardiovascular death, especially due to stroke [1]. Therefore, the occurrence of AF in hypertensive patients not only decreases their quality of life but also has a considerable influence on their prognosis and survival. Older age, blood pressure levels, especially ambulatory systolic blood pressure, increased left ventricular (LV) mass, and increased left atrial (LA) size have been known to be risk factors for the onset of AF in hypertensive patients [2–5]. In particular, a previous study showed that age and LV mass were independent determinants of AF incidence in initially untreated patients with essential hypertension [3].

Renal impairment is a powerful predictor of cardiovascular prognosis. Decreased estimated glomerular filtration rate (eGFR) is clearly associated with the increase in future cardiovascular events [6]. Proteinuria, even microalbuminuria, also increases the risk of cardiovascular events and death [7]. Thus, the involvement of renal impairment in the development of cardiovascular disease has recently been noticed. However, no study has shown the association between the onset of AF and renal impairment in hypertensive patients. To assess the hypothesis that chronic kidney disease (CKD) may affect the incidence of AF, the present study investigated the influence of renal impairment and CKD on the new onset of AF in hypertensives.

Methods

Study participants

From 1263 consecutive hypertensive patients who underwent echocardiography at the Division of Hypertension and Nephrology of our hospital between February 1997 and October 2003, 1118 patients (580 men and 538 women; mean age, 63 years) with normal sinus rhythm

0263-6352 © 2010 Wolters Kluwer Health | Lippincott Williams & Wilkins DOI:10.1097/HJH.0b013e32833a7dfe

who had had no history of previous paroxysmal AF and in whom biochemical and urinary data were simultaneously obtained were enrolled in the present study. Patients with various cardiac disorders such congestive heart failure, myocardial infarction, myocardial disease, pericardial disease, valvular heart disease, LV asynergy, or LV systolic dysfunction (fractional shortening <0.25) were excluded from this study. Individuals after permanent pacemaker implantation or patients receiving dialysis were also excluded. Hypertension was defined as a systolic blood pressure of 140 mmHg or more and/or a diastolic blood pressure of 90 mmHg or more by repeated measurements or when medication was taken for treatment of hypertension. Diabetes mellitus was diagnosed according to the American Diabetes Association criteria, such as a fasting plasma glucose of 7.0 mmol/l or more and/or a plasma glucose level at 2 h after a 75-g oral glucose load of 11.1 mmol/l or more, or when medication was taken for treatment of hyperglycemia.

All procedures of the present study were carried out in accordance with institutional and national ethical guidelines for human studies. All participants enrolled in this study were Japanese, and all gave informed consent to participate in this study.

Echocardiography

A comprehensive two-dimensional echocardiography was performed using a cardiac ultrasound unit (Sonos 5500; Philips Medical Systems, Andover, Massachusetts, USA) as previously described [8]. Echocardiographic parameters were measured by the consensus of two experienced investigators who were blinded to the clinical data of the patients. Measurements included interventricular septal thickness (IVST), posterior wall thickness (PWT), LV diameter at end-diastole (LVDd), LV diameter at end-systole (LVDs), and LA diameter. LV fractional shortening was calculated as (LVDd-LVDs)/LVDd. LV mass was estimated using the formula validated by Devereux and Reichek [9]: LV mass $(g) = 1.04 \times \{(IVST + PWT + LVDd)^3 - LVDd^3\} - 13.6$. LV mass was normalized for body surface area and expressed as the LV mass index.

Clinical parameters

At the time of the echocardiographic examination, blood pressure, heart rate, and body mass were determined. Blood pressure was measured by a physician in a hospital outpatient clinic with the patient in a sitting position after over 10 min of rest, using an appropriate-size arm cuff and mercury sphygmomanometer. The first and fifth Korotkoff sounds were used to identify systolic and diastolic values, respectively, and measurements were taken to the nearest 2 mmHg.

Peripheral blood and urine samples were obtained in the morning after an overnight fast. The serum creatinine level was determined by the enzymatic method and eGFR was calculated by the formula of the Modification of Diet in Renal Disease Study with a modified equation for Japanese [10]: eGFR (ml/min per $1.73\,m^2$) = $194 \times age^{-0.287} \times serum\ creatinin^{-1.094} \times 0.739$ (if woman). Urinary protein excretion was assessed by the dipstick test from spot urine samples.

CKD was defined as decreased eGFR less than 60 ml/min per $1.73\,m^2$ and/or the presence of proteinuria ($\geq$1+). The classification of CKD stages was performed according to the guidelines of the National Kidney Foundation classification of CKD [11] as follows; eGFR 90 ml/min per $1.73\,m^2$ or more with proteinuria (stage 1), eGFR 60–89 ml/min per $1.73\,m^2$ with proteinuria (stage 2), and stages 3, 4, and 5 were classified by the levels of eGFR (30–59, 15–29, and <15 ml/min per $1.73\,m^2$, respectively), regardless of the presence of proteinuria.

Follow-up

After the initial assessment, all patients visited our hospital periodically (every 1–2 months) for the treatment of hypertension and concurrent diseases. The pulse and heart beat were checked at every examination. Individuals with irregular pulse or cardiac rhythm and/or patients with complaint of palpitation or chest discomfort received 12-lead electrocardiogram and 24-h Holter recordings. In addition, all patients received standard 12-lead electrocardiogram at least once a year. AF was defined as absence of P waves before each QRS complex, irregular atrial electrical activity with fibrillatory waves varying in size, shape and timing, and completely irregular RR intervals. New-onset AF as the study endpoint was defined as the first presentation of AF during follow-up. Transient postoperative AF, occurring as an isolated episode within one month after surgery, was not counted as an outcome event. Because newly documented AF, not the duration or persistence of the arrhythmia, was the outcome event of interest, no distinction was made between paroxysmal and persistent AF. For patients without any AF event, the date of censor was that of the last contact with the patient.

Statistical analysis

Statistical analysis was performed using StatView Version 5 Software (Abacus Concepts Inc., Berkeley, California, USA). Values were expressed as mean ± SD. An unpaired Student's *t*-test was used for comparison between the two groups. AF event-free curves were derived by means of the Kaplan–Meier method and were compared by log-rank test. Possible predictors of new-onset AF were tested by univariate Cox proportional hazards regression analysis. Then, a multivariate analysis was applied to identify independent predictors and their predictive power. Independent predictors of AF incidence were also evaluated by using a stepwise regression analysis. A value of $P < 0.05$ was accepted as statistically significant.

Table 1 Clinical characteristics of total participants ($n=1118$)

Variable	
Age (years)	63 ± 11
Sex (men) (%)	52
Body mass index (kg/m^2)	24.3 ± 3.4
Duration of hypertension (years)	16 ± 11
Diabetes mellitus (%)	24
Smokers (current or past) (%)	48
Systolic blood pressure (mmHg)	146 ± 16
Diastolic blood pressure (mmHg)	82 ± 11
Heart rate (bpm)	67 ± 8
eGFR (ml/min per 1.73 m^2)	68 ± 32
Urinary protein	
(−) to (±) (%)	74
(1+) to (2+) (%)	16
≥(3+) (%)	10
Antihypertensive treatment	
Ca channel blockers (%)	69
RAS inhibitors (%)	35
β-blockers (%)	29
Diuretics (%)	17
Others (%)	13
Statin use (%)	29

Values are mean ± SD or percentage. eGFR, estimated glomerular filtration rate; RAS, rennin–angiotensin system.

Results

Patient characteristics

The clinical characteristics of all patients are summarized in Table 1. The average duration of hypertension of the patients was 16 ± 11 years, and they had had history of antihypertensive treatment of 11 ± 9 years as average. At baseline, 83% of the study patients were receiving antihypertensive drugs, and 17% were treated with diet and/or exercise therapy only. Ca channel blockers, rennin–angiotensin system (RAS) inhibitors (i.e., angiotensin II receptor blockers and angiotensin-converting enzyme inhibitors), β-blockers, diuretics, and other classes of agents were used alone or in various combinations in 69, 35, 29, 17, and 13% of the study patients, respectively.

The mean duration of follow-up was 4.5 years (range, 0.1–9.1 years), for a total of 5079 patient-years of observation. During follow-up, 57 cases of new-onset AF were found, indicating the incidence was 1.1% per year. Of these 57 AF cases, 39 (68%) were symptomatic and the other 18 (32%) were asymptomatic at the time of the first documented event.

Relations of estimated glomerular filtration rate and proteinuria to the incidence of atrial fibrillation

The effect of eGFR and proteinuria on the incidence of new-onset AF was evaluated. The cumulative AF event-free rate was significantly decreased according to the reduction of basal eGFR (Fig. 1a). Likewise, AF event-free rate was clearly decreased according to the increase in urinary protein levels (Fig. 1b). In the Cox regression analysis, both eGFR (hazard ratio 0.82 per 10 ml/min per 1.73 m^2, $P<0.001$) and proteinuria [(1+) to (2+): hazard ratio 2.31, $P=0.012$; ≥(3+): hazard ratio 5.07, $P<0.001$ vs. (−) to (±)] were significantly related to the incidence of AF.

Effect of chronic kidney disease on the incidence of atrial fibrillation

We divided the present patients into two groups by the absence or presence of CKD, which was defined as decreased eGFR less than 60 ml/min per 1.73 m^2 and/or the presence of proteinuria (≥1+). The participant group with CKD was associated with older age, higher

Fig. 1

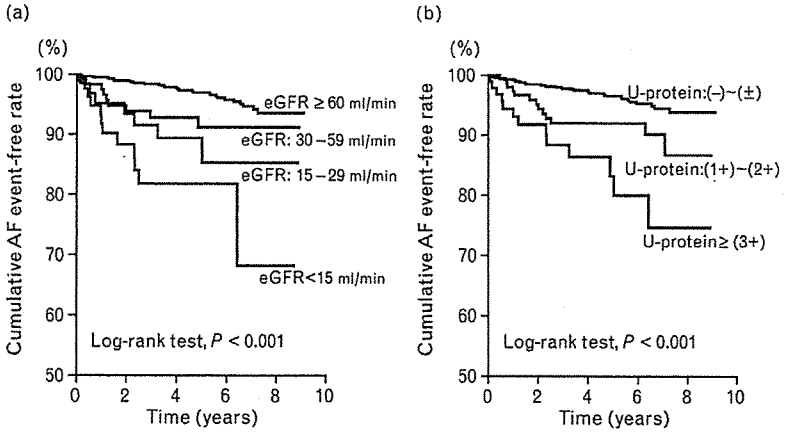

Atrial fibrillation (AF) event-free curves obtained with the Kaplan–Meier method in the respective groups divided by basal estimated glomerular filtration rate (eGFR, a) or urinary protein levels (U-protein, b). (a) All participants were divided into four groups according to basal eGFR levels. Cumulative AF event-free rates in the groups with basal eGFR of ≥60 ($n=818$), 30–59 ($n=128$), 15–29 ($n=73$), and <15 ml/min per 1.73 m^2 ($n=99$) were 93.6, 91.2, 85.3, and 68.2%, respectively (log-rank test, $P<0.001$). (b) All participants were divided into three groups according to basal U-protein levels. Cumulative AF event-free rates in the groups with basal levels of U-protein of (−) to (±) ($n=827$), (1+) to (2+) ($n=183$), and ≥ (3+) ($n=108$) were 93.9, 86.7, and 74.7, respectively (log-rank test, $P<0.001$).

Table 2 Comparison of basal characteristics between the two groups without and with CKD

	CKD (–) ($n=732$)	CKD (+) ($n=386$)
Age (years)	62±11	65±11*
Sex (men) (%)	47	61*
Body mass index (kg/m^2)	24.5±3.4	23.8±3.4*
Duration of hypertension (years)	15±10	18±11*
Diabetes mellitus (%)	18	35*
Smokers (current or past) (%)	44	55*
Systolic blood pressure (mmHg)	144±15	150±17*
Diastolic blood pressure (mmHg)	82±11	81±11*
Heart rate (beats/min)	67±8	67±8
eGFR (ml/min per 1.73 m^2)	83±20	40±30*
Urinary protein		
(–) to (±) (%)	100	25*
(1+) to (2+) (%)	0	47*
≥(3+) (%)	0	28*
Antihypertensive treatment		
Ca channel blockers (%)	61	83*
RAS inhibitors (%)	32	41*
β-Blockers (%)	26	35*
Diuretics (%)	10	30*
Statin use (%)	26	33*
LA diameter (mm)	36±5	37±5*
LV mass index (g/m^2)	121±31	145±44*
LV fractional shortening	0.42±0.07	0.40±0.07*

Values are mean±SD or percentage. CKD, chronic kidney disease; eGFR, estimated glomerular filtration rate; LA, left atrial; LV, left ventricular; RAS, rennin–angiotensin system. *$P<0.05$ compared with CKD (–).

proportion of men, smaller body mass index, and higher rate of diabetes mellitus and smokers (Table 2). In addition, the patients with CKD had longer duration of hypertension, higher systolic blood pressure, and more use of antihypertensive drugs. As for echocardiographic parameters, LA diameter and LV mass index were significantly greater, and LV fractional shortening was slightly lower in patients with CKD than in those without CKD.

When comparing the incidence of new-onset AF between the two groups, the total incidence of AF through the follow-up periods was markedly higher in the patient group with CKD, compared to that without CKD (Fig. 2a). The cumulative AF event-free rate was also significantly decreased in the CKD group, compared to the non-CKD group (Fig. 2b).

As several confounding factors might be involved in the association between CKD and the incidence of AF in the present participants, we examined the independent predictors of new-onset AF by Cox regression analysis. In the univariate analysis, age, smoking, use of diuretic, LA diameter, LV mass index, and the presence of CKD were significantly related to the incidence of AF (Table 3). Among these possible predictive factors, age, smoking, and the presence of CKD were independent predictors of new-onset AF by the multivariate analysis. The adjusted hazard ratio of having CKD for new-onset AF during follow-up was 2.18 (95% confidence interval 1.21–3.90, $P=0.009$). Independent predictors of AF incidence were re-examined by stepwise regression analysis including all clinical and echocardiographic variables as possible independent factors. The presence of CKD as well as age, smoking, and LA diameter was an independent predictor of new-onset AF (age, hazard ratio 1.48 per 10 years, $P=0.008$; smoking, hazard ratio 1.92, $P=0.037$; LA diameter, hazard ratio 1.43 per 5 mm, $P=0.015$; CKD, hazard ratio 2.36, $P=0.004$).

Chronic kidney disease stages and the incidence of atrial fibrillation

The association of CKD stages with the incidence of AF was finally examined. In the univariate Cox analysis, the occurrence of new-onset AF was significantly increased in

Fig. 2

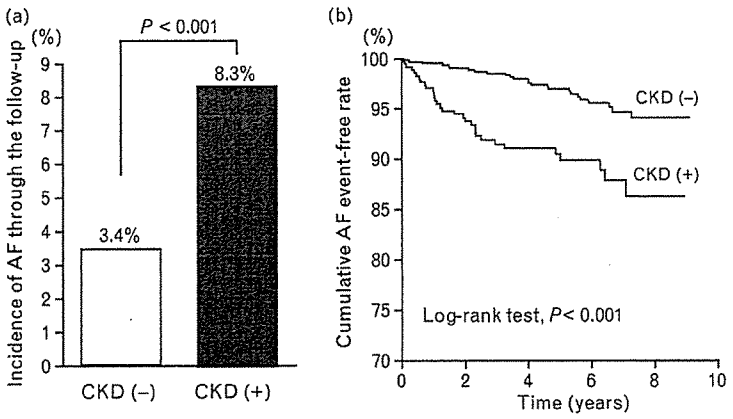

(a) Incidence of atrial fibrillation (AF) through the follow-up periods in the two groups without and with chronic kidney disease (CKD). The total rates of new-onset AF in the patients without and with CKD were 3.4% (0.7% per year) and 8.3% (2.1% per year), respectively ($P<0.001$). (b) AF event-free Kaplan–Meier curves in the two groups without and with CKD. Cumulative AF event-free rates in the non-CKD group and CKD group were 94.1 and 86.3%, respectively (log–rank test, $P<0.001$).

Table 3 **Predictors of new-onset AF by univariate and multivariate Cox regression analysis**

	Hazard ratio (95% CI)	P
Univariate analysis		
Age, 10 years	1.65 (1.24–2.19)	<0.001
Sex, men	1.51 (0.89–2.55)	0.128
Body mass index, 1 kg/m^2	1.01 (0.93–1.09)	0.839
Duration of hypertension, 1 year	1.02 (1.00–1.05)	0.100
Diabetes mellitus, yes	1.34 (0.75–2.40)	0.318
Smoking (current or past), yes	2.23 (1.29–3.84)	0.004
Systolic blood pressure, 10 mmHg	1.06 (0.90–1.25)	0.480
Diastolic blood pressure, 10 mmHg	0.88 (0.69–1.13)	0.316
Heart rate, 1 bpm	0.98 (0.94–1.01)	0.165
Ca channel blocker, yes	1.56 (0.84–2.89)	0.162
RAS inhibitor, yes	0.82 (0.47–1.44)	0.492
β-Blocker, yes	1.38 (0.81–2.35)	0.236
Diuretic, yes	2.23 (1.23–4.03)	0.008
Statin, yes	1.00 (0.57–1.76)	0.990
LA diameter, 5 mm	1.43 (1.10–1.87)	0.008
LV mass index, 10 g/m^2	1.09 (1.03–1.15)	0.004
LV fractional shortening, 0.01	0.98 (0.94–1.02)	0.250
CKD, yes	2.99 (1.77–5.05)	<0.001
Multivariate analysis		
Age, 10 years	1.54 (1.16–2.04)	0.003
Smoking (current or past), yes	1.78 (1.01–3.15)	0.047
Diuretic, yes	1.23 (0.65–2.32)	0.533
LA diameter, 5 mm	1.26 (0.94–1.68)	0.118
LV mass index, 10 g/m^2	1.03 (0.96–1.10)	0.457
CKD, yes	2.18 (1.21–3.90)	0.009

In the multivariate analysis, all variables that had a significant association in the univariate analysis were included as possible independent factors. AF, atrial fibrillation; CI, confidence interval; CKD, chronic kidney disease; LA, left atrial; LV, left ventricular; RAS, rennin–angiotensin system.

the participant groups with CKD stage 3 and more advanced stages (Fig. 3a). After adjustment for confounding factors (i.e., age, smoking, use of diuretic, LA diameter, and LV mass index) by the multivariate analysis, CKD stages 4 and 5 were still significantly associated with the increased incidence of AF (Fig. 3b).

Discussion

The present study has shown that CKD defined as decreased eGFR and/or the presence of proteinuria is longitudinally associated with the incidence of new-onset AF in hypertensive patients. Our results indicate that antecedent existing CKD has a significant influence on new-onset AF in hypertensives.

Several clinical and population-based studies showed that the prevalence of AF was independently associated with decreased eGFR and increased levels of urinary albumin [12–14], although these cross-sectional investigations did not elucidate whether antecedent renal dysfunction affects the incidence of AF. Prospective observational studies examining postoperative AF showed that renal impairment (decreased eGFR or renal failure) was associated with an increased risk of AF after cardiac surgery [15,16]. A recent study reported that decreased baseline eGFR was associated with an increased risk of subsequent new onset AF in a large scale of community-based cohort [17]. The findings of our study are fundamentally consistent with these observations. However, previous

Fig. 3

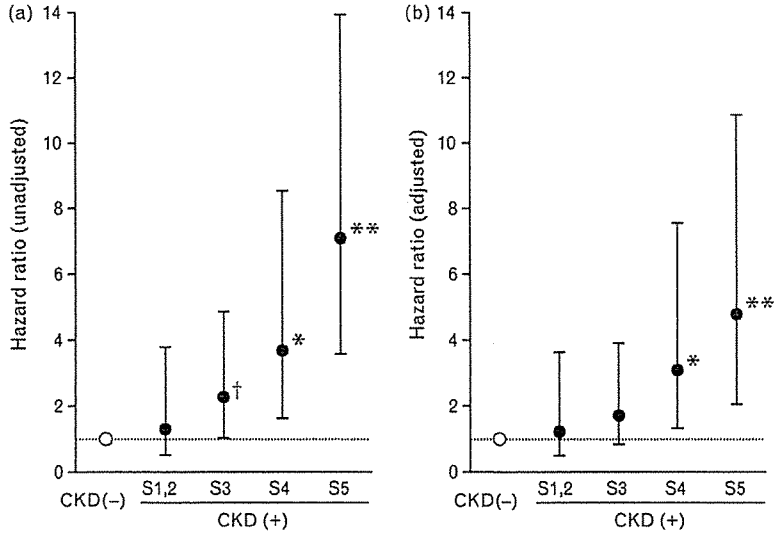

Relation of chronic kidney disease (CKD) stages to the incidence of atrial fibrillation (AF) evaluated by univariate (a) and multivariate (b) Cox regression analysis. Respective data present hazard ratios (open or solid circles) and the 95% confidence intervals (vertical lines) in the groups without CKD ($n=732$) and with CKD stages 1–2 (S1,2, $n=86$), 3 (S3, $n=128$), 4 (S4, $n=73$), and 5 (S5, $n=99$). In the multivariate analysis, all variables that had a significant association in the univariate analysis (i.e., age, smoking, use of diuretic, left atrial diameter, and left ventricular mass index) were included as confounding factors. $^{\dagger}P<0.05$, $^{*}P<0.01$, $^{**}P<0.001$ vs. CKD (–).

studies have shown that many factors are involved in the development of AF in a general population and patients with cardiovascular disorders [18–20]. As for hypertensive patients, it has been revealed that age, systolic blood pressure, LV mass, and LA size are related to the incidence of AF [2–5,21]. Thus, there was the possibility that these factors might mediate the association between CKD and AF incidence observed in the present and other studies, because GFR generally decreases with age, and pressure and volume load augmented by renal dysfunction directly increases LV mass and LA size. In fact, the present patients with CKD had older age, higher systolic blood pressure, and greater LV mass index and LA diameter, compared with those without CKD. In addition, age, LV mass index, and LA diameter as well as CKD were relating factors to the incidence of AF in the univariate Cox regression analysis of this study. By the multivariate analysis, however, the association of CKD with new-onset AF was warranted to be still significant independently of these confounders, although the adjusted hazard ratio of CKD for AF incidence was diminished compared to the crude risk ratio before adjustment. Therefore, the present study has demonstrated for the first time that the existence of CKD in hypertensive patients is an independent predictor of new-onset AF, apart from the effects of aging, LV hypertrophy, and LA dilatation.

Verdecchia *et al.* [3] showed that age and LV mass were the sole independent predictors of new-onset AF in a large cohort of initially untreated patients with essential hypertension. In our patients with chronically treated hypertension, LV mass index was not an independent determinant of the incidence of AF. The exact reason for the discrepant findings is unclear, but there was a possibility that antihypertensive treatment before the enrollment might have modified LV mass in our study.

In the univariate analysis of our study, basal systolic or diastolic blood pressure was not significantly related to the incidence of AF. Previous studies showed that systolic blood pressure and pulse pressure were good predictors of incident AF in large cohorts of the general population [22,23]. In hypertensive patients, however, there have been discrepant findings concerning the significant influence of blood pressure levels on the incident of AF [2–4,21]. Antihypertensive treatment and changes in blood pressure during follow-up might have modified the outcome and have spoiled the possible relation between systolic blood pressure and incident AF in our retrospective observational study. Since the present patients with CKD had a significantly higher systolic blood pressure than those without CKD, there might be a possibility that elevated blood pressure in the CKD group promoted renal dysfunction further, resulting in contribution of new-onset AF partly.

In the present study, the incidence of new-onset AF was clearly associated with the decrease in eGFR. In fact, CKD stages 4 and 5 were a significant predictor of incident AF after adjustment for confounding factors by the multivariate analysis. The incidence of AF was also increased according to the severity of proteinuria. Therefore, our findings suggested that advanced renal dysfunction including massive proteinuria chiefly contributed to the incidence of new-onset AF in the present hypertensive patients.

The causal mechanism by which renal impairment has a great and partly cardiac overload-independent influence on the occurrence of AF in hypertensive patients could not be drawn from our observational study, but there are some possible speculations. The increased risk of developing AF in CKD may be related in part to activation of signaling pathways of inflammation, because previous studies have shown that renal insufficiency is associated with elevations of inflammatory markers such as C-reactive protein [24] and that C-reactive protein predicts increased risk for developing future AF [25]. Possible involvement of oxidative stress and endothelial dysfunction in the development of AF has also been shown [26,27]. Since the patients with chronic renal failure have increased levels of oxidative stress markers and impaired endothelial function [28], oxidative stress and endothelial dysfunction caused by renal impairment may be involved in the increased risk of new-onset AF in patients with CKD. In addition, these mechanisms might be also involved in the association between smoking habit and incident AF observed in the present study, because smoking is known to increase oxidative stress and deteriorate endothelial function.

Limitations

Screening 24-h electrocardiographic recordings were not performed in our study, although standard 12-lead electrocardiograms were periodically done for all the present patients. Therefore, it is possible that asymptomatic cases of AF may have gone undetected. In fact, 68% of 57 cases of newly documented AF were accompanied by some symptom such as palpitation and chest discomfort, and the other 32% were asymptomatic cases in the present study. However, all patients visited our hospital periodically (every 1–2 months) and the pulse and heart beat were checked at every examination. Individuals with irregular pulse or cardiac rhythm received 12-lead electrocardiogram and 24-h Holter recordings, even they had no cardiac symptom. In addition, the incidence of new-onset AF in our study (1.1% per year) was similar to the incidence rates in other studies for patients with essential hypertension (0.5–1.7% per year) [3–5,21] and higher than those in middle-aged and elderly adults from population-based studies (0.2–1.1% per year) [17,18,22,23,29,30]. Thus, it is less likely that there were a considerable number of missed AF cases in the present study. Furthermore, since any misclassification or underdetection of incident AF is

expected to occur at random and independent of renal function, such misclassification would not overestimate the true risk of new-onset AF associated with CKD. The small number of new-onset AF during follow-up, however, must be considered as a limitation of the study, especially in comparing AF incidence rates among more than three groups.

Several studies have revealed that RAS inhibitor treatment and hydroxymethylglutaryl coenzyme A reductase inhibitor (statin) use are associated with reduced incidence of AF in patients with cardiovascular disease [21,31,32]. As another study limitation, therefore, we must consider the possibility that these treatments might bias the outcome of the present study.

Moreover, there was a possibility that the obtained findings in this study might be limited to the Japanese population. Further studies are needed to validate our results in Western and other racial populations.

In conclusion, the present study demonstrated that CKD defined as decreased eGFR and/or the presence of proteinuria was associated with an increased risk of new-onset AF in hypertensive patients, and that the impact of CKD on the incidence of AF was independent of LV hypertrophy and LA dilatation. In particular, advanced stages of CKD were strongly related to the increasing occurrence of AF. In managing hypertensive patients, therefore, it may be important to prevent the progression of renal dysfunction in prevention of the occurrence of new-onset AF.

Acknowledgement

The authors thank Yoko Saito and Miho Nishibata for their secretarial assistance.

There are no conflicts of interest.

References

1 Krahn AD, Manfreda J, Tate RB, Mathewson FA, Cuddy TE. The natural history of atrial fibrillation: incidence, risk factors, and prognosis in the Manitoba Follow-Up Study. *Am J Med* 1995; **98**:476–484.
2 Ciaroni S, Cuenoud L, Bloch A. Clinical study to investigate the predictive parameters for the onset of atrial fibrillation in patients with essential hypertension. *Am Heart J* 2000; **139**:814–819.
3 Verdecchia P, Reboldi G, Gattobigio R, Bentivoglio M, Borgioni C, Angeli F, *et al.* Atrial fibrillation in hypertension: predictors and outcome. *Hypertension* 2003; **41**:218–223.
4 Ciaroni S, Bloch A, Lemaire MC, Fournet D, Bettoni M. Prognostic value of 24-h ambulatory blood pressure measurement for the onset of atrial fibrillation in treated patients with essential hypertension. *Am J Cardiol* 2004; **94**:1566–1569.
5 Okin PM, Wachtell K, Devereux RB, Harris KE, Jern S, Kjeldsen SE, *et al.* Regression of electrocardiographic left ventricular hypertrophy and decreased incidence of new-onset atrial fibrillation in patients with hypertension. *JAMA* 2006; **296**:1242–1248.
6 Go AS, Chertow GM, Fan D, McCulloch CE, Hsu CY. Chronic kidney disease and the risks of death, cardiovascular events, and hospitalization. *N Engl J Med* 2004; **351**:1296–1305.
7 Gerstein HC, Mann JF, Yi Q, Zinman B, Dinneen SF, Hoogwerf B, *et al.* Albuminuria and risk of cardiovascular events, death, and heart failure in diabetic and nondiabetic individuals. *JAMA* 2001; **286**:421–426.
8 Iwashima Y, Horio T, Kamide K, Rakugi H, Ogihara T, Kawano Y. Uric acid, left ventricular mass index, and risk of cardiovascular disease in essential hypertension. *Hypertension* 2006; **47**:195–202.
9 Devereux RB, Reichek N. Echocardiographic determination of left ventricular mass in man: anatomic validation of the method. *Circulation* 1977; **55**:613–618.
10 Matsuo S, Imai E, Horio M, Yasuda Y, Tomita K, Nitta K, *et al.* Revised equations for estimated GFR from serum creatinine in Japan. *Am J Kidney Dis* 2009; **53**:982–992.
11 National Kidney Foundation. K/DOQI clinical practice guidelines for chronic kidney disease: evaluation, classification, and stratification. *Am J Kidney Dis* 2002; **39**:S1–S266.
12 Iguchi Y, Kimura K, Kobayashi K, Aoki J, Terasawa Y, Sakai K, *et al.* Relation of atrial fibrillation to glomerular filtration rate. *Am J Cardiol* 2008; **102**:1056–1059.
13 Böhm M, Thoenes M, Neuberger HR, Gräber S, Reil JC, Bramlage P, Volpe M. Atrial fibrillation and heart rate independently correlate to microalbuminuria in hypertensive patients. *Eur Heart J* 2009; **30**:1364–1371.
14 McManus DD, Corteville DC, Shlipak MG, Whooley MA, Ix JH. Relation of kidney function and albuminuria with atrial fibrillation (from the Heart and Soul Study). *Am J Cardiol* 2009; **104**:1551–1555.
15 Mathew JP, Fontes ML, Tudor IC, Ramsay J, Duke P, Mazer CD, *et al.* A multicenter risk index for atrial fibrillation after cardiac surgery. *JAMA* 2004; **291**:1720–1729.
16 Auer J, Lamm G, Weber T, Berent R, Ng CK, Porodko M, Eber B. Renal function is associated with risk of atrial fibrillation after cardiac surgery. *Can J Cardiol* 2007; **23**:859–863.
17 Watanabe H, Watanabe T, Sasaki S, Nagai K, Roden DM, Aizawa Y. Close bidirectional relationship between chronic kidney disease and atrial fibrillation: the Niigata preventive medicine study. *Am Heart J* 2009; **158**:629–636.
18 Benjamin EJ, Levy D, Vaziri SM, D'Agostino RB, Belanger AJ, Wolf PA. Independent risk factors for atrial fibrillation in a population-based cohort. The Framingham Heart Study. *JAMA* 1994; **271**:840–844.
19 Kannel WB, Wolf PA, Benjamin EJ, Levy D. Prevalence, incidence, prognosis, and predisposing conditions for atrial fibrillation: population-based estimates. *Am J Cardiol* 1998; **82**:2N–9N.
20 Tsang TS, Barnes ME, Gersh BJ, Bailey KR, Seward JB. Risks for atrial fibrillation and congestive heart failure in patients ≥65 years of age with abnormal left ventricular diastolic relaxation. *Am J Cardiol* 2004; **93**:54–58.
21 Wachtell K, Lehto M, Gerdts E, Olsen MH, Hornestam B, Dahlöf B, *et al.* Angiotensin II receptor blockade reduces new-onset atrial fibrillation and subsequent stroke compared to atenolol: the Losartan Intervention For End Point Reduction in Hypertension (LIFE) study. *J Am Coll Cardiol* 2005; **45**:712–719.
22 Conen D, Tedrow UB, Koplan BA, Glynn RJ, Buring JE, Albert CM. Influence of systolic and diastolic blood pressure on the risk of incident atrial fibrillation in women. *Circulation* 2009; **119**:2146–2152.
23 Mitchell GF, Vasan RS, Keyes MJ, Parise H, Wang TJ, Larson MG, *et al.* Pulse pressure and risk of new-onset atrial fibrillation. *JAMA* 2007; **297**:709–715.
24 Shlipak MG, Fried LF, Crump C, Bleyer AJ, Manolio TA, Tracy RP, *et al.* Elevations of inflammatory and procoagulant biomarkers in elderly persons with renal insufficiency. *Circulation* 2003; **107**:87–92.
25 Aviles RJ, Martin DO, Apperson-Hansen C, Houghtaling PL, Rautaharju P, Kronmal RA, *et al.* Inflammation as a risk factor for atrial fibrillation. *Circulation* 2003; **108**:3006–3010.
26 Huang CX, Liu Y, Xia WF, Tang YH, Huang H. Oxidative stress: a possible pathogenesis of atrial fibrillation. *Med Hypotheses* 2009; **72**:466–467.
27 Cengel A, Sahinarslan A, Biberoglu G, Hasanoglu A, Tavil Y, Tulmaç M, Ozdemir M. Asymmetrical dimethylarginine level in atrial fibrillation. *Acta Cardiol* 2008; **63**:33–37.
28 Annuk M, Zilmer M, Lind L, Linde T, Fellström B. Oxidative stress and endothelial function in chronic renal failure. *J Am Soc Nephrol* 2001; **12**:2747–2752.
29 Wang TJ, Parise H, Levy D, D'Agostino RB Sr, Wolf PA, Vasan RS, Benjamin EJ. Obesity and the risk of new-onset atrial fibrillation. *JAMA* 2004; **292**:2471–2477.
30 Watanabe H, Tanabe N, Watanabe T, Darbar D, Roden DM, Sasaki S, Aizawa Y. Metabolic syndrome and risk of development of atrial fibrillation: the Niigata preventive medicine study. *Circulation* 2008; **117**:1255–1260.
31 Healey JS, Baranchuk A, Crystal E, Morillo CA, Garfinkle M, Yusuf S, Connolly SJ. Prevention of atrial fibrillation with angiotensin-converting enzyme inhibitors and angiotensin receptor blockers: a meta-analysis. *J Am Coll Cardiol* 2005; **45**:1832–1839.
32 Pellegrini CN, Vittinghoff E, Lin F, Hulley SB, Marcus GM. Statin use is associated with lower risk of atrial fibrillation in women with coronary disease: the HERS trial. *Heart* 2009; **95**:704–708.

LOX-1 mediates vascular lipid retention under hypertensive state

Atushi Nakano[a], Nobutaka Inoue[a], Yuko Sato[a], Norihisa Nishimichi[b], Kenji Takikawa[b], Yoshiko Fujita[a], Akemi Kakino[a], Kazunori Otsui[a], Saburo Yamaguchi[a], Haruo Matsuda[b] and Tatsuya Sawamura[a]

Objectives Hypertension is a powerful independent risk factor for atherosclerotic cardiovascular diseases; however, the precise molecular mechanisms whereby hypertension promotes atherosclerotic formation remain to be determined. The interaction between oxidized low-density lipoprotein (oxLDL) and its receptor lectin-like oxidized low-density lipoprotein receptor-1 (LOX-1) plays a critical role in atherogenesis. To clarify how hypertension promotes atherosclerosis, we investigated specific roles of LOX-1 in acceleration of lipid deposition under a hypertensive state.

Methods We employed a model of stroke-prone spontaneously hypertensive rats (SHR-SP) that exhibits acute lipid deposition in mesenteric artery induced by high fat and salt loading. These vascular lipid deposition lesions share similar characteristics with the initial lesions of human atherosclerosis.

Results The enhanced LOX-1 expression in SHR-SP was associated with oxidized LDL deposited in vascular wall. Anti-LOX-1 neutralizing antibody dramatically suppressed the lipid deposition *in vivo* in SHR-SP. Vitamin E decreased serum oxLDL-like LOX-1 ligands, and suppressed the vascular lipid deposition. The vascular permeability, evaluated by the leakage of Evans blue, was markedly enhanced by pretreatment of oxLDL. The enhancement of vascular permeability induced by oxLDL was suppressed by anti-LOX-1 antibody.

Conclusion The enhanced expression and activation of LOX-1 mediated the enhancement of vascular permeability, which contributed to the vascular lipid accumulation under hypertensive states. *J Hypertens* 28:1273–1280 © 2010 Wolters Kluwer Health | Lippincott Williams & Wilkins.

Journal of Hypertension 2010, 28:1273–1280

Keywords: LOX-1, oxidized low-density lipoproteins, SHR-SP

Abbreviations: ApoB, Apo-lipoprotein B; DiI, 1,1-dioctadecyl-3,3,3,3-tetramethylindocarbocyanine perchlorate; DiI-oxLDL, DiI-labeled oxLDL; GAPDH, glyceraldehyde 3-phosphate dehydrogenase; HDL, high-density lipoprotein; KRS, Krebs-Ringer solution; LDL, low-density lipoprotein; LOX-1, lectin-like oxidized low-density lipoprotein receptor-1; MBP, mean blood pressure; MFI, mean fluorescence intensity; oxLDL, oxidized low-density lipoprotein; PCR, polymerase chain reaction; SHR, spontaneously hypertensive rats; SHR-SP, stroke-prone spontaneously hypertensive rats; SMC, smooth muscle cells; TC, total cholesterol; Vit-E, Vitamin E; WKY, Wistar–Kyoto rats

[a]Department of Vascular Physiology, National Cardiovascular Center Research Institute, Fujishirodai, Suita, Osaka, Japan and [b]Laboratory of Immunobiology, Department of Molecular and Applied Biosciences, Graduate School of Biosphere Science, Hiroshima University, Hiroshima, Japan

Correspondence to Tatsuya Sawamura, MD, PhD, Director, Department of Vascular Physiology, National Cardiovascular Center Research Institute, 5-7-1, Fujishirodai, Suita, Osaka 565-8565, Japan
Tel: +81 6 6833 5012 x2518; fax: +81 6 6835 5329;
e-mail: t-sawamura@umin.ac.jp

Received 30 July 2009 Revised 28 December 2009
Accepted 1 February 2010

See editorial comment on page 1127

Introduction

An elevation of either systolic or diastolic pressure is a powerful independent risk factor for atherosclerotic cardiovascular diseases [1]. Yamori *et al.* [2] presented important findings, soon after the development of spontaneously hypertensive rats (SHR). Namely, SHR rapidly developed arterial lipid deposition in mesenteric artery and the basilar artery as well as a greater hypercholesterolemic response within two weeks when fed a high-fat diet and 1% salt loading in drinking water [2,3]. This rapid accumulation of lipids, which is referred to as acute atherosis, shares similar characteristics with fatty streak of the initial atherosclerotic lesion. This experimental model, therefore, is useful and appropriate for analyzing pharmacological effects of various substances on the process of atherosclerosis.

Since the proposal of 'the response to endothelial injury/dysfunction hypothesis' [4], the role of endothelial cells in the pathogenic mechanisms of atherosclerosis have been well recognized. On the contrary, 'the response-to-retention model' in early atherosclerosis [5,6] proposed that the retention of lipoprotein in the vessel wall is essential for atherogenesis. Indeed, it is reported that the above-mentioned fatty streak lesion can be found even in young children and infants. The lipid retention, so-called acute atherosis, is also well documented in the maternal vasculature of women with preeclampsia [7,8].

Lectin-like oxidized low-density lipoprotein receptor-1 (LOX-1) was identified as the receptor for oxidized low-density lipoprotein (oxLDL) on endothelial cells [9]. Since this discovery, accumulating evidence has

0263-6352 © 2010 Wolters Kluwer Health | Lippincott Williams & Wilkins

DOI:10.1097/HJH.0b013e32833835d4